Direct Numerical Simulations of Conjugate Heat Transfer under Supercritical Pressure Conditions

Zur Erlangung des akademischen Grades eines
DOKTORS DER INGENIEURWISSENSCHAFTEN (Dr.-Ing.)

von der KIT-Fakultät für Maschinenbau des
Karlsruher Instituts für Technologie (KIT)
angenommene

DISSERTATION

von

M.Sc. Gürel Özeşme

Tag der mündlichen Prüfung:	11.03.2026
Hauptreferent:	Prof. Dr.-Ing. Xu Cheng
Korreferent:	Assoc. Prof. Dr. Ali Tiftikçi

This document is licensed under a Creative Commons
Attribution-Non Commercial 4.0 International License (CC BY-NC 4.0):
https://creativecommons.org/licenses/by-nc/4.0/deed.en

Eidesstattliche Erklärung

Ich versichere wahrheitsgemäß, die Arbeit selbstständig angefertigt, alle benutzten Hilfsmittel vollständig und genau angegeben und alles kenntlich gemacht zu haben, was aus Arbeiten anderer unverändert oder mit Abänderungen entnommen wurde.

Karlsruhe, 3. März 2026

. . . . . .
M.Sc. Gürel Özeşme

Acknowledgements

The journey traveled through this dissertation was made of lots of ups and downs. “Time” was the essence of this work. I dedicate this thesis to the memory of my father, Elvan Özeşme, whose time ended while this dissertation was being written.

The challenges of this journey could not have been overcome without continuous support of my doctoral supervisor, Prof. Dr. -Ing. Xu Cheng. My special thanks go to him for his invaluable expertise, undying patience and tireless efforts that guided me along this path. His contributions to my vision of the world and engineering will be carried forward to further generations.

I would also like to thank my co-supervisor, Assoc. Prof. Dr. Ali Tiftikçi, for his constructive comments and suggestions that guided me in shaping the final form of this work.

I am deeply grateful to my colleagues at the Institute for Applied Thermofluidics (IATF) for their support, friendship and encouragement. Our discussions and everyday laughter made this journey a life experience to be remembered. I would like to give my special thanks to my dear friend and colleague Dr. -Ing. Fabian Alexander Wiltschko who supported me during this work both in the office and outside of it, with great kindness and initiative.

I would like to express my sincere gratitude to my roommates on the Hermann-Ehlers-Kolleg 5th Floor who helped me endure the challenges of adapting to a new country and Covid-19 pandemic as they became my family in Germany.

Distances, time differences, and life challenges altogether can be overcome with true friendship. I would like to give my special thanks to Ceyda Eldem, Ph.D.(c) for her friendship and help with proofreading this dissertation.

Development is a continuous process that requires great efforts and sacrifices. I would like to give my special thanks to my family, and my friends Hasan Tolga Ada and Mert Öztürk who helped me find the strength to continue whenever I faced difficulties.

My sincere thanks go to İrem Karaaslan who made me remember that there is more in life than numbers and simulation results, and who became a partner in both my journey and hers.

This dissertation was supported by the YLSY – Study Abroad Graduate Scholarship Program by the Ministry of National Education, Republic of Türkiye.

Kurzfassung

Das „Generation IV International Forum (GIF)“ hat einen Technologieplan für die Entwicklung von Reaktorkonzepten der vierten Generation vorgeschlagen, der aus fünf zentralen Designaspekten besteht. Eines dieser Konzepte ist der überkritische wassergekühlte Reaktor (SCWR), welcher eine hohe thermische Effizienz sowie ein einfaches Anlagenlayout bietet. Die Verwendung von überkritischem Wasser stellt jedoch Herausforderungen für die Bewertung der Sicherheit und Leistung der vorgeschlagenen Konzepte dar. Der Grund hierfür liegt in den drastischen Änderungen der thermophysikalischen Eigenschaften im pseudokritischen Bereich. Diese Änderungen beeinflussen die Turbulenz und den turbulenten Wärmeübergang in der Wandnähe von Brennelementen. Eine genaue Vorhersage der turbulenten Statistik stellt nach wie vor eine Herausforderung in Bezug auf den aktuellen Stand der Forschung dar.

Diese Arbeit liefert Referenzdaten aus direkten numerischen Simulationen (DNS) unter Berücksichtigung der konjugierten Wärmeübertragung (CHT) für horizontal orientierte, überkritische, turbulente, ringförmige Strömungen, um nukleare Brennstäbe herum. Die Erwärmung der Wand erfolgt über Wärmeleitung im Festkörper, wodurch sich Temperaturfluktuationen innerhalb der Wandstruktur ausbilden, anstatt durch idealisierte Randbedingungen begrenzt zu werden. Die gewonnenen Referenzdaten werden zur Charakterisierung des hochanisotropen, beheizten turbulenten Strömungsfeldes verwendet und mit sekundären Strömungsereignissen verknüpft, um deren Einfluss auf die Turbulenz und Wärmeübertragung zu bewerten. Darüber hinaus wird der Transport der turbulenten kinetischen Energie und des turbulenten Wärmeflusses untersucht, um die dominanten Transportmechanismen im Zusammenhang mit diesen Strömungsereignissen zu identifizieren.

Die DNS-Daten wurden anschließend für eine A-priori-Bewertung von zwei ausgewählten RANS-Schließungen und zwei Turbulenzwärmefluss-Schließungen genutzt, um deren Fähigkeit zur Erfassung anisotroper Turbulenz zu beurteilen. Die getesteten Schließungen wurden hinsichtlich ihrer Fähigkeit bewertet, das beobachtete Verhalten der anisotropen Turbulenz und des turbulenten Wärmetransfers zu reproduzieren. Die A-priori-Bewertung fasst die Schwächen der getesteten Schließungen zusammen. Ein Ansatz mit konstanter turbulenter Prandtl-Zahl war für die Vorhersage des turbulenten Wärmeflusses im vorliegenden Strömungsfeld nicht geeignet, was weitere Untersuchungen zu horizontalen, turbulenten, überkritischen Strömungen erfordert. Zusätzlich war der Temperaturgradient nicht ausreichend, um das Verhalten des turbulenten Wärmeflusses abzubilden, sodass die getesteten Schließungen eine geringe Vorhersageleistung zeigten. Auf Basis dieser Ergebnisse wurden mögliche Richtungen zur Modellverbesserung identifiziert, um die Modellsensitivität hinsichtlich turbulenter Anisotropie und Wärmelast zu erhöhen.

Abstract

The “Generation IV International Forum (GIF)” has proposed a technology roadmap for the development of Generation IV nuclear reactor concepts, which consists of five key design aspects. The supercritical water-cooled reactor (SCWR) is one of these concepts and offers high thermal efficiency and a simple plant layout. However, the use of supercritical water brings challenges for the assessment of the safety and performance of the suggested design concepts due to drastic changes of thermophysical properties in the pseudo-critical region. These changes alter the turbulence and turbulent heat transfer in the near wall region of the fuel assemblies. Accurate prediction of the turbulent statistics still remains a challenge in the current state of the art.

This thesis provides reference direct numerical simulation (DNS) data for horizontally oriented, supercritical, turbulent, annular flow around nuclear fuel pin with conjugate heat transfer (CHT). Heating is provided through conduction inside the solid wall so that temperature fluctuations develop within the wall response, rather than constrained by idealized boundary conditions. Obtained reference data were used for characterizing the highly anisotropic heated turbulent flow field and link these data to secondary flow events to assess their impact on turbulence and heat transfer. Furthermore, the transport of turbulent kinetic energy and turbulent heat flux were investigated to assess dominant transport mechanisms associated with these flow events.

The DNS data were then used to perform a priori assessment of two selected RANS closures and two turbulent heat flux closures to assess their prediction capabilities to capture the anisotropic turbulence. Tested closures were evaluated for their ability to reproduce the observed anisotropic turbulence and turbulent heat transfer behavior. Weaknesses of the tested closures were summarized upon a priori assessment. Constant turbulent Prandtl number approach was not suitable for the prediction of turbulent heat flux within provided flow field that requires further study on horizontal, turbulent, supercritical flows. Additionally, temperature gradient was not sufficient to reflect turbulent heat flux behavior that tested closures presented poor prediction performance. Possible model improvement directions were identified upon the obtained a priori assessment results to improve model awareness in terms of turbulent anisotropy and heat load.

Contents

List of figures

List of tables

Abbreviations

Bishop	Bishop correlation
CHT	Conjugate heat transfer
DB	Dittus–Boelter correlation
DNS	Direct numerical simulation
GEN	Generation
GFR	Gas-cooled fast reactor
GGDH	Generalized gradient diffusion hypothesis
GIF	Generation IV International Forum
HTC	Heat transfer coefficient
KIT	Karlsruhe Institute of Technology
LES	Large eddy simulation
LFR	Lead-cooled fast reactor
MSR	Molten salt reactor
NIST	National Institute of Standards and Technology
RANS	Reynolds-averaged Navier–Stokes
RMS	Root mean square
SCW	Supercritical water
SCWR	Supercritical water-cooled reactor
SFI	Secondary flow intensity
SFR	Sodium-cooled fast reactor
SGDH	Simple gradient diffusion hypothesis
SMR	Small modular reactor
THF	Turbulent heat flux
TKE	Turbulent kinetic energy
VHTR	Very high temperature reactor

Nomenclature

Latin Letters

Symbol	Description	Dimension
A	Area	m^2
a	Turbulent anisotropy tensor	-
B	Buoyancy budget for turbulent kinetic energy transport	m^2/s^3
C	Constant	-
$C_{1C,2C,3C}$	Barycentric weights	-
$c_{p,v}$	Specific heat capacity	$\frac{kJ}{kgK}$
D	Diffusion budget for turbulent kinetic energy transport	m^2/s^3
D_h	Hydraulic diameter	m
D_i	Inner diameter of annular pipe	s
d	Wall distance inside solid domain	m
e	Eigenvalue	-
f	Model function	-
g	Acceleration of gravity	$\frac{m}{s^2}$
G	Mass flux	$\frac{kg}{m^2 s}$
Gr	Grashof number	-
h	Enthalpy	$\frac{m^2}{s^2}$
I	Identity matrix	-
I_a, II_a, III_a	Invariants of anisotropy tensor	-
j	Radial cell grid index	-

k	Turbulent kinetic energy	$\frac{m^2}{s^2}$
K	Thermal activity ratio	-
L	Length	m
$\dot{m}$	Mass flow rate	kg/s
N_2	Total number of cells in radial direction	-
Nu	Nusselt number	-
Pr	Prandtl number	-
P	Production budget for transport equations	m^2/s^3
q''	Heat flux	$\frac{W}{m^2}$
r	Radius	m
Re	Reynolds number	-
R	Reynolds stress	$\frac{m^2}{s^2}$
Ri	Richardson number	-
q	Power	W
S	Strain rate tensor	$\frac{1}{s}$
T	Temperature	K
t	Time	s
t_{clad}	Cladding thickness	m
U	Velocity	$\frac{m}{s}$
x, y, z	Location	-
$x^{1C,2C,3C}$	Barycentric map triangle vertices	-
u, v, w	Velocity in x, y, z directions	$\frac{m}{s}$

Greek Letters

Symbol	Description	Dimension
α	Thermal diffusivity	$\frac{m^2}{s}$
β	Thermal expansion coefficient	$\frac{1}{K}$
γ	Cell stretching parameter	-
Δ	Difference	-
ε	Turbulent kinetic energy dissipation rate	$\frac{m^2}{s^3}$
ε^{THF}	Dissipation budget for turbulent heat flux transport	mK/s^2
η	Kolmogorov length scale	m
δ	Half gap of the annular channel	m
δ_{ij}	Kronecker delta	-
θ	Angle	-
λ	Thermal conductivity	$\frac{W}{mK}$
μ	Dynamic viscosity	$\frac{kg}{ms}$
ν	Kinematic viscosity	$\frac{kg}{ms}$
ρ	Density	$\frac{kg}{m^3}$
σ_k	Model constant	-
τ	Characteristic time	s
τ_{ij}	Shear stress	$\frac{kg}{ms^2}$
ϕ	Flow quantity	-
Ω	Thermal resistance	$\frac{W}{K}$
ω	Rotation rate tensor	$\frac{1}{s}$

Superscripts

Symbol	Description	Dimension
$\overline{\phi}$	Mean value	-
ϕ'	Fluctuating component	-
$\phi^{1C,2C,3C}$	Convex coordinate	-
ϕ^{+}	Quantity normalized in wall units	-

Subscripts

Symbol	Description	Dimension
ϕ_{avg}	Average parameter	-
ϕ_b	Bulk parameter	-
ϕ_{value}	Desired value parameter	-
ϕ_{eff}	Effective parameter	-
ϕ_{pc}	Critical point	-
ϕ_c	Conduction parameter	-
ϕ_{ft}	Flow-through parameter	-
ϕ_f	Fluid domain parameter	-
ϕ_τ	Friction parameter	-
ϕ_{HT}	Heat transfer parameter	-
ϕ_{high}	High parameter	-
ϕ_0	Initial parameter	-
$\phi_{\text{in}/out}$	Inlet/Outlet parameter	-
$\phi_{\text{inner}/outer}$	Inner/Outer wall parameter	-
ϕ_η	Kolmogorov scale	-
ϕ_{low}	Low parameter	-
ϕ_{max}	Maximum parameter	-
ϕ_{mean}	Mean parameter	-
ϕ_{min}	Minimum parameter	-
$\phi_{\mu,\,1,2,3,\theta}$	Model coefficient	-
ϕ_s	Solid domain parameter	-
$\phi_{i,j,k,l}$	Tensor indices	-
ϕ_t	Turbulence parameter	-
ϕ_n	Wall normal direction parameter	-
ϕ_w	Wall property	-

1. Introduction

Global electricity demand continues to grow with technological advances in the world. The need of energy splits into various areas like electrification of transport, mass-production, and high performance computing are needed for newly emerged areas like AI adds further load. Although, efficient use of energy is one of the main concerns, the advances on this field are not competent enough to stop the growing need of installed reliable capacity.

Power demand is met by several energy resources. The oldest of these resources known as fossil fuels, which enabled the mass production of materials. In the early 20th century, electricity generation by nuclear fission was achieved. This success is followed by the first commercial power plants that use atomic energy for power generation to the grid. Unfortunately, the use of atomic energy in power production also generates highly radioactive waste which is still one of the awaiting problems of the nuclear industry. These concerns are covered with high power generation density and lower carbon footprint compared to other energy sources that are used for conventional power generation. Increased environmental awareness and past accidents (and their environmental consequences) encouraged the use of renewable resources. Yet, benefiting from renewable energy resources poses challenges to the electricity grid due to their dependence on weather conditions. Therefore, the use of atomic energy comes forward due to its stable power generation with a high-capacity factor and high availability. Consequently, the design considerations of commercial nuclear power plants are shaped by the operational safety requirements of nuclear power generation.

Generation III (Gen III) reactor designs were seen as reliable to answer industrial needs in this context. They can climb up to gigawatt level power generation rate and exhibit reliable safety standards for commercial operation. Later, these design concepts were enhanced to exhibit additional passive safety features [1]. These improvements are named as Gen III+ designs [2] that retain the Gen III design features with additional passive safety features. Also, small modular reactor (SMR) designs have started to surface in this class, and do not require an enormous financial investment upfront at the construction stage, unlike conventional nuclear reactors. Proposed designs can feature power generation from 50 to 300 MWe per unit. These designs are also subject to further improvements in various aspects like thermal efficiency and reactor safety in comparison to their big-old predecessors. Initial improvements are named as Generation III+ considering existing design with passive safety mechanisms. The expertise gained from these concepts led to advanced nuclear reactor designs that classified as Gen IV nuclear reactors.

The development of Gen IV nuclear reactor designs features various approaches in the concept reactor designs that exhibit advanced versions of previous concepts. The "Generation IV International Forum (GIF)" was established in 2000 [3] to develop a technology roadmap for Generation IV reactor designs. The roadmap proposed includes five key aspects to carry further technological advances in the reactor designs [3],

- Sustainability: Long-term availability and lower nuclear waste production.
- Safety & reliability: The lower the probability of severe accidents, the less need for emergency response.
- Economics: Lower life cycle cost, lower financial risk.
- Proliferation resistance: Increases barriers to the production, diversion, or misuse of weapons-usable nuclear materials.
- Physical protection: Increased security against acts of terrorism.

These aspects are meant to guide the research and development efforts put into the development of the Gen IV reactors. GIF determined six promising Gen IV nuclear reactor designs concepts to include in their technology roadmap:

- Gas-cooled fast reactor (GFR)
- Lead-cooled fast reactor (LFR)
- Molten salt reactor (MSR)
- Sodium-cooled fast reactor (SFR)
- Supercritical water-cooled reactor (SCWR)
- Very high temperature reactor (VHTR)

Among these six concepts, the supercritical water-cooled reactor concept is the reference concept in the scope of this thesis.

1.1 Supercritical water-cooled reactor (SCWR) concept

Supercritical water-cooled reactor (SCWR) appears to be noteworthy among those designs in several reasons. First, it uses supercritical water as coolant which is familiar with existing commercial pressurized water reactor designs over past decade. The operation at high temperature and high pressure (supercritical pressure conditions) makes it possible to reach higher thermal efficiency with a relatively simple reactor cycle layout (Figure 1.1) [4].

The SCWR concept relies on a direct cycle in which the reactor coolant also serves as the working fluid of the turbine. The coolant is pressurized to supercritical pressure conditions (around 25 MPa) and enters the reactor core below the pseudo-critical temperature. As working fluid flows through the reactor core, it is heated through the pseudo-critical region until the reactor core outlet. The heated supercritical water is then sent to the turbine to produce electricity. The excess heat is removed by external heat sink loop and cooled water is pumped back to the reactor pressure and returned to the reactor core.

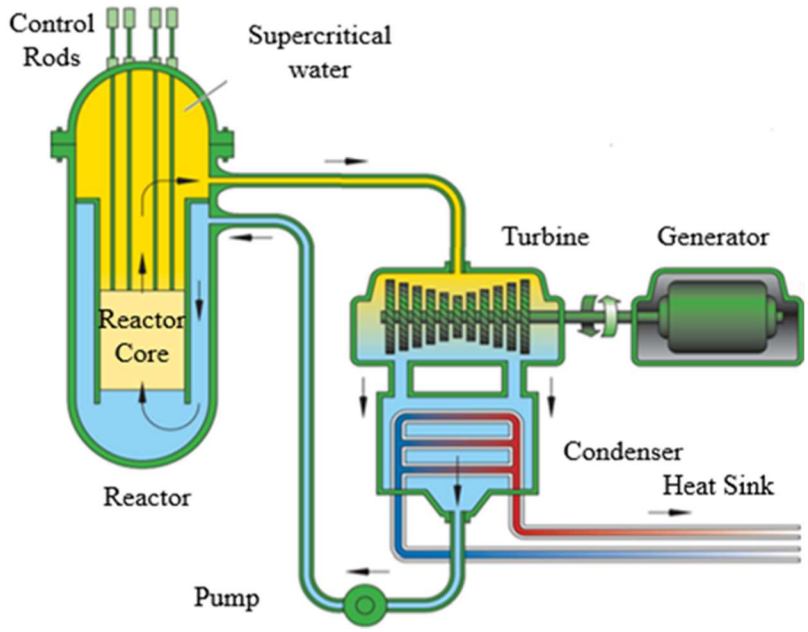

Figure 1.1. Schematic layout of an SCWR power cycle [4].

The design concept is still under development; further improvements are being made within various designs suggestions [5]. These independent design suggestions meet at a reactor core pressure of 25 MPa and a thermal efficiency of ~ 44% with core inlet temperature of 280 °C (553 K) and core outlet temperature of 500 °C (773 K). Fuel enrichment for these designs suggestions varies as well as their high rated power generation around 1-1.6 GWe.

1.2 Importance of turbulence and conjugate heat transfer at SCWR conditions

SCWR concept utilizes higher reactor outlet temperature in their fundamental design. The high temperature output enables the ability to exhibit higher thermal efficiency of the power cycle. Understanding the features of heat transfer under supercritical conditions becomes a key to achieve high efficiency target as heat removal is sustained while keeping temperature levels under the material limits.

The use of supercritical water brings new challenges rather than the conditions provided in the typical pressurized water reactor designs. Under supercritical pressure conditions, water exhibits drastic temperature-dependent variations in its thermophysical properties near the so-called pseudo-critical region. These changes can substantially alter local heat transfer quality [6] leading sudden enhancement or deterioration. The changes in the heat transfer are also connected to the occurrence of secondary flow that mainly acts separately from the main flow. Secondary flow appears due to heating that leads to various physical phenomena like buoyancy induced flow, laminarization, thermal acceleration of the fluid and stratification. The change in the thermophysical properties in pseudo-critical region amplifies these flow events. Turbulence tends

to be highly anisotropic and intermittently unstable under the direct effect of these conditions which aids heat removal process throughout reactor core. The coupling between heat transfer and turbulence forms complex and chaotic feedback that continuously affects the flow and the feedback itself.

The study on turbulence and heat transfer in supercritical flows still requires further research even though various studies have been held so far covering experimental and numerical studies of different levels. In the current state of research, the results of immediate changes of thermophysical properties in terms of heat transfer and turbulence cannot yet be fully assessed. The accurate determination of heat transfer coefficient cannot be achieved especially at the pseudo-critical region. The discrepancy in the prediction leads to further issues since the prediction of the temperature field both in the fuel surface and heated flow are deviated. It is crucial to understand abovementioned physical mechanisms under the SCWR conditions to perform accurate assessments regarding proposed SCWR designs and improve them for further development stages.

These targets can be addressed by comprehensive analysis of experimental and numerical studies. Experimental studies are used to measure general behavior of the flow and provide reference data for numerical studies. Numerical studies provide additional insight at different levels of detail, depending on the modelling approach used. The general behavior of the flow can be predicted by Reynolds-Averaged Navier-Stokes (RANS) simulations in which turbulence and heat transfer are entirely modeled. However, under the complex flow conditions, the general flow behavior presented in a low accuracy due to modeling and the use of relatively low grid resolution in exchange for the small computational cost. In addition, turbulence and heat transfer models may require further calibration needs for specific flow conditions to achieve desired prediction capabilities. Large Eddy Simulations (LES) can partially do modeling turbulence and heat transfer. LES resolves large turbulent scales and models sub-grid scales of turbulence. The resolution of larger scales of turbulence provides higher accuracy rather than RANS but computationally far more expensive in return. To fully resolve turbulence without modeling, grid should be arranged to resolve all scales of turbulence in given boundary conditions of the flow. In this way, Navier-Stokes equations can be resolved by means of Direct Numerical Simulation (DNS).

DNS is mainly used to provide experiment-like quality or reference numerical data for the detailed assessment of turbulence and heat transfer under given boundary conditions dedicated for the aim of the research. These boundary conditions are important not only to define boundaries of the flow domain, but also important for how these boundaries influence the flow field. The heat is applied to the domain by ideal iso-flux or iso-thermal boundary conditions which can lead to inaccurate prediction of turbulent heat transfer and may result in either over-predicted or under-predicted turbulent heat transfer. The use of the conjugate heat transfer enhances the prediction accuracy by resolving heat diffusion within the solid wall instead of relying on idealized thermal boundary conditions. Heating through the solid wall treats thermal statistics as solid domain (or heated wall) modeled [7]. A realistic high-accuracy representation of the turbulent flow together with heat conduction in the solid wall can provide an insight that can be benefited for further developments of turbulence and turbulent heat flux closures which fail under the strong thermophysical property gradients and heating induced secondary flows which can lead to locally varying anisotropic turbulence. These improvements are necessary for an accurate assessment of the turbulence and heat transfer under supercritical pressure conditions.

1.3 Thesis goals and outline

Although various studies have been performed for high-fidelity simulations with supercritical fluid, there is a gap in the literature for horizontal annular pipe flow under supercritical conditions with conjugate heat transfer. This thesis addresses this gap by providing DNS reference data for horizontal annular flow around a fuel pin under SCWR conditions with conjugate heat transfer. The geometry is the representative geometry of fuel channel that presented in ECC-SMART project [8], which aimed to develop a small modular reactor (SMR) cooled by supercritical water (SCW-SMR) by joint efforts of European, Canadian, and Chinese partners.

The reference data include the following,

- Fundamental flow statistics.
- Two-point correlations: Reynolds stresses and its anisotropy, turbulent heat flux.
- Three-point correlations: Transport budgets of turbulent kinetic energy and turbulent heat flux.

Obtained data are used to establish the connection between physical phenomena such as the effect of buoyancy, thermal acceleration, and laminarization. The use of conjugate heat transfer and its effect on turbulent heat transfer is addressed in this manner. The thesis is structured as six chapters,

1. **Introduction:** The motivation and goals of the thesis.

2. **The state of the art:** Fundamental knowledge regarding turbulence and heat transfer, literature survey regarding both experimental and numerical studies in the context of DNS works done in supercritical pressure conditions.

3. **Methodology:** Detailed information about DNS setup: description of the cases, material selection, boundary conditions, grid structure, numerical schemes, governing equations, and validation of the numerical method.

4. **Turbulence and heat transfer at supercritical pressure conditions:** Representation of obtained statistics and evaluations on fundamental data, turbulent stresses and heat transfer, budget profiles, and discussion to link between statistics and flow phenomena.

5. **A priori assessment of RANS turbulence and heat flux closures: Analysis with DNS data:** The test of RANS closures by their capability to capture the changes in flow field with anisotropic turbulence by a priori assessment method by provided DNS data.

6. **Conclusion and future work:** A priori analysis of selected RANS models in terms of capability to capture anisotropic behavior of the flow and response of dedicated models to buoyant movement of the fluid.

2 State of the art

SCWR conditions mentioned are simplified at supercritical water at the pressure of 25 MPa and temperatures from 280 °C (core inlet) to 500 °C (core outlet) for the scope of this thesis.

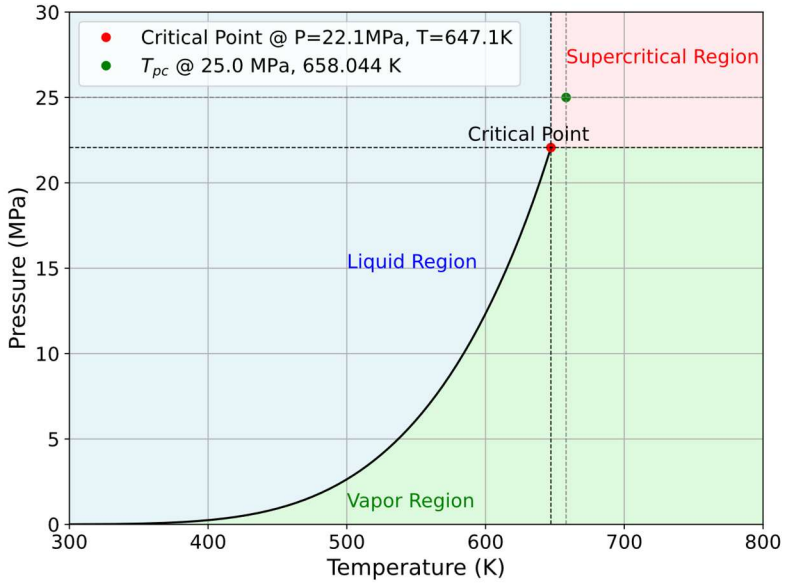

Figure 2.1 Phase diagram of water [9].

These conditions lie beyond critical point as indicated in Fig 2.1. The red region denoted in the figure covers the area where fluid is supercritical. Fluid state is described here as "gas-like" due to thermophysical property changes it goes through. The pseudo-critical temperature T_{pc} at 25 MPa is indicated by green dot. Focus is given to the pseudo-critical region which covers the vicinity of the T_{pc}. As seen in Fig 2.2, the rate of change of thermophysical properties reaches the maximum at the pseudo-critical region located around pseudo-critical temperature (T_{pc}) of 658 K under the 25 MPa pressure according to the data obtained from REFPROP database [9].

The changes observed in the pseudo-critical region [10] that affecting both turbulence and heat transfer due to drastic changes in thermophysical properties of the fluid. Figure 2.2 illustrates the magnitude of these property variations for density (ρ), viscosity (μ), thermal conductivity (λ), enthalpy (h), and specific heat (c_p). In a very narrow temperature range, fluid exhibits significantly lower viscosity that reduces viscous stresses and density drops less than 30% of its value. The heat conductivity exhibits an instant fall while its ability to hold heat (isobaric heat

capacity) peaks at the T_{pc}. Later, isobaric heat capacity returns to its early value by completing its peak.

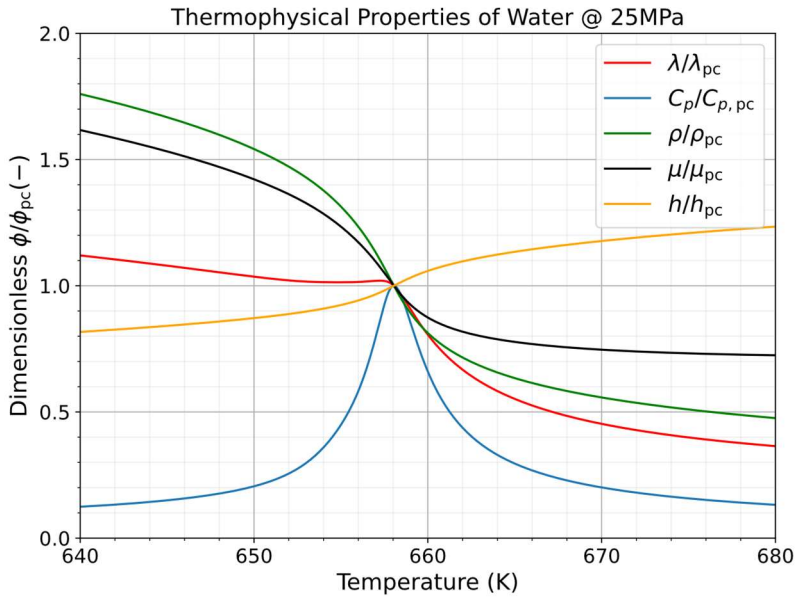

Figure 2.2. Thermophysical properties of supercritical water at 25 MPa [8], [9].

These changes contribute to physical events in the flow field in terms of turbulence and heat transfer. As turbulence production and transport are directly challenged with the changes of density and viscosity. Heat transfer is also directly affected by the changes in thermal conductivity and specific heat. Therefore, these changes affect heated turbulent flow regime. The secondary flow events alter the state of turbulent structures by making them spatially inhomogeneous and directional (anisotropic).

2.1 Turbulence and anisotropy

The term “turbulence” refers to fluid flow in which fluid particles do not follow a smooth and steady path as in laminar flow. Instead, the speed and direction of the particle subject to continuous chaotic fluctuations. In other words, they exhibit irregular, unsteady, and chaotic behavior. These are features of the turbulent flow regime, that widely benefited in many industrial applications such as energy, heating, automotive industry. The presence of turbulent motions aids heat removal processes in complex systems enabling engineers to design components with better performance. In case of internal flows, the criteria for whether the flow is turbulent or not is characterized by Reynolds number that is calculated as the ratio of inertial forces over frictional (viscous) forces [11],

$$Re = \frac{G D_h}{\mu} \tag{2.1}$$

G is the mass flux of the flow in the concerned channel with hydraulic diameter d_h. For fully developed internal flows in the smooth circular tubes [12], flow is laminar when Re < 2100. The flow is considered turbulent when Re > 4000. The range 2100 ≤ Re ≤ 4000 is considered transitional regime. The movement of fluid particles is illustrated in Figure 2.3.

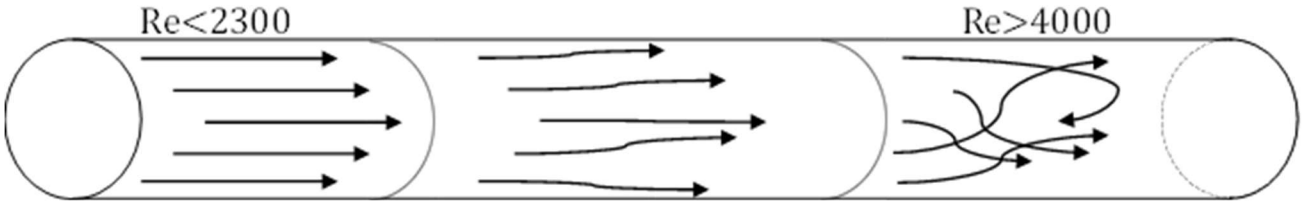

Figure 2.3. Illustration of movement of fluid particles in different flow regimes.

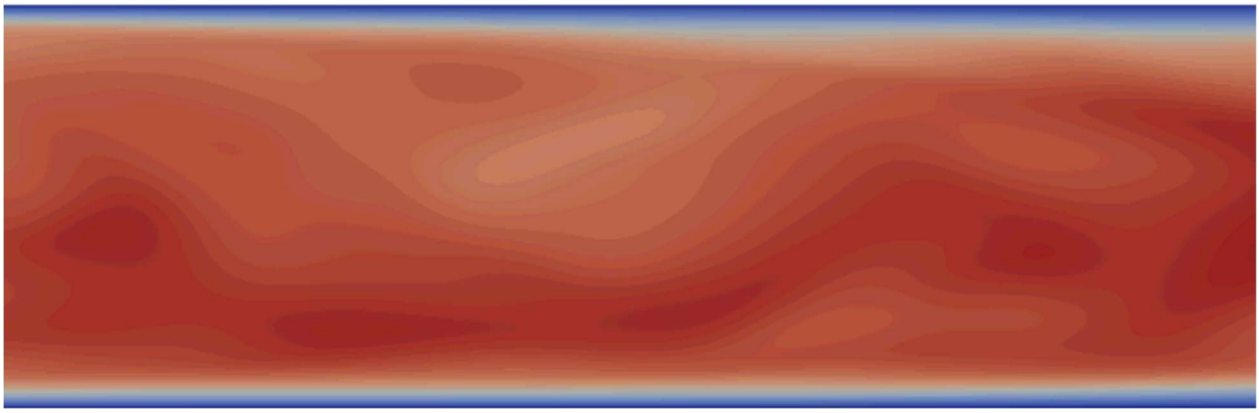

Figure 2.4. Instantaneous streamwise velocity field from DNS of annular pipe flow.

High and low speed streaks are part of the velocity fluctuations in turbulent channel flow. An example of an instantaneous streamwise velocity field is shown in Fig. 2.4. As instantaneous velocity of the turbulent flow is subject to continuous change, similar behavior can be seen in other flow properties. Therefore, the instantaneous value of any quantity $\phi(t)$ can be decomposed into its mean and fluctuating components.

$$\overline{\phi} = \lim_{T\to\infty} \frac{1}{T} \int_{t_0}^{t_0+T} \phi(t)dt, \quad \phi = \overline{\phi} + \phi' \tag{2.2}$$

Overline symbol defines the mean value of ϕ averaged over time. Meantime, ϕ' refers to fluctuating component on that time. In the case of velocity, three spatial components should be considered and can be written in vector formation similar to Eq 2.2,

$$U(t) = \begin{bmatrix} \overline{u} \\ \overline{v} \\ \overline{w} \end{bmatrix} - \begin{bmatrix} u' \\ v' \\ w' \end{bmatrix} \tag{2.3}$$

Therefore, the mean and fluctuating velocity components can be written in tensor form,

$$U = \begin{bmatrix} u \\ v \\ w \end{bmatrix} = \begin{bmatrix} u_i \\ u_j \\ u_k \end{bmatrix} \tag{2.4}$$

Mean velocity and its fluctuations can be evaluated to perform statistical analysis on the characterization of turbulence. Turbulent stresses, or Reynolds stresses can be calculated by obtaining time average (Reynolds average) of the product of velocity fluctuations. The tensor notation of velocity components can be shown as below. Obtained averages can be used to describe the local transport of momentum of fluid particles inside the fluid flow[13]. Reynolds stresses are defined into a 3x3 tensor matrix by considering three axes of movement.

$$\overline{u_i' u_j'} = \frac{1}{N} \sum_{t=0}^{t=N} u_i'(t) u_j'(t) \tag{2.5}$$

$$R_{ij} = \overline{u_i' u_j'} = \begin{bmatrix} \overline{u_i' u_i'} & \overline{u_i' u_j'} & \overline{u_i' u_k'} \\ \overline{u_j' u_i'} & \overline{u_j' u_j'} & \overline{u_j' u_k'} \\ \overline{u_k' u_i'} & \overline{u_k' u_j'} & \overline{u_k' u_k'} \end{bmatrix} \tag{2.6}$$

The indices (i, j, k) in the Eq. 2.6 correspond to the velocity components (u, v, w). In this study, the main flow direction is represented by w and is aligned with the z direction. The 3x3 tensor mentioned above is symmetric, so it has only six independent components. Reynolds stresses are a key quantity for assessing how turbulence is affected under provided flow conditions. The turbulent kinetic energy provides a simple measure of how strong the turbulence is in a specific location. The turbulent kinetic energy per unit mass is calculated by half the sum of the normal Reynolds stresses,

$$k = \frac{1}{2} \overline{u_i' u_i'} = \frac{1}{2} \left(\overline{u'u'} + \overline{v'v'} + \overline{w'w'} \right) \tag{2.7}$$

The magnitude of each Reynolds stress tensor components differs, which means the fluctuating momentum transport is not the same in the three coordinate directions. In the case of ideally isotropic turbulence, it is expected that momentum transport by fluctuating components is evenly distributed to all three directions. However, shape of the turbulent structures in the flow field changes every moment. The mathematical meaning of ideally isotropic turbulence assumption is that all principal Reynolds stresses are equal, and all off-diagonal terms of Reynolds stress tensor are zero.

$$R_{ij} = \frac{2}{3} k \delta_{ij}, \ (i = j) \tag{2.8}$$

$$R_{ij} = 0, \ (i \neq j) \tag{2.9}$$

As a result of the isotropic turbulence assumption, the Reynolds stress tensor has only non-zero elements in the diagonal part. The formulation for the turbulent kinetic energy can be used to describe the isotropic part of the turbulence,

$$\overline{u'u'} = \overline{v'v'} = \overline{w'w'} = \frac{2}{3}k \tag{2.10}$$

On the other hand, anisotropy of turbulence can be spotted by the difference in the directional magnitude of the stress elements. Still, the nature of turbulence makes it difficult to distinguish the state of these structures because of its continuous rotational movement. The anisotropic state of the turbulence can be assessed by calculating anisotropy tensor [14],

$$a_{ij} = \frac{\overline{u_i' u_j'}}{2k} - \frac{1}{3}\delta_{ij} \qquad where\ \delta_{ij} = \begin{cases} 1 & if\ i = j \\ 0 & if\ i \neq j \end{cases} \tag{2.11}$$

$$I_a = a_{ii} \tag{2.12}$$

$$II_a = a_{ij}a_{ji} \tag{2.13}$$

$$III_a = a_{ij}a_{jk}a_{ki} \tag{2.14}$$

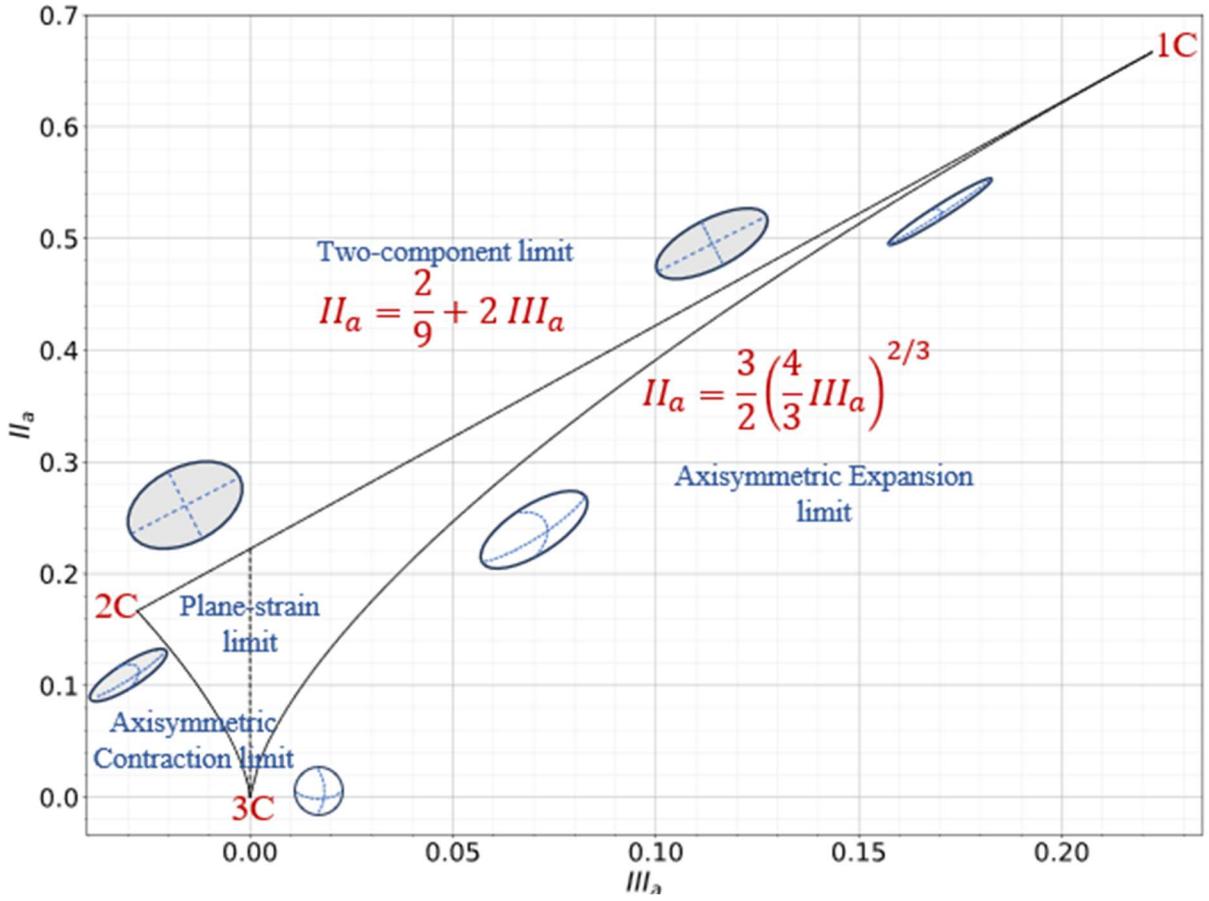

Figure 2.5. Anisotropy invariant map for turbulence (adapted from [15].).

The anisotropy tensor a_{ij} provides a dimensionless measure of the deviation from the isotropic turbulence at a given location of the flow. In ideally isotropic turbulence, anisotropy tensor becomes zero which means that there are no discrepancies in between normal Reynolds stresses and all shear stresses vanish. In other conditions, the value of the anisotropy tensor quantifies the degree of anisotropy of the turbulent structure. As the turbulent structures rotate, their shape remains the same even though their orientation changes. As the turbulent structures rotate, their

shape remains the same even though their orientation changes. The shape of turbulent structures can be inferred by calculating the second and third invariants of the anisotropy tensor [14]. These invariants are plotted together on an anisotropy invariant map (AIM) to provide further insight into the turbulent structures, as shown in Fig. 2.5.

The boundary curves define the mathematical limits of physically realizable turbulent anisotropy can be reached [16]. There are three limiting states of turbulence that each have mathematical boundaries. The axisymmetric expansion symbolizes the state of the turbulence that stretches or attenuates in one principal direction while others are being dampened. Turbulent structure exhibits the "prolate ellipsoid" or "rod-like" shape along the limit. On the other hand, the axisymmetric contraction refers to turbulent structure widens/compresses in two directions while the third one is being suppressed. The limiting equation [17] for both states given below,

$$II_a = \frac{3}{2}\left(\frac{4}{3}|III_a|\right)^{2/3} \tag{2.15}$$

The upper end of the Lumley triangle is drawn by "2-component limit" indicating there is no momentum transport to the third direction in the turbulent structure. The shape of turbulence is totally planar, and energy is shared in between two other directional movements. 2 component limiting state require ideal conditions to happen like no-slip wall condition. The limiting equation follows linear path,

$$II_a = \frac{2}{9} + 2III_a \tag{2.16}$$

The AIM represents three different states of turbulence by the labels 3C, 2C and 1C that denote three, two and one component turbulence. 3C point refers to isotropic turbulence that the turbulent kinetic energy is equally distributed among normal Reynolds stress components which form a spherical shape. Anisotropy increases with the departure from the 3C state that transforms to a planar shape through 2C point (state). 1C point refers to rod-like one component turbulence which indicates the turbulence essentially confined to (or dominant to) a single direction. These transitions are visually described in Fig. 2.5 and are used to describe the anisotropic behavior of turbulence in terms of limiting states and transition region in between them. The representation provided by AIM can be put in a linear and uniform description of turbulent anisotropy in convex coordinates by reorganizing them for Barycentric map [17]. The mathematical procedure to retrieve the convex coordinates depends on the eigenvalues (e_1, e_2, e_3) of the anisotropy tensor.

$$a = [a_{ij}] = \frac{R_{ij}}{2k} - \frac{1}{3}I \tag{2.17}$$

$$det(a - eI) = 0 \tag{2.18}$$

The eigenvalues of the anisotropy tensor matrix $(e_1 \geq e_2 \geq e_3)$ provide basis for anisotropic weight coefficients to be used for barycentric coordinates of turbulent anisotropy. The following relations can be used to calculate these coefficients,

$$C_{1C} = e_1 - e_2 \tag{2.19}$$
$$C_{2C} = 2(e_2 - e_3) \tag{2.20}$$
$$C_{3C} = 1 + 3e_3 \tag{2.21}$$

These weights symbolize the linear (C_{1C}), planar (C_{2C}), and spherical (C_{3C}) states of the turbulent anisotropy. The sum of these weights equals to unity in each possible state. The limiting states provided in AIM appear in the new coordinates for the barycentric map as vertex point locations of equilateral triangle.

$$[x^{1C}, x^{2C}, x^{3C}] = \left[(1,0), (0,0), \left(\frac{1}{2}, \frac{\sqrt{3}}{2}\right)\right] \tag{2.22}$$

The convex coordinates in the barycentric map can be calculated by the equation including properties of all three limiting states.

$$x = C_{1C}x^{1C} + C_{2C}x^{2C} + C_{3C}x^{3C} \tag{2.23}$$
$$C_{1C} + C_{2C} + C_{3C} = 1 \tag{2.24}$$

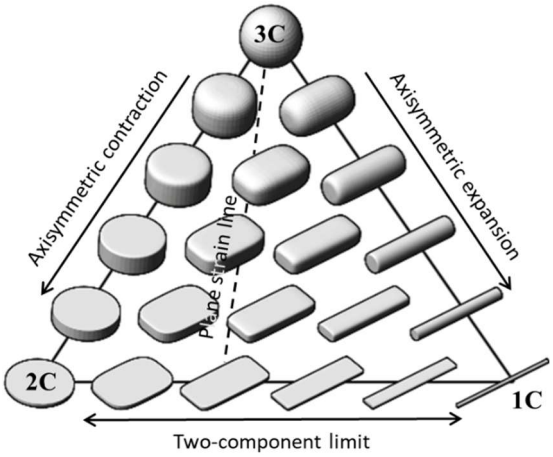

Figure 2.6. The adapted figure of limiting states and respective states of the turbulent structures [17], [18].

The limiting states on the AIM (Fig. 2.5) / barycentric maps (Fig. 2.6) describe how turbulence becomes rod-like (1C), planar (2C), or isotropic (3C) under acting forces in the flow like wall-generated shear and buoyancy related effects. Shear stress is defined as the wall normal interaction of streamwise momentum of the flow. It has two main elements separating viscous effects and inertial effects [11].

$$\tau = \rho\nu\frac{d\overline{U}}{dy} - \rho\overline{u'v'} \tag{2.25}$$

y term indicates wall-normal direction and ν is wall normal velocity component. The flow velocity value falls to zero at the wall (no-slip condition) with the help of the viscous effects. The effect of the viscosity is distinctively visible in the velocity profile at the vicinity of the wall, called the

viscous boundary layer (or sublayer) by Prandtl [19]. The equation for the wall shear stress can be found below as the no-slip condition applies,

$$\tau_w = \rho\nu\left(\frac{d\overline{U}}{dy}\right)_{y=0} \tag{2.26}$$

The contribution of viscous part fades along with the viscous boundary layer as velocity gradient approaches to the zero. Inertial elements contribution becomes important for the regions further to wall than viscous sublayer. The wall shear stress can be used to scale turbulent quantities in terms of velocity and wall distance. The friction (shear) velocity can be calculated as follows,

$$u_\tau = \sqrt{\tau_w/\rho} \tag{2.27}$$

The near wall region or turbulence itself can be characterized by the friction Reynolds number by using half channel height (δ) and the ratio of friction velocity and kinematic viscosity at the wall.

$$Re_\tau = u_\tau\delta/\nu \tag{2.28}$$

These quantities can be used to quantify thickness of the viscous sublayer or the near wall turbulence. In turbulent flow research, they benefit for dimensionless analysis such as dimensionless wall distance y^+ and dimensionless velocity u^+.

$$y^+ = u_\tau y/\nu \tag{2.29}$$

$$u^+ = \overline{u}/u_\tau \tag{2.30}$$

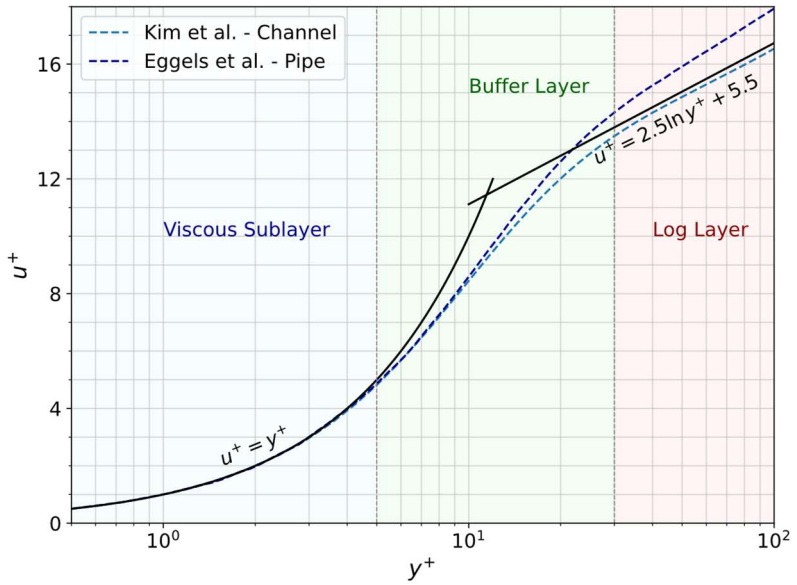

Figure 2.7. Profile of streamwise velocity in the dimensionless form [20], [21].

As the effect of the viscosity diminishes by the distance from the wall, the transition from the viscous sublayer to turbulent core region starts. The linear relationship (Eq. 2.31) deviates slightly

as the distance from the wall increases [11]. The log law (Eq. 2.32) becomes effective for the turbulent core region (logarithmic layer) as dominance shifts from viscous effects to shear in the buffer layer. This transition region so-called "buffer layer". The fully developed turbulent flow is formed by the presence of three regions altogether. The relation of the wall distance and the streamwise velocity profile of fully developed turbulent flow field across regions are given in Fig. 2.7 within equations 2.31 – 2.32.

$$u^+ = y^+, \ where \quad y^+ < 5 \tag{2.31}$$

$$u^+ = 2.5lny^+ + 5.5, \ where \quad y^+ > 30 \tag{2.32}$$

2.2 Heat transfer

Heat transfer is used to describe the transport of thermal energy due to temperature differences. Heat transfer can happen in modes such as conduction, convection, and radiation. In this thesis, heat applied to the flow domain modeled by imposed wall heat flux. A heat source q (W) applied to surface area A (m^2) is defined as heat flux (W/m^2).

$$q'' = q/A \tag{2.33}$$

2.2.1 Conduction

The conduction heat transfer is associated with diffusive transport by temperature gradients in the modeled domain. Heat flux due to conduction in wall normal direction is given by Fourier's law [22],

$$q_n'' = -\lambda \frac{dT}{dx_n}\bigg|_w \tag{2.34}$$

Eq 2.34 defines wall normal heat flux where λ is the thermal conductivity of the fluid and dT / dx_n is temperature gradient in the wall normal direction. Heat is transferred by conduction which is driven by temperature gradients at the near wall region of the flow. This region is called conductive sublayer [19]. However, the turbulent transport of heat should be taken into account in turbulent flows.

$$\overline{q}_n'' = \overline{q}_\lambda'' + \overline{q}_t'' \tag{2.35}$$

$$\overline{q}_n'' = -\lambda \frac{d\overline{T}}{dx_n} - \rho c_p \overline{u_n' T'} \tag{2.36}$$

In Eq. 2.36, wall normal heat flux $\overline{q}_n''$ is decomposed into heat flux by conduction $\overline{q}_\lambda''$ and turbulent flux $\overline{q}_t''$. Here, T' symbolizes temporal fluctuations of temperature which used to form second order quantity as velocity-temperature correlation $u_n' T'$ in Eq. 2.37. The velocity-temperature

correlation used to analyze the turbulent transfer behavior as it refers to turbulent heat flux similarly to the Reynolds stresses for the fluctuating momentum transfer.

$$THF = \overline{u_i' T'} = \overline{(u_i - \overline{u_i})(T - \overline{T})} \tag{2.37}$$

2.2.2 Convection

The convective heat transfer is driven by the fluid's bulk motion in addition to diffusive thermal energy transport. The wall heat flux due to convection is commonly expressed by Newton's law of cooling,

$$q_w'' = HTC\ (T_w - T_b) \tag{2.38}$$

Equations 2.38 uses temperature difference in between wall and bulk flow multiplied by convective heat transfer coefficient $HTC\ \left(W/(m^2K)\right)$. The Nusselt number is a dimensionless number that can be used to assess the quality of convective heat transfer,

$$Nu = \frac{HTC D_h}{\lambda} \tag{2.39}$$

By definition, the Nusselt number is a dimensionless ratio of convective to conductive heat transfer. It requires the convective heat transfer coefficient HTC to be determined for complete assessment. The heat transfer coefficient depends on the flow conditions, geometry, and fluid. So, it cannot be obtained by thermophysical property data of the fluid alone. Instead, it requires to use of empirical correlations proposed used for this purpose; the Dittus – Boelter (DB) correlation can be given as an example [6],

$$Nu_{DB} = 0.023 Re^{0.8} Pr^{0.4} \tag{2.40}$$

DB correlation is widely used in literature. It should be noted that it was originally developed for single phase, heated turbulent flows in smooth, circular tubes within the range of $\mathrm{Re} \gtrsim 10^4$ and $0.7 \lesssim Pr \lesssim 160$. In case of supercritical flows, DB correlation can reasonably predict the heat transfer coefficient [23] at the supercritical pressure conditions. However, it fails in the pseudo-critical region where significant thermophysical property changes are present [24]. Several correlations developed over years that show relatively better prediction accuracy in supercritical flows. For horizontal supercritical flows, the Bishop correlation has shown better agreement especially in the pseudo – critical region for the prediction of the heat transfer coefficient [6], [25], [26],

$$Nu_{Bishop} = 0.0069 Re^{0.9} \overline{Pr}^{0.66} \left(\frac{\rho_w}{\rho_b}\right)^{0.43} \left(1 + 2.4 \frac{D_h}{z}\right) \tag{2.41}$$

$$where \qquad \overline{Pr} = \frac{\overline{c_p}\mu}{\lambda},\ \ \overline{c_p} = \frac{h_w - h_b}{T_w - T_b} \tag{2.42}$$

z refers to streamwise location that is required to calculate entry effects that flow is subjected. Mean Prandtl number $\overline{Pr}$ has been used in Bishop correlation instead conventional form of the Prandtl number. Also, the ratio of wall and bulk fluid densities are taken into account. These features make the Bishop correlation is more convenient to use in horizontal supercritical flows in circular tubes. On the other hand, correlation itself requires prior knowledge about temperature development in the flow field, as bulk temperature and wall temperature information are required. The use of DB and Bishop correlations in the scope of this thesis are introduced in Chapter 3.

Changes in the heat transfer quality and whether the flow is in "normal, deteriorated, or enhanced" regime can be assessed by the changes in the wall temperature in the relevant location in the flow field. "Normal" heat transfer exhibits behavior similar to convective heat transfer under subcritical pressure conditions unlike supercritical region. The heat transfer coefficient is relatively well predicted by correlations like DB that perform well in such conditions for general engineering use. Under supercritical pressure conditions, strong property variations in the pseudo-critical region can strongly affect the heat transfer regime. In this region, the thermal conductivity first rises slightly, then subjects to rapid fall while the specific heat capacity draws a sharp peak at the pseudo-critical temperature. These changes lead to higher wall temperatures rather than the normal heat transfer regime for a given heat flux, which is characterized by lower heat transfer coefficient for deteriorated heat transfer [27]. This effect appears at the heated flow when wall temperature exceeds pseudo-critical temperature while the bulk temperature of the flow remains below it $\left(T_b < T_{pc} < T_{wall}\right)$. The deterioration event is more evident as applied heat flux increases, which is also connected to the buoyancy effect due to fluid density changes. Even though several criterions offered the onset of deteriorated heat transfer, the exact conclusion has not been made yet. In the case of low heat flux applied, enhanced heat transfer might occur at the pseudo-critical region as higher HTC can be observed in comparison to normal regime of heat transfer. This is caused by the sharp increase in the specific heat capacity [6]. Another possible reason for the enhanced heat transfer regime to happen in horizontal pipe flows due to buoyancy effects as heated fluid accumulates at the top region whereas it causes locally deteriorated heat transfer regime while the bottom part of the wall remains cooler, which results in enhancement in the heat transfer as well [28], [29].

The temperature difference between wall surface and the fluid forms the thermal boundary layer. The convective heat transfer is enabled by the bulk fluid motion as heat being carried away by the fluid motions. There are two modes of convective heat transfer: natural convection and forced convection. Natural convection occurs by temperature dependent density changes in the fluid. As the fluid heats up, it gets lighter, they try to move against the gravitational direction. This phenomenon also benefited in the passive safety systems introduced in the Gen 3+ nuclear reactor designs [30]. On the other hand, forced convection occurs when the flow is mainly driven by the external forces where buoyancy is negligible in comparison. However, there are cases that both secondary flow by the buoyancy and flow driving external effects (e.g., pump), remain active simultaneously. Resulting effects of both convection mechanisms couple and form mixed convection regime. The degree of the influence of buoyancy effects on the flow can be quantified by the Grashof number Gr which is used to characterize the relative importance of buoyancy and viscous forces in the flow.

$$Gr = \frac{g\beta(T_{wall} - T_b)D_h^3}{\nu_b^2} \tag{2.43}$$

In Eq 2.43, $g\ (m/s^2)$ refers to gravitational acceleration, $\beta(1/K)$ thermal expansion coefficient, and $\nu_b(m^2/s)$ kinematic viscosity. Another setting for such judgement is to understand how fluid particles are transported by buoyant effects in comparison to inertial forces (Re). In the current state of the art, the quantification on the regime of convective heat transfer can be made by the Richarson number ($Ri = Gr/Re^n$) which is the ratio of Grashof number and power of Reynolds number. Yet, there is no consensus in the literature for the threshold that buoyancy is effective over the flows in supercritical pressure conditions [31]. In case of horizontal flow in supercritical pressure conditions, following relation has been selected to evaluate the dominance of by calculating the Richardson number [32],

$$Ri = Gr/Re^2 \tag{2.44}$$

There are different findings regarding use of the Richardson number as a criterion for buoyancy effects. In the case of horizontal flows with water in supercritical pressure conditions, experimental studies report that the buoyancy effects become noticeable is set to 0.1 [31]. For cases where $Ri < 0.1$, the flow is considered to be in forced convection regime. Richardson number remains important until it reaches 10, where flow is under the mixed convection regime under the influence of both forced and natural convection. In cases where $Ri > 10$, the flow driven predominantly by buoyancy where it can be considered as natural convection. At this point, the influence of forced convection is either negligibly small or absent. In this thesis, the onset criterion for the buoyancy effect is selected as following,

$$0.1 < Ri < 10 \tag{2.45}$$

In cases where the buoyancy effect is very low, it is reported that the low end of the buoyancy criteria fails to assess whether the buoyancy effect takes place accurately. Although extensive experimental and numerical studies have been conducted in the current state of the art, no consensus has yet been achieved in the literature [28–30].

2.3 Experimental studies

One of the earliest available experimental works in this context was conducted by Yamagata [33]. Their study includes experiments at different pressures and heat fluxes for vertical and horizontal water flows under supercritical pressure conditions. The prediction performance of correlations was compared with obtained results, and the effects of changing flow boundary conditions were discussed extensively. An extensive literature survey about experimental works for supercritical water and carbon dioxide (sCO_2) was made in 2005 by Pioro and Duffrey [27], [34]. The mentioned works are classified according to flow orientations, geometries and working fluid. Based on these studies, further comments on deteriorated heat transfer in horizontal and vertical

channels are provided. The effectiveness of heat transfer correlations over collected works is extensively investigated. Four experimental works that use supercritical water with an annulus geometry are mentioned; all were performed in the vertical orientation. It has been noted that the heat transfer regime depends on the heat load applied to the annulus. Overall, it has been concluded that three modes of heat transfer (normal, deteriorated, and enhanced) can take place regardless of the orientation of the tube section. Enhancement by the buoyancy effect has been pointed out for the works made with horizontal tubes, which are directly visible by wall temperature values in the different angular locations on the wall. Driven by the non-uniform wall temperature, heat transfer occurs more efficiently at the bottom wall rather than on the top wall. In some cases, it is possible to observe that heat transfer at the top wall is deteriorated while heat transfer at the bottom wall is enhanced. The degree and extent of the deterioration affect the recovery from deterioration to enhancement process. It is observed that the recovery of heat transfer was weaker at the top wall for the cases where deteriorated heat transfer was observed in both top and bottom walls [25].

Few studies exist for supercritical R134a (sR134a); most of the studies conducted for supercritical water and sCO_2 have been repeated for sR134a as well. The use of different fluids allows further understanding whether observed heat transfer regimes take place due to the flow conditions regardless of fluid itself. Therefore, these additional experimental data led to further modifications on existing heat transfer correlations. One of these modifications was proposed [35] upon these findings to the Gnielinski's correlation due to its characteristic behavior that overcorrects flow variations. The new correlation was reported to perform better predictions within provided experimental matrix for sR134a. Later, Tian et al. revisited buoyancy criterion [29] for horizontal flow of sR134a. Experimental measurements reported for different tube diameters, heat flux, and mass flux values were used to evaluate the threshold for the buoyancy effect. As they compared different buoyancy criteria, they proposed a simple correlation for engineering use to overcome inconsistencies in threshold values defined for the Richardson number and Jackson buoyancy criterion [36]. The new simplified criterion for the buoyancy effect is constructed by heat flux, tube diameter, and mass flux parameters and evaluated for the experiments with supercritical water provided in the literature [37], [38].

Similar work was performed for sCO_2 [39] in relatively large diameter tubes. Their conclusion indicates that increased mass flow rate and increased tube diameter both increased the heat transfer coefficient (HTC). These findings are used to modify the Dittus – Boelter correlation for improved prediction under supercritical pressure conditions. The existence of buoyancy effects in the horizontal flows allows the occurrence of secondary flows, which leads to the flow stratification [25], [26]. It is observed that the presence of stratified layer forms a flow region that exhibits different behavior of flow and heat transfer. The distinction caused by the stratified layer reflected to the flow as different heat transfer quality in between the top and bottom sides of the tube. This phenomenon brings challenges to the predictions made by heat transfer correlations. It has been found that the Bishop correlation shows better accuracy in the pseudo-critical region among the other correlations evaluated. One of the main features of this work is that flow acceleration is separately evaluated from the buoyancy effect, in which the flow acceleration increases towards the pseudo-critical region and loses momentum afterwards. The flow acceleration by thermal expansion effect was relatively minor compared to the buoyancy effect in the horizontal flows [40]. Later, similar evaluations were made with experimental results from vertical flows [41].

The extent of the available experimental works under supercritical pressure conditions and connected studies dealing with the detailed investigation of heat transfer provides an overview about the understanding obtained regarding the flow conditions examined. The findings are provided have been tested more extensively with vertical flows due to their availability in the literature. However, it is not the case for horizontal flows in supercritical pressure conditions. No consensus has been reached on the onset of criterion for buoyancy effect. Furthermore, accurate prediction of heat transfer in pseudo-critical region still needs further research. The findings obtained regarding horizontal flows under supercritical pressure conditions still require further assessment to be supported by the new experimental works to understand the impact of buoyancy induced stratification of the fluid, and changes on heat transfer regime.

2.4 Numerical studies

Early DNS studies of wall-bounded flows focused on canonical flows started with periodic channel flow between two parallel, flat plates [21] and later followed by fully developed pipe flow [20]. These numerical experiments can be used to understand and perform detailed statistical analysis of turbulence. Later, it was possible to add temperature as a passive scalar for the incompressible flows, which were made it possible to calculate temperature-related statistics and turbulent heat flux [42]. These improvements opened path to DNS of more complex geometries where heating was included. Those analyses were made with the application of iso-flux or iso-thermal boundary conditions on the desired wall boundary. In fact, applying those boundary conditions resulted in different predictions of temperature related statistics, such as temperature variance and turbulent heat flux [43]. It has been observed that differences in the prediction of those statistics result in discrepancies in the near-wall region of the flow domain. Using the solid wall for heating purposes shows the behavior of the Robin boundary condition, which leads to a more accurate prediction [44]. These predictions are highly affected by the solid wall thickness and material properties. The measure thermal activity ratio K, is material (solid / fluid) based ratio to assess which material dominates how fast solid material reacts to the temperature changes compared to the fluid. Thermal activity term is calculated by the square root of the multiplication of material density, specific heat, and thermal conductivity [7].

$$K = \sqrt{\frac{k_f \rho_f c_{p_f}}{k_s \rho_s c_{p_s}}} \tag{2.46}$$

Previous studies showed that heat diffusion is highly sensitive to thermal activity ratio, however the responsiveness differs when it comes to wall thickness [45]. Especially for low-Prandtl number fluids, the effects of using conjugate heat transfer visible when dimensionless solid wall thickness d^+ greater than 10 [45], [46]. Dimensionless solid wall thickness mentioned can be calculated similarly to the dimensionless wall distance for fluid domain y^+ in Eq. 2.27 with the exact normalization approach by taking account of wall distance inside through solid wall.

$$d^+ = \frac{y_s u_\tau}{\nu_f} \tag{2.47}$$

These parameters altogether have direct impact on temperature fluctuations and turbulent heat flux [47]. The transition in between solid and fluid domains alters these statistics due to thermal resistance they apply. The change in thermal resistance results in different trend behavior for the both sides of the contacting wall surface.

Before we proceed with DNS studies on compressible flows, it is important to mention that the present literature survey focuses on low Reynolds number applications, mainly under supercritical pressure conditions. DNS studies with external flows are not discussed here and primarily focus is on internal channel flows. Changes in the thermophysical properties become important as flow subjected to external effects such as heating. Several works done with heated internal gas flow provided important reference for high resolution studies with supercritical flows [48], [49]. One of the remarkable studies in this context deals with testing prediction performance of RANS models against experimental data of internal gas flow [48], [50]. The study confirms that several RANS models can predict general flow behavior [51]. Later, high resolution simulations (LES and DNS) were utilized with air [52], [53] in which of pipe and annular pipe flows were investigated. One of the early examples of the use of tabulated thermophysical property data to introduce fluid properties was reported in these studies. It was confirmed that the use of thermophysical property tables is a robust method for high resolution numerical simulations with variable thermophysical properties [53].

Numerical studies with supercritical fluids are treated separately from the classical compressible flow simulations due to their strong thermophysical property changes in the pseudo–critical region (Fig 2.2). Early high-resolution computational studies with supercritical fluids were performed for vertical pipe flow [49] where sCO_2 is used as a working fluid. A fully developed turbulent flow field was first generated in periodic inflow part to feed the heated part. Boundary conditions for the inflow part were selected as the same as the study of Eggels et al. [20]. Mean flow statistics were examined in both the inflow and heated part. Nemati et al. utilized several cases where individual thermophysical property changes isolated to observe the independent contribution of thermophysical property variations [54]. Their study has reported mean statistics for the turbulence and heat transfer including bulk properties, turbulent stresses, turbulent heat flux, and production rate of turbulent kinetic energy on the heated part. Obtained statistics were used to provide a connection with the buoyancy effects as different stages of the heated part are examined in detail. Cao et al. [55] investigated the separate effects of buoyancy and thermal acceleration effects with the help of the mean statistics and turbulent kinetic energy production rate budgets. They connected deterioration and enhancement in heat transfer and turbulence to these mechanisms. Although they suggested an acceleration number for further judgment, it is not suitable for practical engineering use. He et al. [56] illustrated these mechanisms with a flow chart to explain more in detail and investigated transitions between deterioration and recovery in turbulence and laminarization events along with the heat transfer. In general, DNS studies performed with dedicated codes developed for this purpose as provided in presented literature. Nevertheless, similar works were conducted with OpenFOAM. The presented mean flow statistics indicate that the use of second order numerical schemes was sufficiently accurate to support detailed

investigations regarding turbulence and heat transfer [57], [58]. Most of the available studies focus on the vertical flows within pipe geometry. There are very few examples of the use of annular pipe flow heated from inside [59], [60] that uses sCO_2 as the working fluid. Those works have been set to relatively high Reynolds numbers, 8900 and 8000. Simulations were repeated to include several cases to observe effect of heating, buoyancy, and the use of constant thermophysical fluid properties as provided for the heated pipe flow [54]. The behavior of the turbulent structures was analyzed to assess how the local turbulence characteristics change within different conditions. Peeters et al. [60], [61] further investigated the effect of varying thermophysical properties by separating them to determine the effect of varying density and viscosity of the fluid [60]. Conclusions made provided more insight into how the buoyancy is connected with laminarization and turbulence recovery. Their detailed investigations allowed them to identify heat sweep and ejection mechanisms. Later, these studies were repeated for supercritical water [62], [63]. DNS results obtained were compared with predictions of heat transfer correlations at different heat flux levels.

The effect of buoyancy takes place differently in horizontal flows than in vertical flows. In horizontal circular pipe flows, it leads to thermal stratification on the upper levels of the flow cross section due to secondary flows induced by buoyancy. There are fewer DNS studies of horizontal supercritical flows than their vertical counterparts. As the secondary flow is not aligned with the flow direction, heat transfer and turbulent structures are weakened more strongly on the upper side of the pipe wall rather than the bottom side [64]. Therefore, heat accumulation along the gravitational direction shows different trends as heated fluid accumulates on the top side of the wall. This accumulation is called stratification that requires a separate evaluation for top and bottom wall regions, unlike vertical flows showing symmetric behavior at the same elevation. Also, the choice of inlet temperature requires some attention. The selection of inlet temperature may affect early temperature rise along the flow channel depending on how close to pseudo-critical region. The initial rise at the beginning of the heated part may result in rapid rise of wall temperature that makes it impossible to observe the characteristic changes in the pseudo-critical region. This immediate jump is observed in the study of Wang et al. [65] where supercritical water is used as working fluid.

Heat was mainly imposed by iso-flux boundary conditions applied to the wall surface in studies mentioned above. The use of conjugate heat transfer (CHT) in high resolution simulations with supercritical fluids is not common in the current available literature. Pucciarelli et al. [66], performed LES study where vertical heated flow between two flat plates is investigated. In the study, heating is uniformly applied to the far surface of the solid domain, which is delivered to the fluid domain by conduction. He et al., performed DNS with a relatively low Reynolds number without buoyancy effects [67]. Reynolds stresses and behavior of turbulent heat flux were investigated. Their investigation confirmed that the presence of the solid wall alters obtained statistics in comparison to non-CHT cases. The summary of DNS works dealing with supercritical flows available in the literature listed in the Table 2.1,

Table 2.1. List of DNS works mentioned as geometry & orientation, selected fluid, Re number.

	Geometry	Orientation	Fluid	Re
[50]	Pipe	Vertical	CO2	5400
[56]	Pipe		CO2	3540
[61]	Annular Pipe		CO2	8000
[57]	Pipe		CO2	2617
[65]	Pipe	Horizontal	CO2	5400
[59]	Pipe	Vertical	CO2	5400
[69]	Pipe		Water	5400
[68]	Pipe - CHT		CO2	3600

2.5 Summary

This chapter summarized the state of the art on high resolution studies dealing with turbulence and heat transfer under supercritical pressure. First, fundamental knowledge regarding turbulence and heat transfer was presented to support the interpretation of the DNS results provided in this study. Later, the current status of research on both experimental and numerical studies with supercritical flows was reviewed. Several gaps have been pointed out: the lack of DNS reference data for supercritical flows with horizontal orientation within the representative geometry for flow around nuclear fuel pin such as annular pipe flow heated from inside. Therefore, secondary flow mechanisms due to heating effects are not completely understood in given conditions. Another gap is the lack of DNS studies that utilize conjugate heat transfer under supercritical pressure conditions. Available literature focuses on the DNS cases with ideal boundary conditions to impose heating such as iso-flux or iso-thermal boundary conditions. The present thesis addresses these gaps by providing DNS of horizontal annular pipe flow with supercritical water where heat is imposed by conjugate heat transfer. The detailed numerical methodology used to perform direct numerical simulations within conjugate heat transfer is described in the following chapter.

3 Methodology

3.1 Simulation setup

3.1.1 Geometry

In this section, details of the DNS setup are described in terms of geometry, boundary conditions, thermophysical property treatment of selected materials and grid structure. As mentioned earlier, the simulation domain is created by values that originated from a SCWR design suggestion [8], [68] in which hydraulic diameter, fuel rod diameter, and cladding thickness are implemented without any changes. The flow area is arranged in an annular pipe flow geometry with a corresponding fuel assembly hydraulic diameter shown in Fig 3.1.

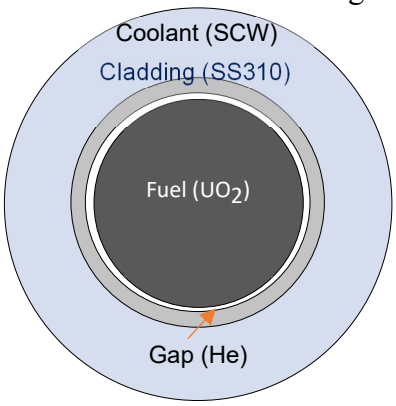

Figure 3.1. Cross-section of fuel rod and surrounding coolant flow area.

The cladding material is selected as SS310 for this study [69], [70]. The DNS domain with heated solid wall has been modeled including the coolant flow area with given hydraulic diameter and cladding material. In case of modeling approach for the DNS domain, it is important to assess whether temperature fluctuations are affecting other neighboring regions before reaching the coolant. The characteristic time for heat transfer (Eq. 3.1) [71], has been used for this assessment which can be calculated by dividing the square of the heat transfer thickness [68], [72] by the thermal diffusivity of the material. Additionally, thermal resistance (Eq. 3.2) for each region is calculated for each region.

$$\tau_{HT} = \frac{L_{HT}^2}{\alpha} \tag{3.1}$$

$$\Omega_{HT} = \frac{L_{HT}}{\lambda} \tag{3.2}$$

Table 3.1. Thermal diffusivity and characteristic time for heat transfer for He and SS310.

	UO_2 (1400 K [73])	He (6MPa [68], 645K)	$SS310$
$L_{HT}\ (m)$	0.00336	0.0001	0.00063
$\alpha\ (m^2/s)$	0.80×10^{-6}	1.17×10^{-5}	3.33×10^{-6}
$\lambda\ (W/mK)$	2.75	0.268	13.5
$\tau_{HT}\ (s)$	14.112	8.548×10^{-4}	0.119
$\Omega_{HT}\ (W/K)$	1.22×10^{-3}	3.730×10^{-4}	4.662×10^{-5}

Characteristic heat transfer times and thermal resistance values for fuel [74], [75], gap [9] and cladding [70] regions have been calculated within their thermophysical property values. Calculated values are presented in table 3.1.

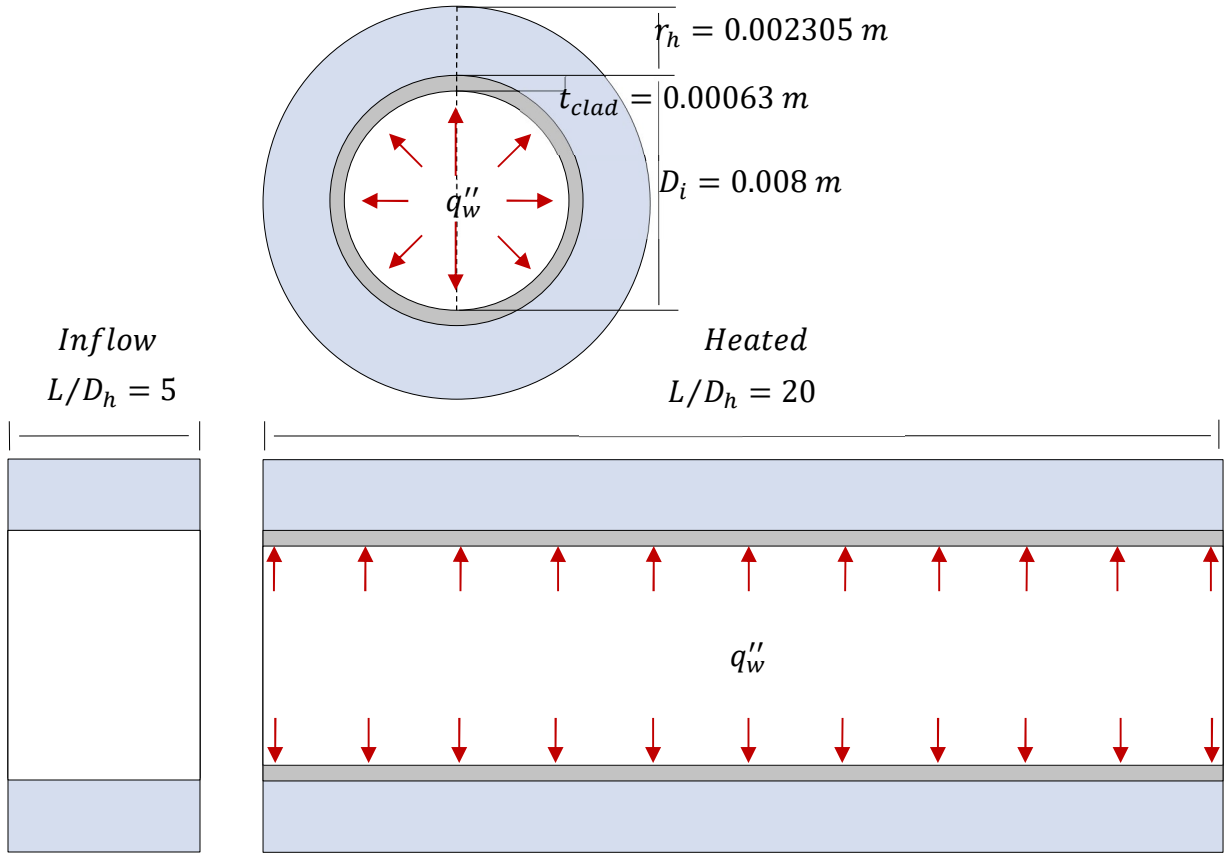

Figure 3.2. Representative sketch of the simulation domain.

The characteristic time for heat transfer is significantly smaller for gas gap (Helium) than for the cladding material (SS310) across in their thicknesses while fuel exhibits the largest value. It means that the gap region immediately responds to temperature fluctuations received from the fuel region. However, cladding materials higher characteristic time value than gap region makes it slower to respond these temperature fluctuations and eventually dampening them. Meanwhile, thermal resistance is dominated by fuel and gap regions, where most of the radial temperature drops from the fuel centerline to the outer surface of the cladding occurs in these regions. The modeling of the gap region would have negligible effect on the temperature statistics as temperature fluctuations would be delivered to the inner surface of the cladding. At this point, modeling of the fuel region is not expected to alter the coolant side thermal statistics rather than iso-flux boundary condition. The final setup is constructed with only the coolant (supercritical water) and cladding material as (SS310) solid domain. The general structure of the simulation domain is given in Figure 3.2.

The fluid domain is divided into two parts: inflow and heated part. It is necessary to separate the fluid section to ensure that the heated part receives a fully developed turbulent flow field before any heating is applied. A fully developed turbulent flow field for inflow part is achieved by distorting velocity field with random turbulent structures until turbulence becomes statistically stationary. These structures (vortices) in the inflow part are maintained by streamwise periodic boundary condition at fixed bulk Reynolds number that is used to feed the heated part. In this way, the heated part is provided by a time resolved, fully turbulent flow field with the constant mass flux. These settings attenuate the unwanted artefacts of using synthetic turbulence such as lack of random turbulent structures, and excessive or weak turbulent streaks. In addition to the fully developed turbulent flow field (velocity field), temperature inside the inflow part is kept constant at the selected inlet temperature ensure there is no possible numerical errors affecting inflow part related with energy equation. No additional effects are introduced for the outlet section of the domain. The only measure taken is to extend the heated length by 2 hydraulic diameters to eliminate outlet effects that might occur during the simulation. The heated part is 9.22 cm in length and 1.26 cm at the outer diameter. Strong pressure changes in a tube of such a small size are not expected. For this reason, boundary conditions are set to constant pressure at 25 MPa. This assumption leads to a constant-pressure simulation domain, allowing the numerical scheme to reach convergence more easily.

3.1.2 Implementation of thermophysical properties of supercritical water

Thermophysical properties of supercritical water have been introduced into the simulation setup as tabulated data based on temperature and pressure. Data have been provided by the REFPROP [9] database, which has been proven to be a robust approach in previous studies [57], [63]. Yet, it is vital to ensure uncertainty is kept under reasonable limits when the solver needs to interpolate between predefined temperature points. An uncertainty analysis was performed on the specific heat values that have the highest variations in the pseudo–critical region among all thermophysical properties concerned.

$$c_{p_{value}} = c_{p_{low}} + \frac{(T_{value} - T_{low})\left(c_{p_{high}} - c_{p_{low}}\right)}{\left(T_{high} - T_{low}\right)} \tag{3.2}$$

The procedure relies on linear interpolation, when the solver needs thermophysical property data at temperatures not directly listed in the provided thermophysical property table. Linear interpolation is performed for the corresponding temperature value to calculate thermophysical property values. Process covers the temperature linked data in between the closest higher and lower temperatures provided in the tabulated data. Visual process of the determination of values for different sampling frequencies is illustrated in Fig. 3.3.

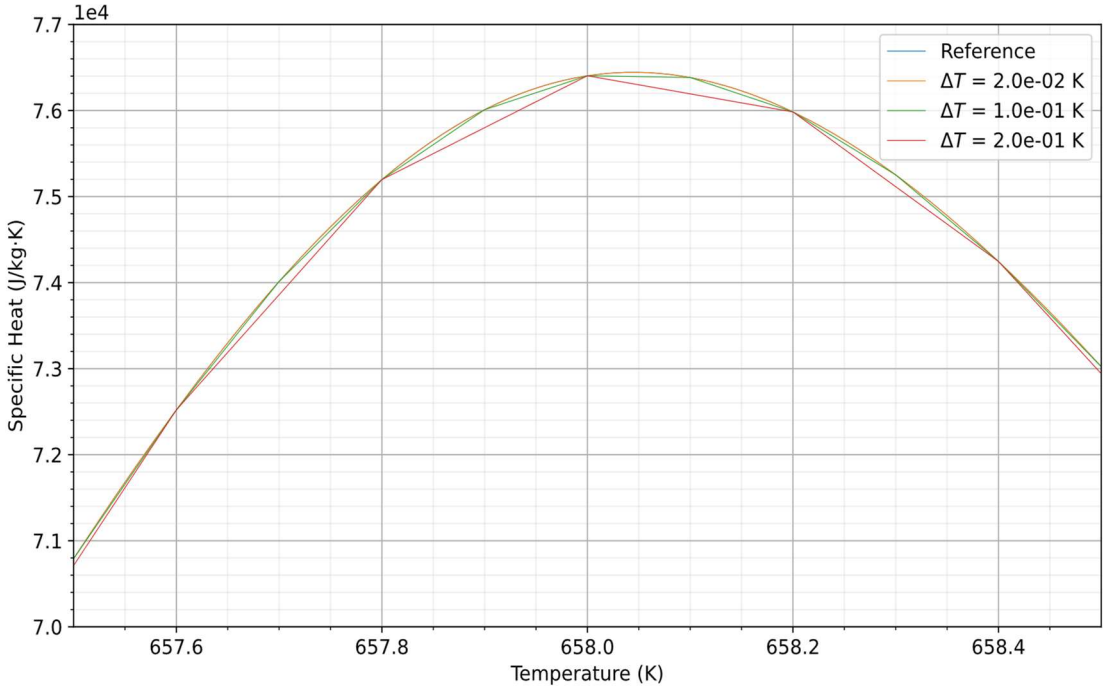

Figure 3.3. Example plot with specific heat values to demonstrate how the interpolation procedure works with the provided data (reference: Data set with 1e-5 K temperature step).

Interpolated values pose an error in comparison to reference properties as shown in Figure 3.3. Accuracy increases as thermophysical property data sampled in higher frequency for each temperature. The highest discrepancies between interpolated data and reference samples are observed in interpolation specific heat values that peak in the pseudo-critical region. Therefore, the selection of sampling frequency made by considering the specific heat related error.

$$\epsilon_{max} = max\left(\frac{\left|C_p^{data} - c_p^{ref}\right|}{c_p^{ref}}\right) \times\ 100\,\% \tag{3.3}$$

$$\epsilon_{mean} = mean\left(\frac{\left|C_p^{data} - c_p^{ref}\right|}{c_p^{ref}}\right) \times\ 100\,\% \tag{3.4}$$

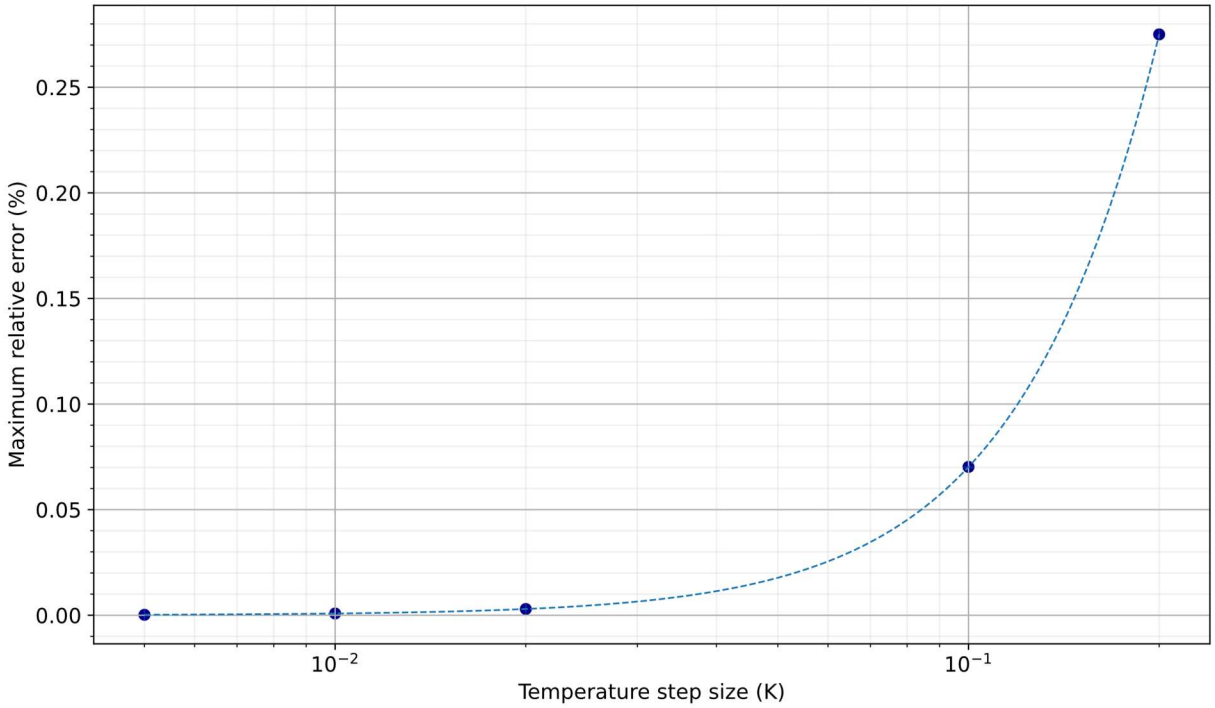

Figure 3.4. Maximum pointwise relative error of specific heat compared to the temperature step.

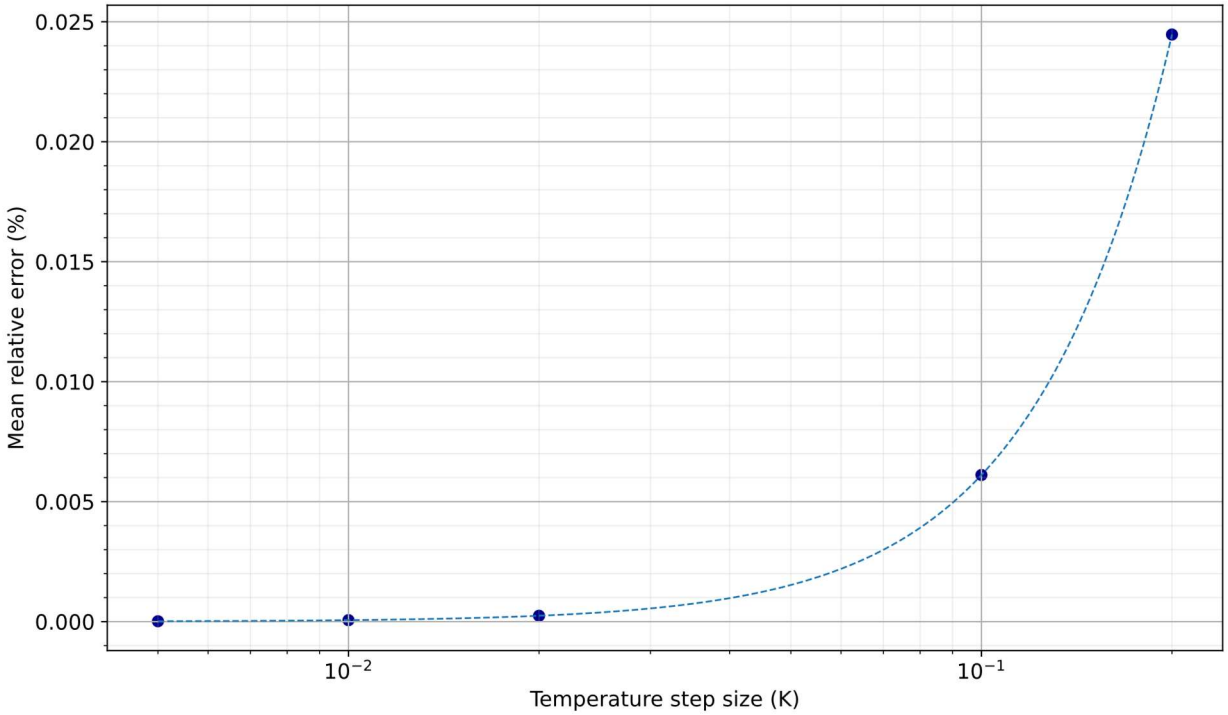

Figure 3.5. Mean pointwise relative error of specific heat compared to the temperature step.

The maximum observed relative error (Eq. 3.3) corresponds to approximately ten the mean relative error (Eq. 3.4) values recorded. Trend curves are added to Figures 3.4 and 3.5 to illustrate how the error value develops with the sampling frequency. However, the increase in the sampling frequency brings additional computational cost. Mean error values reach the order of 0.00001% if

the sampling frequency is increased to the point that temperature step becomes 0.0005 K. It is deemed sufficient for this study to keep the sampling frequency at a temperature step of 0.02 K, which provides a mean relative error of 0.0025% in the interpolation of the thermophysical data.

Unlike in the fluid domain, a constant thermophysical property is provided for the solid domain. The following thermophysical properties are used for cladding material SS310 [70].

Table 3.2. Thermophysical properties of SS310 for solid domain.

$\rho_s\ (kg/m^3)$	$\lambda_s\ (W/mK)$	$C_{v\,s}\ (kJ/kgK)$
7940	13.5	510

3.1.3 Grid structure

As the purpose of DNS (numerical experiment) to resolve all turbulent scales ideally, the computational grid must be constructed accordingly. Turbulent scales tend to dissipate into smaller scales as they appear. This process continues until the smallest scales of turbulence and dissipation into heat energy. There are three scales of turbulence (Kolmogorov scales) known as length, velocity, and time scales [11].

$$\eta = \left(\frac{\nu^3}{\varepsilon}\right)^{\frac{1}{4}} \tag{3.5}$$

$$u_\eta = (\varepsilon\nu)^{\frac{1}{4}} \tag{3.6}$$

$$\tau_\eta = \left(\frac{\nu}{\varepsilon}\right)^{\frac{1}{2}} \tag{3.7}$$

The term ε refers to the dissipation rate of turbulence. It can be calculated by following approximation [76],

$$\varepsilon = \frac{C_\mu^{0.75} k^{1.5}}{L} \tag{3.8}$$

Where k is turbulent kinetic energy, L is characteristic length and C_μ is a constant value of 0.09.

$$k = \frac{3}{2}\left(0.16\mathrm{Re}^{-0.125} U_b\right)^2 \tag{3.9}$$

$$L = 0.07 D_h \tag{3.10}$$

The ideal measure DNS suitable grid structure is that grid spacing should be close to Kolmogorov length scale to capture/resolve smallest turbulence scales (Eq. 3.11).

$$\Delta x/\eta \cong 1 \tag{3.11}$$

Yet, this condition significantly increases the computational cost to perform DNS. As the smallest eddies correspond to a negligibly small portion of turbulent kinetic energy, S. Pope [11] suggested that this criterion can be relaxed up to a ratio of 2.1 for homogeneous turbulence. The relaxed limitation of the ratio 2.1 has been extended further to larger values in recent DNS works made under supercritical pressure conditions up to ratios of 6 – 9.5 [57], [59], [62]. However, turbulent statistics obtained in these works are in good agreement with the law of the wall (Eq. 2.29-2.30).

In case of wall bounded flows, cell grading at the near wall region is needed to resolve all relevant scales of turbulence, otherwise either DNS becomes either impractical due to its computational cost or fails to resolve all relevant scales. Their relaxed approach on the grid structure still enables them to obtain turbulent statistics in good accuracy. The relaxation of these limits can be compensated through regional cell grading. Turbulent scales appear to be smaller (but larger in number) at the near wall region rather than core flow. For this reason, grid cells can be arranged to be smaller at the near wall regions and larger by the distance to the nearest wall for the rest of the flow domain. The hyperbolic tangent function (Eq. 3.12) is used to distribute cell locations in the radial direction [59].

$$\frac{r}{\delta} = \frac{r_i}{\delta} + \left(1 - \frac{tanh\left\{\gamma\left[1 - \frac{2(j-1)}{N_2 - 1}\right]\right\}}{tanh(\gamma)} \right) \tag{3.12}$$

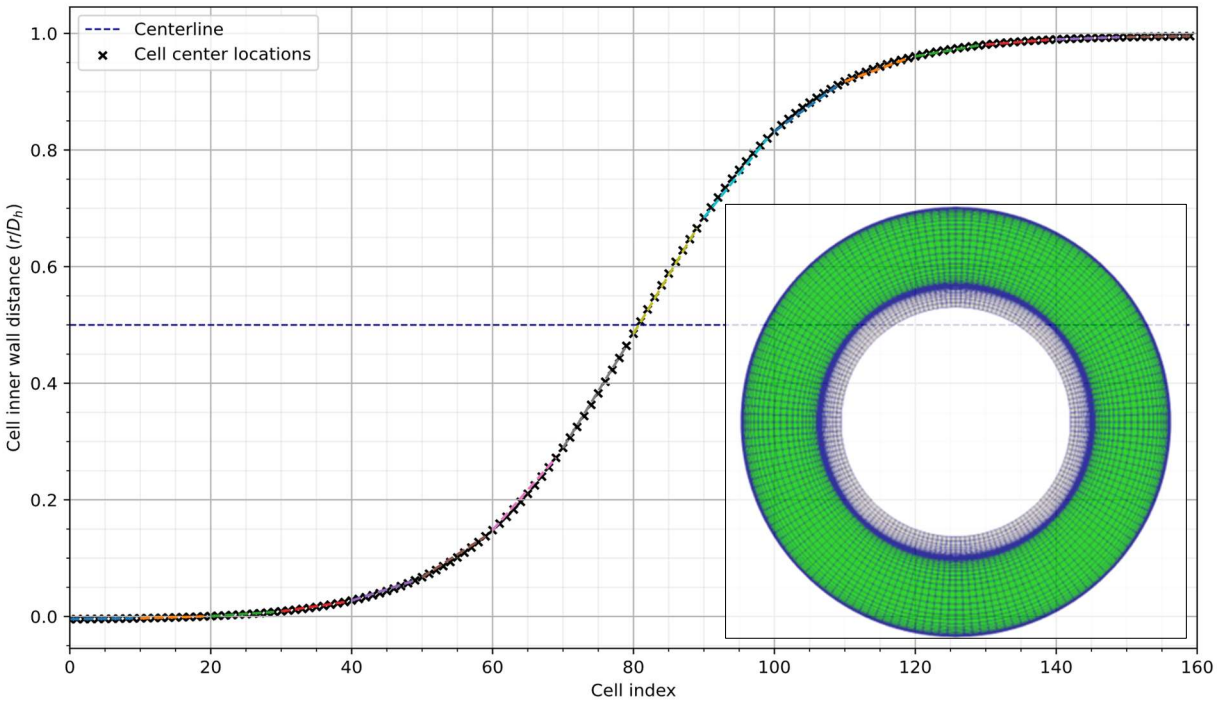

Figure 3.6. Distribution of cells by cell number and inner wall distance locations.

The tangential function provided allows re-distribution of the cells in radial direction. In Fig. 3.6, the respective locations of the cells in the annular gap were plotted to illustrate how cells are stationed in radial direction. Their distribution kept uniform and evenly distributed in streamwise

and angular directions. The representative picture of grid structure for annular cross section including solid domain is shown on the right-hand side of Figure 3.6.

Another restriction lies in the selection of time step to perform DNS. The principle is to perform the DNS with a time step small enough to fluid particles move only a fraction of the cell size during one time step ($\Delta\tau$) in average. As every movement of the fluid particles tracked cell by cell, it is possible to capture the smallest relevant turbulent structures. Relevant statistics for the established grid structure are given in Table 3.3.

Table 3.3. Fluid region grid resolution is relative to local Kolmogorov scales.

$\Delta z/\eta$	1.42
$\Delta r/\eta$	0.005 – 0.95
$\Delta\theta/\eta$	1.74 – 2.75
$\Delta\tau/\tau_\eta$	0.0113

The fluid region grid mostly satisfies Pope's criterion by drawing close to 2.1 which is an acceptable compromise according to the provided examples from literature. In the solid part, cells are structured with linear grading where they are set to be conformal with fluid mesh. Global statistics of the grid structure can be summarized in Table 3.4,

Table 3.4. Global grid for regions and simulation domain.

$z \times r \times \theta\ (inflow)$	$360 \times 160 \times 320$	18.4 M
$z \times r \times \theta\ (heated)$	$1440 \times 160 \times 320$	73.7 M
$z \times r \times \theta\ (solid)$	$1440 \times 40 \times 320$	18.4 M

3.2 Boundary and initial conditions

Cases were determined according to the required computational cost, and the similarity was constructed using a SCWR design suggestion by KIT [8]. A secondary criterion was that cases should provide information for physical events in the pseudo-critical region. The first analysis was conducted to investigate temperature rise in the streamwise direction along the heated annular pipe section. Operating pressure, hydraulic diameter, and heated (fuel) rod diameter are the same as in selected SCWR design suggestion. The computational cost of DNS makes it impractical to perform DNS at very high Reynolds numbers. Therefore, Reynolds number as 5400 for DNS case to be utilized. The number selected through concerns regarding computational cost and to align this study with other DNS works dealing with supercritical flows [57], [63]. The heat flux to be applied was determined under the limitations of DNS while preserving similarity to the SCWR conditions. Data considered for the similarity can be found below,

Table 3.5. Selected parameters from SCWR design suggestion by KIT [8].

$q''_{avg}\ (kW/m^2)$	$q''_{max}\ (kW/m^2)$	$D_h(m)$	$G(kg/m^2s)$
775	1550	0.00461	2024.25

Table 3.6. Preliminary initial & boundary conditions for DNS fluid domain.

Re	$T_0(K)$	$P(MPa)$	$G(kg/m^2s)$
5400	645	25	66.24

Material properties of the fluid and solid were kept the same for both SCWR design suggestion and DNS setup. The next step was to set the temperature drop between wall temperature and bulk flow temperature the same for both.

$$(T_w - T_b)_{SCWR} \approx (T_w - T_b)_{DNS} \tag{3.13}$$

In this way, it is possible to observe the transition of fluid temperature through pseudo-critical region in the radial direction. As the condition $T_b < T_{pc} < T_w$ is satisfied in the DNS setup, the similarity link to SCWR design suggestion can be made over heat transfer coefficient. HTC is calculated by the relation $HTC = q_w''/(T_w - T_b)$. Accordingly, the condition that was given in Eq. 3.13 can be rewritten as follows,

$$\left(\frac{q_w''}{HTC}\right)_{SCWR} \approx \left(\frac{q_w''}{HTC}\right)_{DNS} \tag{3.14}$$

Here, HTC was replaced with Nusselt number by its definitive formulation.

$$\left(\frac{q_w''}{\frac{\lambda Nu}{D_h}}\right)_{SCWR} \approx \left(\frac{q_w''}{\frac{\lambda Nu}{D_h}}\right)_{DNS} \tag{3.15}$$

In the next step, DB correlation was used to interpret the similar relation by Reynolds number between SCWR conditions and DNS setup. Other parameters regarding flow conditions are provided at Tables 3.5 and 3.6.

$$\left(\frac{q_w''}{0.023Re^{0.8}Pr^{0.4}\frac{\lambda}{D_h}}\right)_{SCWR} \approx \left(\frac{q_w''}{0.023Re^{0.8}Pr^{0.4}\frac{\lambda}{D_h}}\right)_{DNS} \tag{3.16}$$

The hydraulic diameter has been chosen identical with SCWR design suggestion. Also, the assumption of equal temperature difference from wall surface to bulk flow still held. Parameters λ, Pr, D_h are cancelled out to complete similarity relation. The final form of the relation simplified into the ratio of wall heat flux over 0.8 power of Reynolds number.

$$\frac{q_{w-SCWR}''}{Re_{SCWR}^{0.8}} \approx \frac{q_{w-DNS}''}{Re_{DNS}^{0.8}} \tag{3.17}$$

The average and maximum values of the heat flux to be applied were found as 49.903 and $99.806\,kW/m^2$. These values were utilized to the DNS setup as 50 and $100\,kW/m^2$ for simplicity. Later, the selection of inlet temperature was revisited to observe the phenomenon expected to happen in supercritical conditions. In this regard, two criteria have been set as priorities:

- Transition through the pseudo-critical region should be observed from the heated wall to the bulk region. The heated wall temperature should exceed the critical temperature, while the bulk temperature must stay below this limit.
- The influence of inlet temperature, heating flux, and presence of gravity should be distinguishable.

As a first step, the rise in the bulk enthalpy along the streamwise direction was calculated to make such an assessment.

$$h_{b,out} = h_{b,in} + \frac{A_{HT} q''_{avg}}{\dot{m}} \tag{3.18}$$

As the enthalpy rise along the annular pipe was calculated, the bulk temperature rise has been inferred from this information. Later, streamwise bulk temperature and corresponding predicted wall temperature have been estimated by obtaining an iterative solution of wall temperature using Bishop correlation and definitive formula for the Nusselt number.

$$Nu_{Bishop} = 0.0069 Re^{0.9} \overline{Pr}^{0.66} \left(\frac{\rho_w}{\rho_b}\right)^{0.43} \left(1 + 2.4\frac{D_h}{x}\right) \equiv \frac{q''_{avg} D_h}{\lambda(T_b - T_{wall})} \tag{3.19}$$

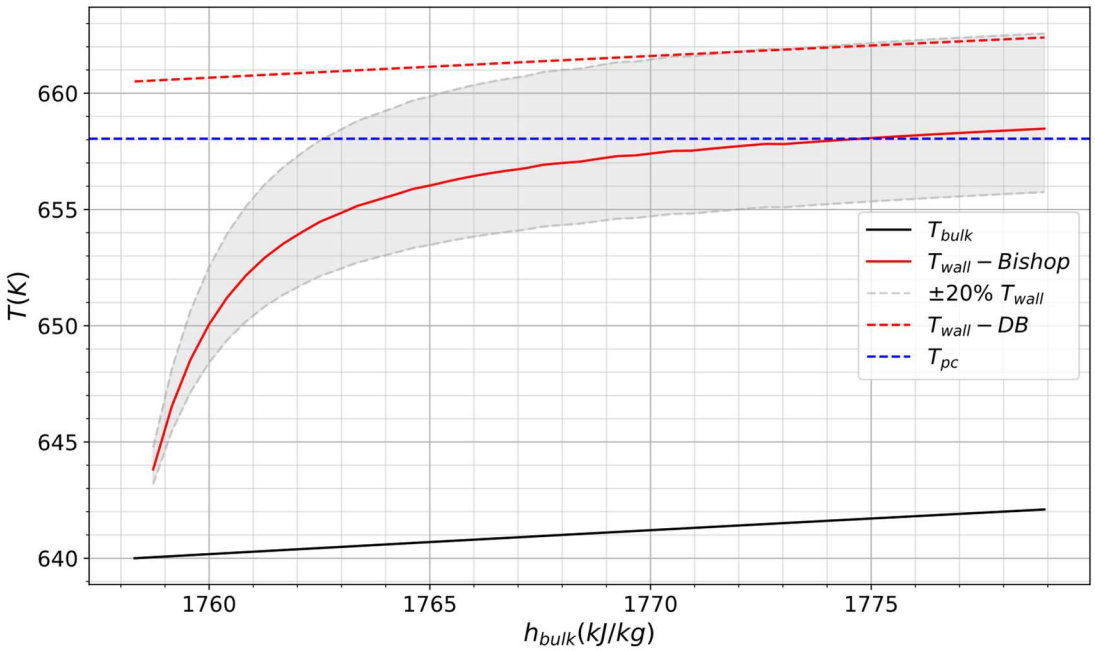

Figure 3.7. Rise in the bulk enthalpy and respective temperature profile in streamwise direction for $T_0 = 640\ K$.

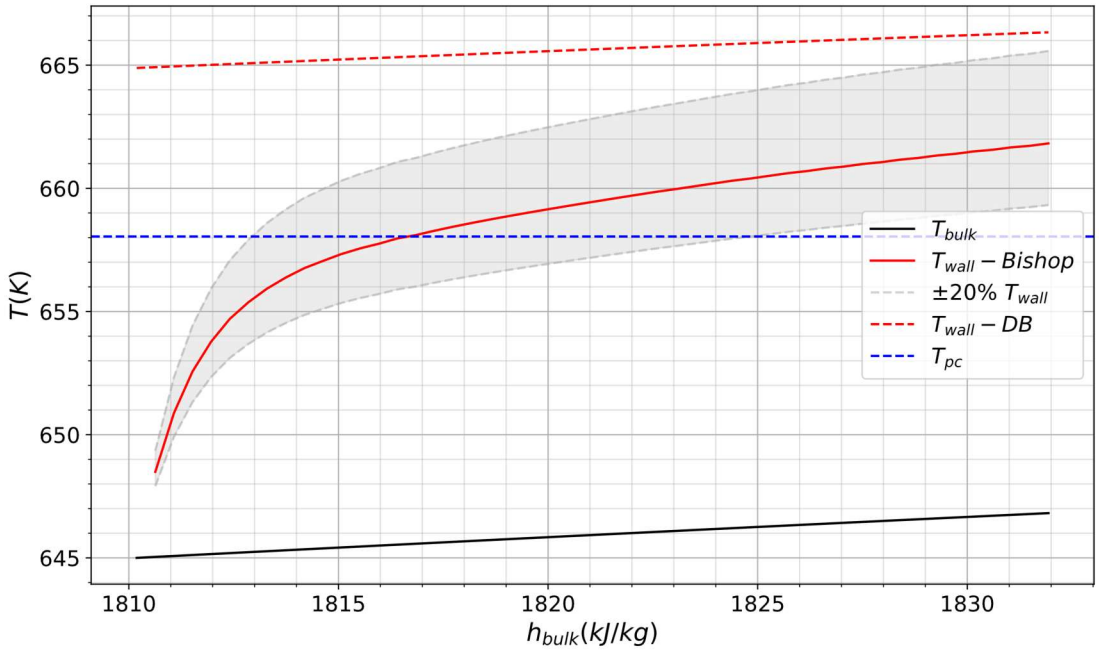

Figure 3.8. Rise in the bulk enthalpy and respective temperature profile in streamwise direction for $T_0 = 645K$.

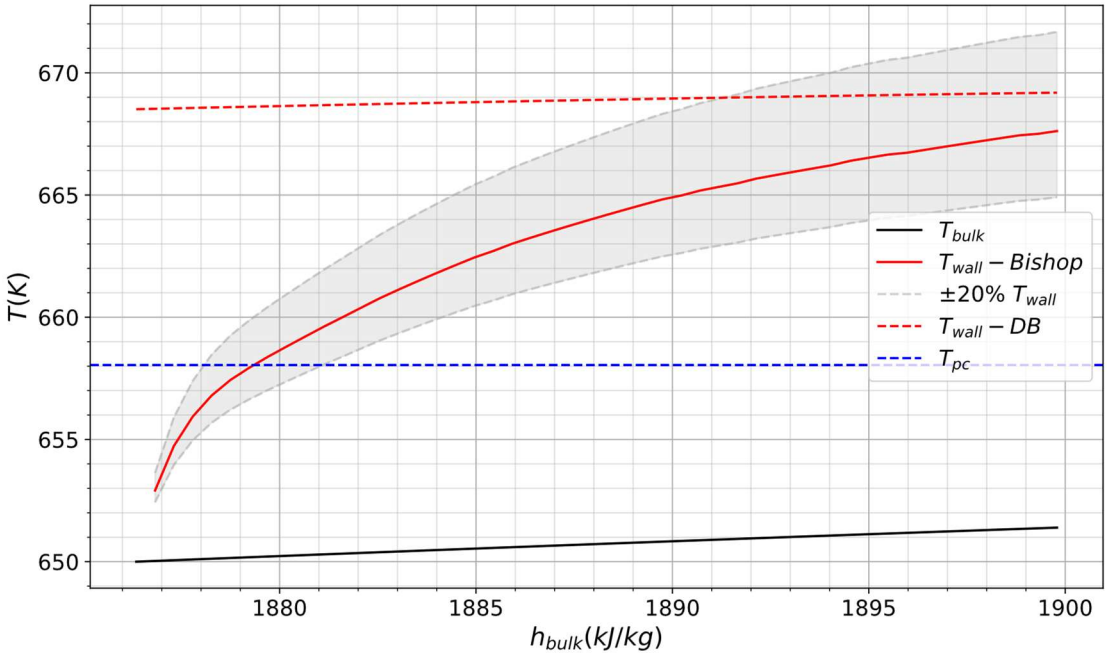

Figure 3.9. Rise in the bulk enthalpy and respective temperature profile in streamwise direction for $T_0 = 650K$.

As the criterion for the DNS cases to observe the temperature profile covering the pseudo-critical region and possible heated length is restricted by the computational resources available, the initial temperature is selected very close to this region. Analysis made for three different inlet temperature values as T_0=[640, 645, 650] K.

Smaller initial temperature provides more range to investigate the region remaining below the critical temperature point. Yet, it is important to stay in the range of pseudo–critical region range for the purpose of this study. Regardless of the initial temperature, an immediate jump appears at the beginning of the heated length. The crossing point location for the critical temperature is two-thirds of the heated length when $T_0 = 640K$ Fig. 3.7 selected, one-third when $T_0 = 645K$ (Fig. 3.8). For $T_0 = 650K$ (Figure 3.9), it is clear that the wall temperature immediately crosses T_{pc} point at the beginning of the heated part. Therefore, it represents limited information about the development of events regarding turbulence and heat transfer that might be happening in the lower edge of the pseudo–critical region.

Their different T_{pc} point crossing locations allow us to investigate the physical changes in the fluid within different length intervals in the heated part. Additionally, two other cases are included to investigate the effect of heat flux and the presence of the gravity for further analysis. The list of the cases determined has been given in the Table 3.7.

Table 3.7. DNS case matrix.

Short Name	Case (T:Q:G)	$T_0(K)$	$q''_{wall}\ (kW/m^2)$	$Buoyancy$
Case 1	640-050-G	640	50	Yes
Case 2	645-050-G	645	50	Yes
Case 3	645-100-G	645	100	Yes
Case 4	645-050-N	645	50	No
Case 5	650-050-G	650	50	Yes

Case name format $T: Q: G$ where $T \rightarrow T_0,\ Q \rightarrow q''_w$, Gravity (G:on,N:off).

The physical (conceptual) boundary conditions are defined, and their numerical implementation for the DNS setup is summarized for fluid and solid in Tables 3.8 and 3.9.

Table 3.8. DNS setup fluid domain boundary conditions.

Fluid	Boundary	U	T	P
Inflow	Inner wall	$U = 0$	$\partial T/\partial x_n = 0$	$\partial P/\partial x_n = 0$
	Outer wall			
	Inlet	$U\|_{inlet}^{inflow} = U\|_{outlet}^{inflow}$	$T = T_0$	$\partial P/\partial x_n = 0$
	Outlet		$\partial T/\partial x_n = 0$	$P = 25\ MPa$
Heated	Inner wall	$U = 0$	$T_f = T_s,$ $\lambda_f\ \partial T_f/\partial x_i = \lambda_s\ \partial T_s/\partial x_i$	$\partial P/\partial x_n = 0$
	Outer wall		$\partial T/\partial x_n = 0$	
	Inlet	$U\|_{inlet}^{heated} = U\|_{outlet}^{Inflow}$	$T = T_0$	
	Outlet	$U_z \geq 0, \quad \partial U/\partial x_n = 0$ $U_z < 0, \quad$ -	$\partial T/\partial x_n = 0$	$P = 25\ MPa$

Table 3.9. DNS setup solid domain boundary conditions.

Solid	Boundary	T
Heated	Inner wall	$T_f = T_s, \quad \lambda_f\ \partial T_f/\partial x_i = \lambda_s\ \partial T_s/\partial x_i$
	Outer wall	$\partial T/\partial x_n = 0$

As the both conceptual and numerical boundary conditions were specified, the DNS setup was constructed within the grid structure defined for the representative geometry of flow around nuclear fuel pin.

3.3 Governing equations

As the computational domain has been provided, governing equations for the fluid and the solid region are different. Additionally, budgets for transport equations for turbulent kinetic energy, turbulent heat flux were calculated in the post-processing of the results.

3.3.1 Governing equations for fluid

Conservation of mass,

$$\frac{\partial \rho}{\partial t} + \frac{\partial (\rho u_i)}{\partial x_i} = 0 \tag{3.20}$$

Conservation of momentum,

$$\frac{\partial (\rho u_i)}{\partial t} + \frac{\partial \left(\rho u_i u_j\right)}{x_j} = -\frac{\partial p}{\partial x_i} + \frac{\partial}{\partial x_j}\left[\mu\left(\frac{\partial u_i}{\partial x_j} + \frac{\partial u_j}{\partial x_i}\right) - \frac{2}{3}\mu\delta_{ij}\frac{\partial u_k}{\partial x_k}\right] + \rho g_i \tag{3.21}$$

Conservation of energy,

$$\frac{\partial (\rho h)}{\partial t} + \frac{\partial \left(\rho u_j h\right)}{\partial x_j} = \frac{\partial}{\partial x_j}\left(\frac{\lambda}{\rho c_p}\frac{\partial h}{\partial x_j}\right) \tag{3.22}$$

These equations were discretized and solved numerically to solve turbulent flow field.

3.3.2 Governing equations for solid

Heat diffusion equation was solved in the solid domain.

$$\rho c_p \frac{\partial T}{\partial t} + q = \frac{\partial}{\partial x_j}\left(k\frac{\partial T}{\partial x_j}\right) \tag{3.23}$$

As the energy equation for these two regions was solved, the coupling mechanism between them to exchange temperature information on the interface (heated inner wall surface of fluid domain) was managed as given below. Each domain is marked with their first letters.

$$\begin{aligned} T_f &= T_s \\ \lambda_f \frac{dT_f}{dx_n} &= \lambda_s \frac{dT_s}{dx_n} \end{aligned} \tag{3.24}$$

3.3.3 Budgets of transport equations

The transport equation for turbulent kinetic energy is used to compute the budget terms from the DNS results. The budget terms for diffusion, production, buoyancy, and dissipation of turbulent kinetic energy were used to understand how turbulent kinetic energy (or turbulence) affected under the observed effects of buoyancy, flow stratification, thermal acceleration and laminarization.

Budgets for the transport of turbulent kinetic energy [77],

$$\frac{\partial k}{\partial t} + \overline{U_i}\frac{\partial k}{\partial x_i} = \underbrace{-\frac{1}{2}\frac{\partial \overline{u_j' u_j' u_i'}}{\partial x_i}}_{D_{Turb}^{TKE}} + \underbrace{\upsilon \frac{\partial^2 k}{\partial x_j^2}}_{D_{Mol}^{TKE}} - \underbrace{\left(\overline{u_i' u_j'}\frac{\partial \overline{U_i}}{\partial x_j}\right)}_{P^{TKE}} - \underbrace{\frac{g_i}{\overline{\rho}}\overline{\rho' u_i'}\delta_{i3}}_{B^{TKE}} - \underbrace{\upsilon \overline{\frac{\partial u_i'}{\partial x_j}\frac{\partial u_i'}{\partial x_j}}}_{\varepsilon^{TKE}} \tag{3.25}$$

The buoyancy production term has been redefined by using Boussinesq approximation for buoyant flows [78], since the system kept in constant pressure and density fluctuations are only dependent on temperature.

$$\rho' = \rho_0 \beta T', \; where \; \beta = -\frac{1}{\rho}\beta\frac{\partial \rho}{\partial T} \tag{3.26}$$

In further step, mean density was assumed equal to initial density in the time step ($\overline{\rho} \approx \rho_0$). Buoyancy term takes the form,

$$B = -\beta g_i \overline{u_i' T'}\,, \; g_i = [0 \; -9.81 \; 0] \tag{3.27}$$

This form by Boussinesq approximation was used to evaluate buoyancy budget contribution for turbulent kinetic energy.

Budgets for the transport of turbulent heat flux calculated similarly to the turbulent kinetic energy for further assessment [44], [79].

$$\begin{aligned}\frac{\partial \overline{u_i' T'}}{\partial t} + \overline{U_j}\frac{\partial \overline{u_i' T'}}{\partial x_j} = & -\frac{\partial}{\partial x_j}\left(\underbrace{\overline{u_i' u_j' T'}}_{D_{Turb}^{THF}} - \underbrace{\kappa \overline{u_i' \frac{\partial T'}{\partial x_j}}}_{D_{Mol}^{THF}} - \underbrace{\nu \overline{T' \frac{\partial u_i'}{\partial x_j}}}_{D_{Ther}^{THF}}\right) \\ & - \left(\underbrace{\overline{u_i' u_j'}\frac{\partial \overline{T}}{\partial x_j}}_{P_1^{THF}} + \underbrace{\overline{u_j' T'}\frac{\partial \overline{U_i}}{\partial x_j}}_{P_2^{THF}}\right) - \underbrace{(\nu + \kappa)\overline{\frac{\partial u_i'}{\partial x_j}\frac{\partial T'}{\partial x_j}}}_{\varepsilon^{THF}}\end{aligned} \tag{3.28}$$

In both transport equations, the diffusion terms represent diffusive redistribution of a quantity on the sampled location whether it is being exported or imported between neighboring locations. The production terms define if the quantity is being produced or destroyed by the corresponding mechanism. Lastly, the dissipation term symbolizes the rate of the quantity being irreversibly

dissipated to internal energy of the fluid. These budget terms are computed to analyze their connection to flow events in the heated turbulent flow mentioned above in supercritical pressure conditions.

3.4 Numerical schemes

OpenFOAM is structured as an open-source finite volume code open for further development. In the finite volume method, the domain to be solved is split into small cells to solve finite differential equations like Navier–Stokes equations. A backward differencing scheme was selected for time discretization in the current numerical setup. The "backward Euler method" provides more stability compared to explicit schemes for calculations made for problems with complex physics [80]. Unlike the Euler method, it has an implicit structure and provides second-order accuracy. Gauss linear integration was selected to solve gradient, divergence, and Laplacian schemes. These settings allow us to solve the system spatially with second-order accuracy. Some of the selected schemes were modified with the LUST (Linear Upwind Stabilized Transport) option due to its stability to solve complex solution schemes for velocity and energy. Sufficient order of accuracy has reached using second order schemes for both temporal and spatial discretization, as tests showed that third and fourth-order schemes did not improve turbulent statistics. Governing equations were solved with the PISO (The Pressure Implicit with Splitting of Operator) algorithm [81] to solve pressure – velocity coupling. PISO method was initially introduced for transient compressible flows that solve pressure and velocity terms [82]. The algorithm solves the discretized momentum equation in the first attempt and computes mass flux values at the cell faces. Then it proceeds to solve the pressure equation and updates mass flux values, velocity, and energy terms. As convergence is reached, the solution advances to the next time step [83].The numerical methods listed are summarized in Table 3.10.

Table 3.10. The list of numerical schemes used for DNS setup.

	Fluid	
Task	Method	Order
Time discretization	Backward Euler	2
Convection	Gauss LUST	2
Diffusion	Gauss Linear corrected	2
Gradient	Gauss linear	2
Interpolation	Gauss linear	2
	Solid	
Time discretization	Backward Euler	2
Diffusion	Gauss Linear corrected	2

3.5 Verification of the numerical setup

OpenFOAM has been successfully utilized for high resolution simulations in various applications, including supercritical flows in the current state of the art. However, the specific simulation setup used in this study must be verified that includes the combination of selected boundary conditions, grid configuration, thermophysical property treatment, and numerical scheme selection. In order to do this, reproducing a similar study dealing with direct numerical simulation under supercritical pressure conditions within the vertical annular pipe geometry is selected for verification process [59]. In their study, the flow region was also separated into two parts as inflow and heated. Given simulation setup was applied in the course of the verification of the inflow section by means of mean and second order statistics. Flow conditions and grid resolution for both cases given in Table 3.11.

Table 3.11. Boundary, grid size for validation case versus reference DNS case.

	Verification Case	Reference Case [59]
Fluid	$CO2\ at\ 8\ MPa, Re = 8900, T_0 = 301.15K$	
Geometry ($z \times r \times \theta$)	$5\pi\delta \times 2\delta \times 0.5\pi\delta$	
Grid Size ($z \times r \times \theta$)	$130 \times 130 \times 520$	$129 \times 137 \times 516$

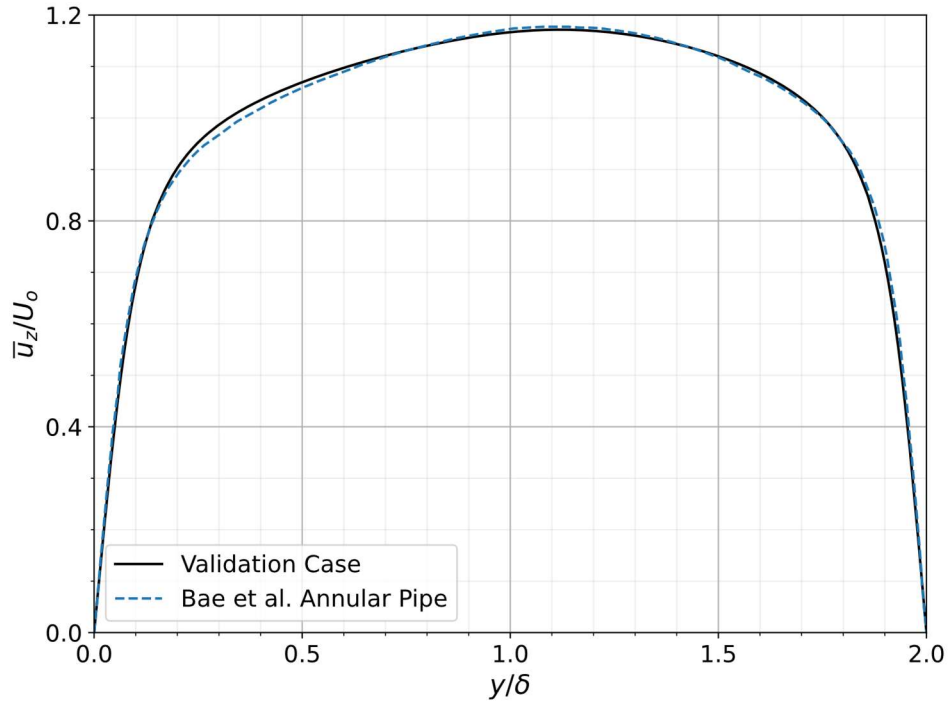

Figure 3.10. The distribution of the mean streamwise velocity plotted with the wall-normal distance.

The test conducted was in good agreement with reference case for distribution of the streamwise velocity. The streamwise velocity profile through annular gap reproduced by the verification case shown in Fig. 3.10.

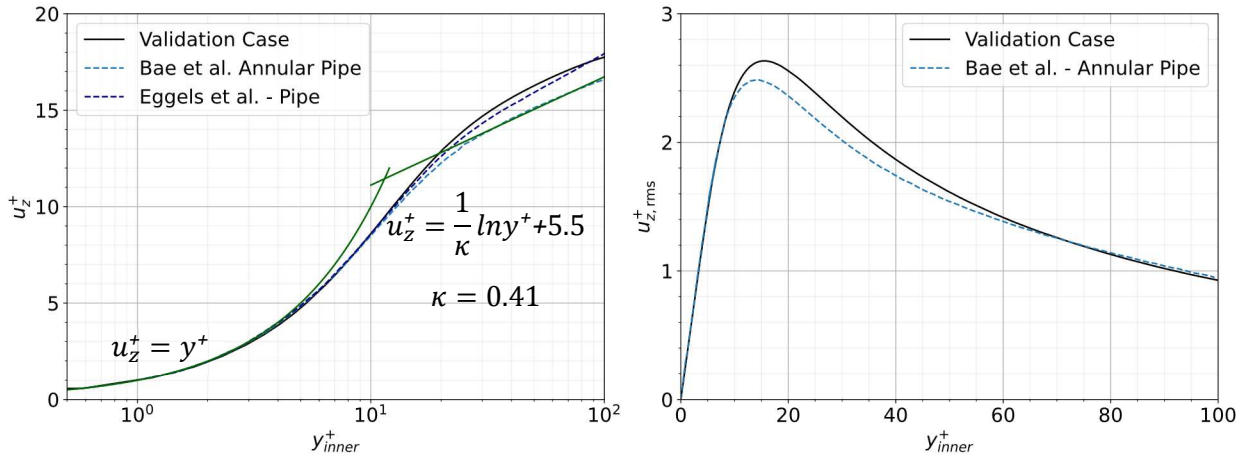

Figure 3.11. Dimensionless streamwise velocity profile (left) and RMS values of streamwise velocity component (right) by the dimensionless inner wall distance.

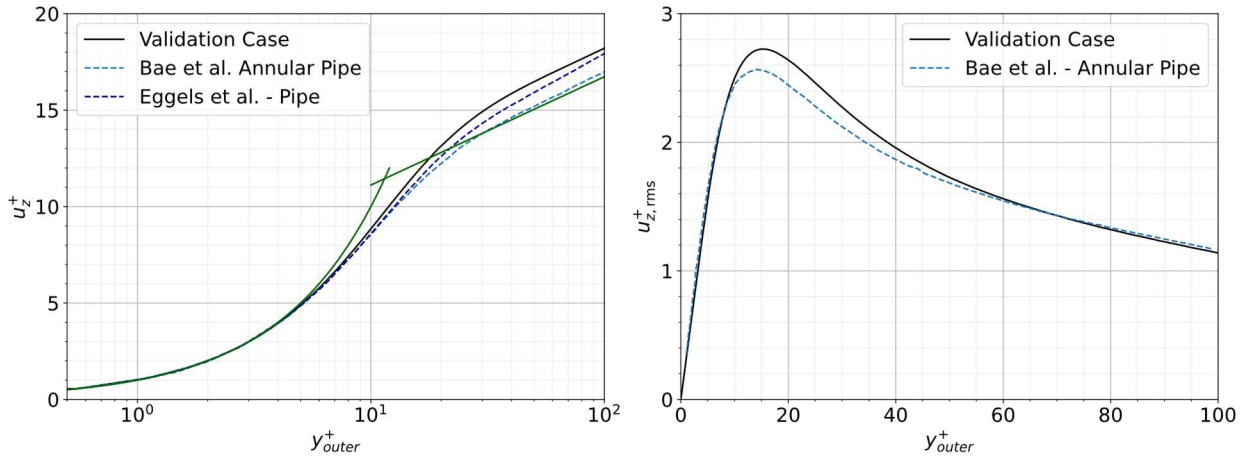

Figure 3.12. Dimensionless streamwise velocity profile (left) and RMS values of streamwise velocity component (right) by the dimensionless outer wall distance.

Dimensionless streamwise velocity showed a slight discrepancy after the buffer region through the bulk region through the references provided [20], [59] and it follows the law of the wall very well. The discrepancy was more visible in the RMS value of streamwise velocity, but it was limited to the vicinity of the buffer region as seen in Figures 3.11-12. Near wall regions were reproduced with excellent agreement. Overall agreement confirms the suitability of the numerical setup for the subsequent DNS cases.

4 Turbulence and heat transfer under supercritical pressure conditions

In this chapter, obtained statistics of the cases introduced in Table 3.6 are presented in this chapter, focusing on the flow events induced by heating within the heated, turbulent flows under supercritical pressure conditions. Chapter is structured to introduce the overview of the flow field stating how data sampling is done, characteristic scales of turbulence and general picture of the flow field structured with the fundamental flow data consists of mean velocity and temperature fields. In further sections, momentum and turbulent heat transfer statistics are presented and linked with the observed changes in the heated part of the flow field within the basis statistics obtained from inflow part. The effect of the conjugate heat transfer investigated in the scope of temperature statistics obtained where different behavior thermal statistics across cases were observed.

4.1 Overview of the flow field

Results are reported with cartesian coordinates as they were produced. Wall normal directions and angular directions are stated for each sampled data. For the heated part, data were collected in eight different angular positions, three of these positions ($0^{\circ}, 90^{\circ}, 270^{\circ}$) were used in the evaluation of the results. Sampling sets were repeated at every 4 hydraulic diameters (Fig 4.1) into the heated part to observe the developments of flow events occurred.

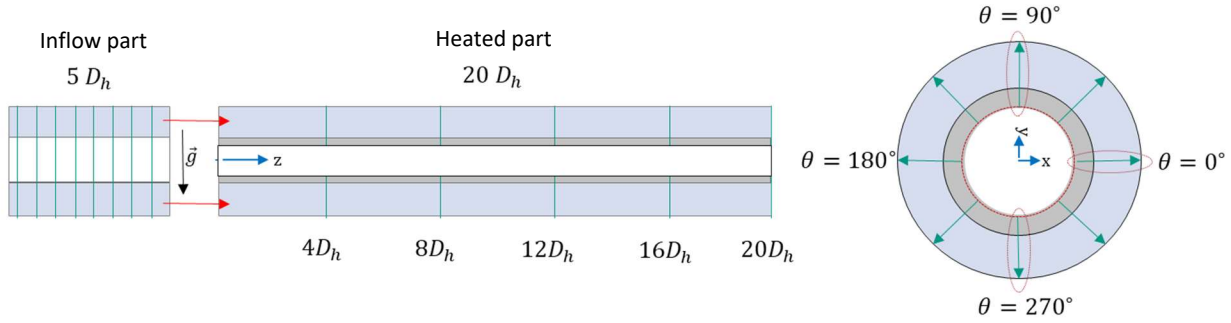

Figure 4.1. Representation of sampling locations used for the reported results.

The sampled data were classified into three groups based on their statistical degree. Fundamental data consists of time averaged velocity and temperature statistics used to understand the general

behavior of the heated flow. Reynolds stresses, turbulent anisotropy and turbulent heat flux, also known as “two-point correlations” were investigated through findings obtained from the analysis of fundamental data. These findings put into further investigation by obtaining triple point correlations as the transport budgets of turbulent kinetic energy and turbulent heat flux. Results presented are evaluated through comparative analysis in the context of the effects of heat flux and presence of the gravity.

4.1.1 The inflow part

The investigation of the flow events of the heated part was held within the turbulent statistics obtained for the inflow part to be able to separate different physical phenomena’s present in the heated part. The selection of inflow part as a basis for the comparison is made through the fact that inflow part was isolated from any heating effects, which serves as an upstream source for the heated part. The statistics include Reynolds-averaged mean velocity profiles, Reynolds stress components, and transport budgets of turbulent kinetic energy (TKE) to characterize the fully developed turbulent flow field in the annular pipe flow without any heating induced effects.

Results are normalized (if necessary) by the statistics provided in Table 4.1. Turbulent statistics of the inflow part include time-averaged values of velocity, principal components of the turbulent stresses, and budgets of TKE.

Table 4.1. Characteristics scales and statistics of turbulence for the inflow part.

	Inner wall	Outer wall
$\delta\ (r_h/2)\ (m)$	0.0011525	
$U_0(m/s)$	0.1350	
$\tau_{ft}(s)\ (heated)$	0.68	
$\tau_{avg}(s)\ (heated)$	$35\tau_{ft}$	
Re_0	5400	
$\tau_w(N/m^2)$	0.03984	0.03600
$u_\tau(m/s)$	0.008680	0.008252
Re_τ	173.6	165.0

The statistical information used to collect averaged results for the DNS simulations and turbulent scales data for the normalization process has been given in the Table 4.1. The term δ denotes half of the annular gap r_h that is used to normalize the wall distance. U_0 is the bulk velocity and Re_0 is the bulk Reynolds number in the inflow part. U_0 is used to normalize the velocity profile. The wall shear stress τ_w is used to calculate friction velocity u_τ which is a measure the velocity scale of the near wall turbulence. The friction Reynolds number Re_τ is used to characterize near wall turbulence in wall bounded turbulent flows. The averaging procedure was performed for τ_{avg} physical time that corresponds to 35 flow-through times τ_{ft} of the flow in the heated part. Inflow part statistics were plotted within the help of the statistics given in Table 4.1. to provide a reference for the changes in the heated part.

The streamwise mean velocity profiles against normalized wall normal distance shown as y/δ and y^+ were plotted in Fig. 4.2. In the left-hand plot, wall curvature and the narrow annular gap jointly shape the development of the velocity profile, where velocity profile at within the inner wall distance exhibit slightly greater development. However, the normalization by the friction velocity belongs to each wall reverses the situation as friction velocity slightly higher for the inner wall. This is due to the slight effect of the wall curvature on the turbulence where concave shape of the inner wall contributes slightly to the turbulence while convex shaped outer wall tends to stabilize it. The narrow annular gap leads to overlap of two boundary layers from the inner and outer walls in the core flow region where y^+>30. Overlapping of the boundary layers results in overshoot of the streamwise velocity profile at the core flow region in comparison to log law of the wall.

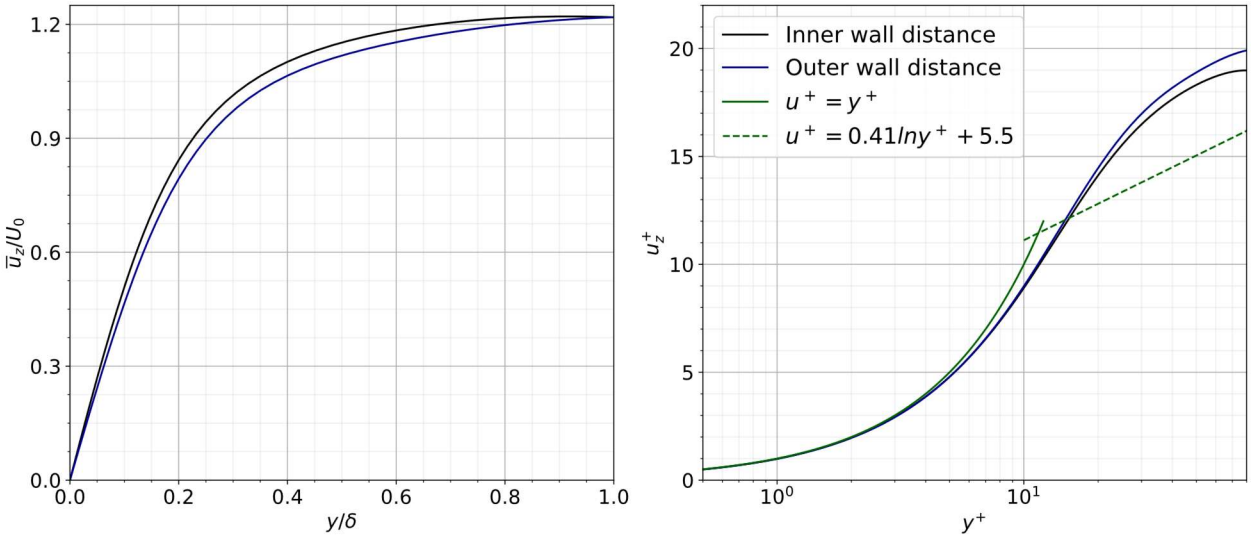

Figure 4.2. Streamwise mean velocity profile at inner and outer walls distances.

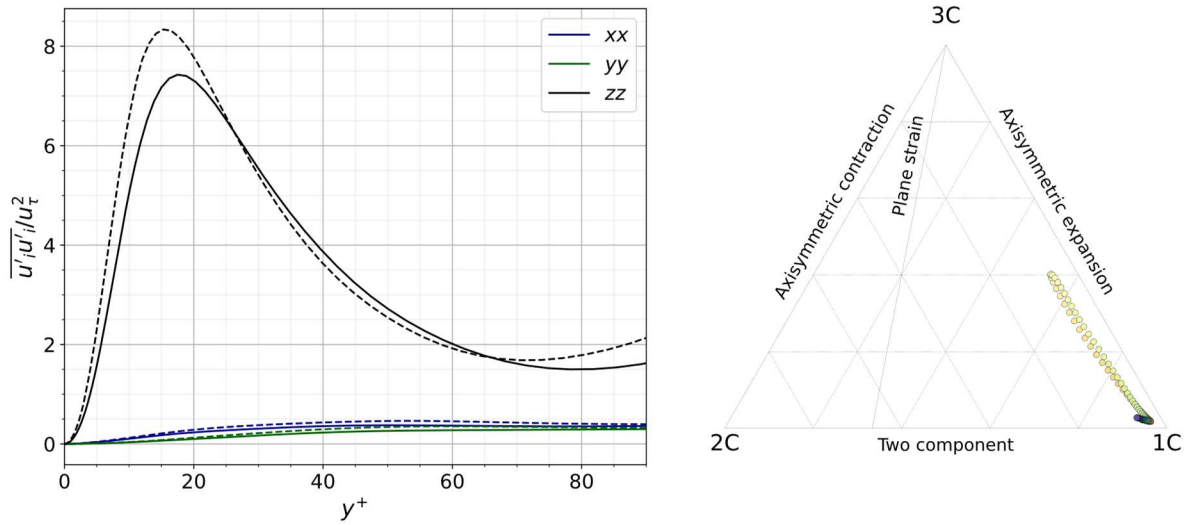

Figure 4.3. Principal Reynolds stresses with dimensionless inner (solid) and outer (dashed) wall distances and representation of turbulent anisotropy for the inflow part.

Principal turbulent stresses the fully developed turbulent flow field are given in the Figure 4.3 left-hand side. It is observed that the streamwise term is highly dominant relative to the other terms. The polarized behavior observed here is due to narrow flow area which causes suppression (or

attenuation) of velocity fluctuations in the wall–normal and angular directions. In other terms, turbulent momentum transport in radial and angular directions are being suppressed. Consequently, flow shows the attributes of highly anisotropic flow. The barycentric map (right) is plotted to visualize the state of turbulent anisotropy in the inflow part. The map identifies highly anisotropic attributes of annular pipe flows [82]. The state of anisotropy forms a cluster near to the 1C state corner, with a weak attempt towards isotropy at the core flow region.

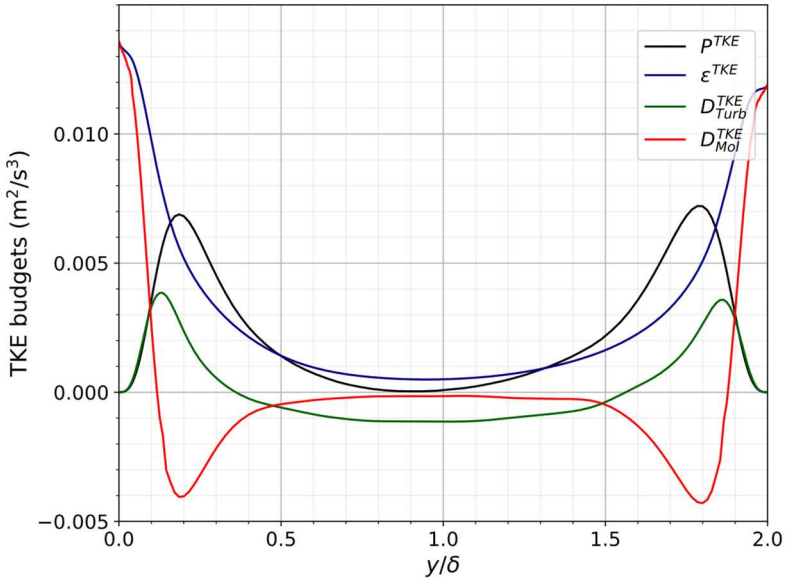

Figure 4.4. Turbulent kinetic energy transport budget profiles for the inflow part.

The development of the provided turbulent statistics above is linked to the transport mechanisms that support them. Budget term profiles for the transport of turbulent kinetic energy plotted in Fig. 4.4 for the inflow part. These mechanisms contribute either positively or negatively to the transport balance. Physics behind these contributions are connected to the flow events due to external effects to the flow. The physical meaning of this budget terms are explained in the section 4.2.

The budgets distributed on the inflow part resemble the state of the wall-bounded flows [11]. Dissipation, and molecular (viscous) diffusion peak in the near-wall regions and decrease rapidly through the viscous sublayer, whereas production and turbulent diffusion terms develop (and peak afterwards). All budgets stabilize at the core flow region. Results provided for the inflow part serve as a basis for comparison to describe the changes induced by heating and buoyancy-related effects. The turbulent statistics, including fundamental data and two- and three-point correlations, to be presented have been scaled through statistics obtained from the inflow section. Case 2 is used as a base case for the evaluation of the results.

4.1.2 The heated part

In this section, the overview of heated part is introduced within the comparative analysis on the effect of the heat flux applied. For this purpose, cases 2 (645-050-G) ($q''_w = 50\ kW/m^2$) and 3 (645-100-G) ($q''_w = 100\ kW/m^2$) were comprehensively analyzed by DNS statistics. The

fundamental statistics were also supported by the results from case 1 (640-050-G) and case 5 (650-050-G). Results are examined at three selected streamwise locations as $4D_h$, $12D_h$ and $20D_h$ to distinguish acting effects on the flow field. The aim is to assess how overall flow behavior changes with the increased heat flux value. Analysis was structured based on the case 2 DNS statistics.

Results obtained from fundamental DNS data are presented in this subsection. The content includes profiles of velocity, temperature, as well as relevant bulk flow data. The sampling location is indicated by the arrow on the mini-map of flow cross section. The axis y/δ refers to wall normal distance from the inner wall to outer wall in the sampled location. According to the mean streamwise velocity profile shown in Fig. 4.5, the flow is subject to different course of heating effects at different angular directions. The increase in wall heat flux contributed differently to the flow field for each angular direction. At the top ($\theta = 90^{\circ}$), streamwise flow drew back and formed a separate layer in the flow as further development of development velocity profile stagnates. This can be recognized in Fig. 4.5 as velocity profiles temporarily flattens. This effect is stronger when a higher heat flux has applied.

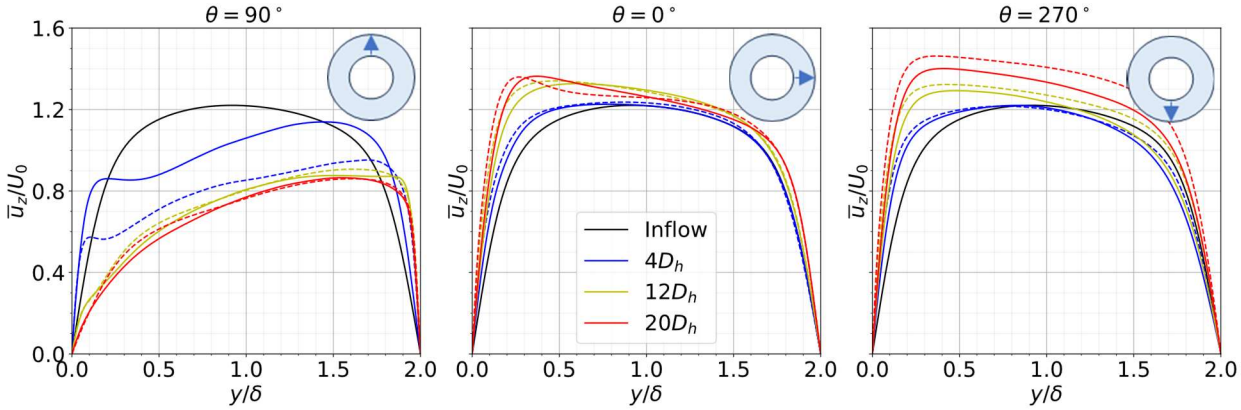

Figure 4.5. Changes in the mean streamwise velocity profiles in the heated part for cases 2 “645-050-G” (solid line) and 3 “645-100-G” (dashed line).

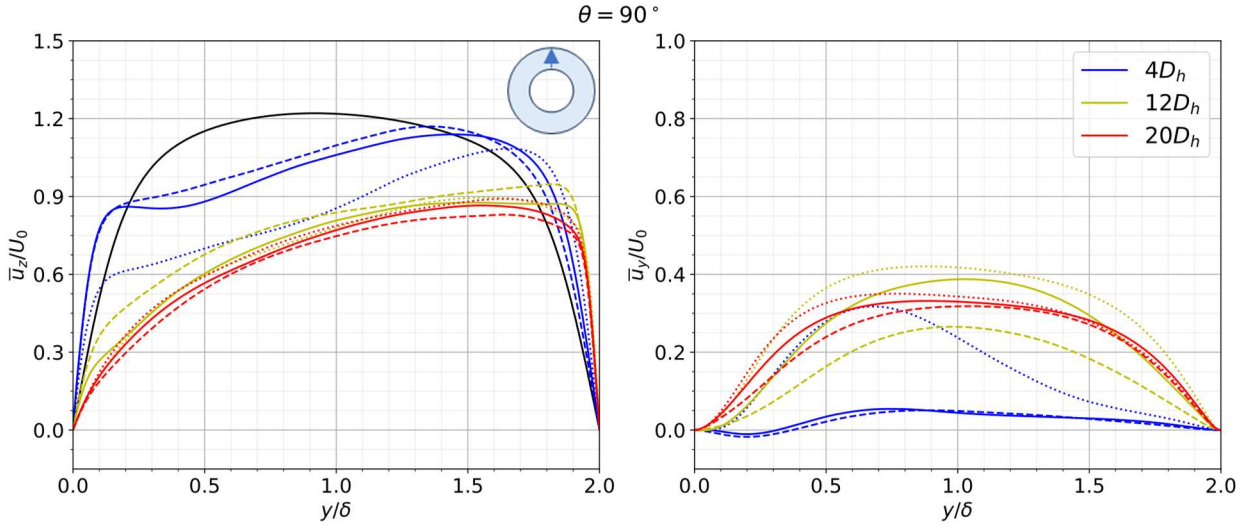

Figure 4.6. Changes in the mean streamwise and wall normal direction velocity profiles in the heated part for cases 1 “640-050-G” (dashed line), 2 “645-050-G” (solid line), and 5 “650-050-G” (dotted line).

On the other hand, the magnitude of the near-wall reduction in the streamwise velocity was not determined by heat flux alone. As the inlet temperature changes for the same heat flux applied, the observed level of reduction at the same location also changes since the thermal development of the flow affected at the entry of the heated part. In Figure 4.6, Case 5 (650-050-G) exhibited a similar trend in streamwise velocity at the top region compared to case 3. In detail, case 3 exhibited a slightly sharper rise and more layer like stagnation in the near wall streamwise velocity profile development. Thus, increased heating intensifies thermal stratification, but the cause of the thermal stratification is not only dependent on heat flux but "heating effects" that covers all thermally induced contributions in addition to heat flux strength which observed upon velocity profile in Figures 4.5 and 4.6. Further remarks were made in following sections on this point.

Heating effects significantly altered the mean velocity profile throughout the heated part of the annular pipe. On the side region ($\theta = 0^{\circ}$), (center, Fig. 4.5) the streamwise velocity has increased as flow progress that shows clear evidence on flow has accelerated on its path. The thermal acceleration of the heated fluid is more apparent in the near-wall region as the profile departs from the general trend. This was caused by several effects, such as buoyancy movement of fluid to upper regions, decreased friction due to decreased viscosity and thermal expansion by density of the heated fluid. Further information is needed to distinguish their presence and relative contributions of these phenomena, which has been revisited in further pages. Increased heat flux caused slightly sharper peak velocity development in the near-heated wall region, indicating that flow events in case 2 are amplified. A similar behavior has been observed at the bottom region ($\theta = 270^{\circ}$), where streamwise velocity drew flatter profile instead of local peak. Difference in the development suggests that localized growing peak at the near heated wall due to the effect of buoyancy as heated fluid travels upper regions. The difference can be observed in Fig. 4.7 within the case 4 as gravity is removed from the system.

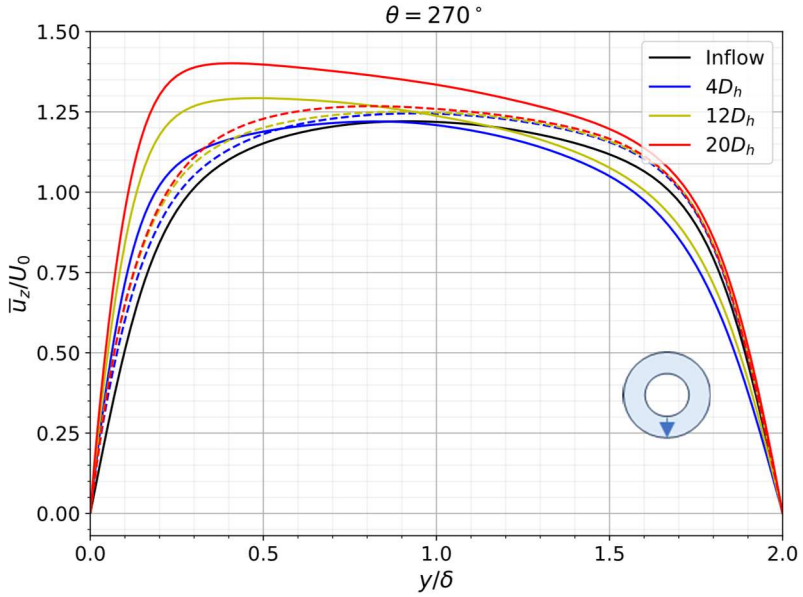

Figure 4.7. Changes in the streamwise mean velocity profiles in the heated part for cases 2 "645-050-G" (solid line) and 4 "645-050-N" (dashed line).

Absence of the gravity also removed effects that contributing mixed convection. For this reason, the bottom side of the case 2 was selected for comparison as the region least affected by secondary flow. It that case, the flow domain exhibited the behavior of forced convection regime for annular pipe flow heated from the inner wall. Streamwise velocity profile subjected to limited and almost symmetrical development and since buoyancy induced movement part of the secondary flow was no longer present. It was observed that presence of buoyancy was contributing to the thermal acceleration of the flow. The limited development allows to distinguish the buoyancy contribution to the thermal acceleration by directional transfer of momentum from the reduced shear and thermal expansion of the fluid.

Cross flow distorted the streamwise movement of the fluid particles that created slight suppression in that direction. The heated fluid accelerates throughout the annular pipe flow depth due to reduced shear, and the thermal expansion gradually enhances the acceleration event gradually in a decreasing magnitude away from the heated wall. Therefore, the heating effects were amplified with increased heat flux.

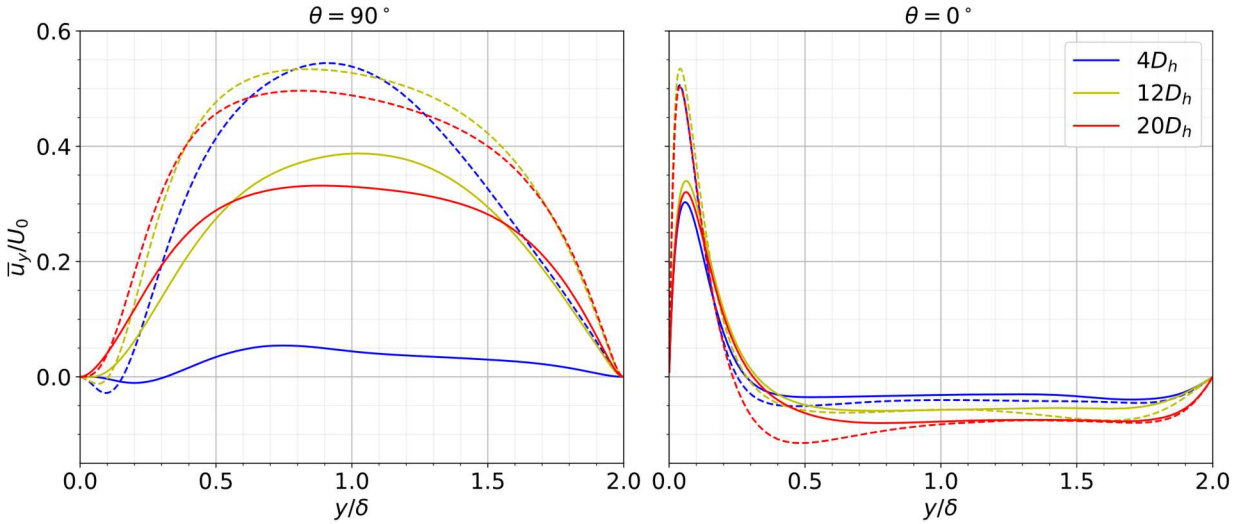

Figure 4.8. Y direction mean velocity profiles for angular positions for the heated part for cases 2 "645-050-G" (solid line) and 3 "645-100-G" (dashed line).

In Fig. 4.8, profiles of the y direction component of the velocity were plotted for the top and side region. As the buoyancy effect was the result of the heated (lighter) fluid traveling upwards against the gravity, a higher heat flux triggered greater upward motion of fluid. Fluid movement in the y-direction at the top was far more intense for case 3 than case 2, even at the early stages. The changes explain how fluid momentum is redistributed under by buoyancy. The redistribution of momentum has led to flow re-development starting from the early stages. Case 2 posed a gradually evolving picture in this regard. However, higher heat flux resulted in a burst of buoyancy effect at the early stage for case 3. Immediate and strong response of buoyancy has driven the flow re-development to advance from overshooting to stabilization phases. An early negative wall-normal motion in the vicinity of the heated wall at the top region that amplifies with the heat flux. Immediate occurrence of buoyant movement created vortical structures in this region where flow tries to compensate for immediate y-directional movement. These events were sourced by the upwards motion of the heated fluid by the curvature of the inner wall. Buoyant movement of the fluid in the vicinity of the inner wall can be traced at the side region as indicated by the peak shown

in the plot in Fig. 4.8 (right). Negative y-direction movement was also observed, indicating a possible redistribution of the heated fluid back to lower regions. These movements are part of the secondary flow, which acts differently from the main flow. X-direction movement at the side region (Fig. 4.9) confirmed the secondary flow movement that follows the curvature of the inner wall leading to upward motion and free redistribution afterwards.

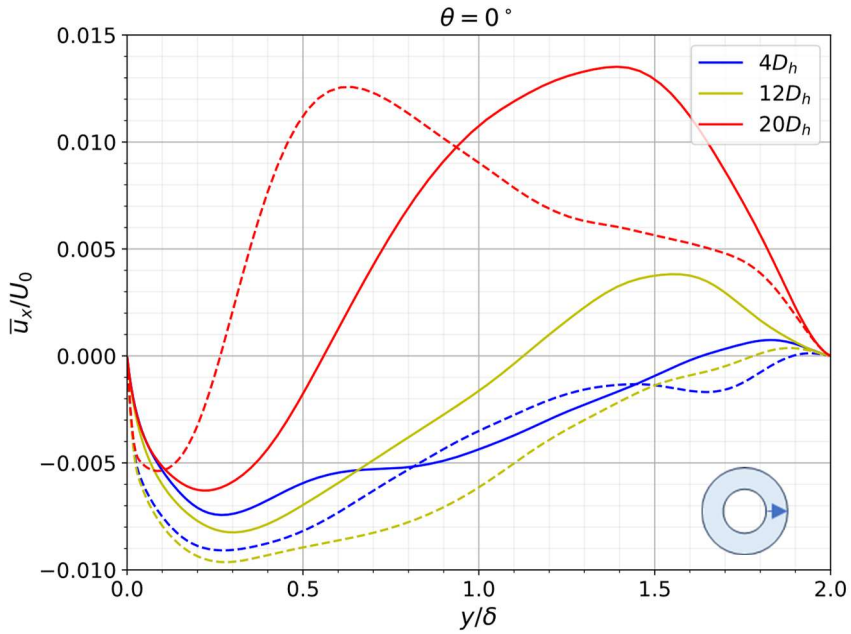

Figure 4.9. The mean x direction velocity profiles for angular positions for the heated part for cases 645-050-G (solid line) and 645-100-G (dashed line).

The secondary flow motion indicates that the near-wall reduction in streamwise velocity is related to buoyant movement of the fluid. The determination of the intensity of secondary flow is essential to observe the whole picture in the flow domain. Therefore, secondary flow intensity (SFI) [63] was mapped for the flow cross sections at the plot locations provided. SFI is the square root of the sum of the squared non-streamwise velocity components (radial and angular) normalized by the bulk velocity of the inflow part. The contribution by thermal acceleration of the fluid is neglected due to the purpose of the SFI investigation is to distinguish and assess the cross-flow sourced part of the secondary flow. Therefore, SFI given in Eq. 4.1.

$$SFI = \frac{\sqrt{\overline{U}_x^2 + \overline{U}_y^2}}{U_0} \tag{4.1}$$

SFI values were calculated for the cross-section of the annular pipe and are presented in Figures 4.10 (Case 2) and 4.11 (Case 3). SFI maps confirmed the inferred travel path of the secondary flow. High SFI started to appear along the inner wall surface, starting from the bottom regions of the flow domain and formed a thickening layer on the path through the top region. The heated fluid from both sides collided at the top region and created symmetric vortical structures. Profiles of the velocity components on the merging location at the top region were presented at the previous

figures. Merged secondary flow structures redistributed back to other regions by the curvature of the outer wall. Case 3 formed a thicker layer of high SFI and exhibited stronger mixing in this regard due to higher heat flux applied. Despite stronger mixing, buoyancy effect remained the driving mechanism for the secondary flow. These movements are the result of heating effects provided by the heat flux applied to the inner wall.

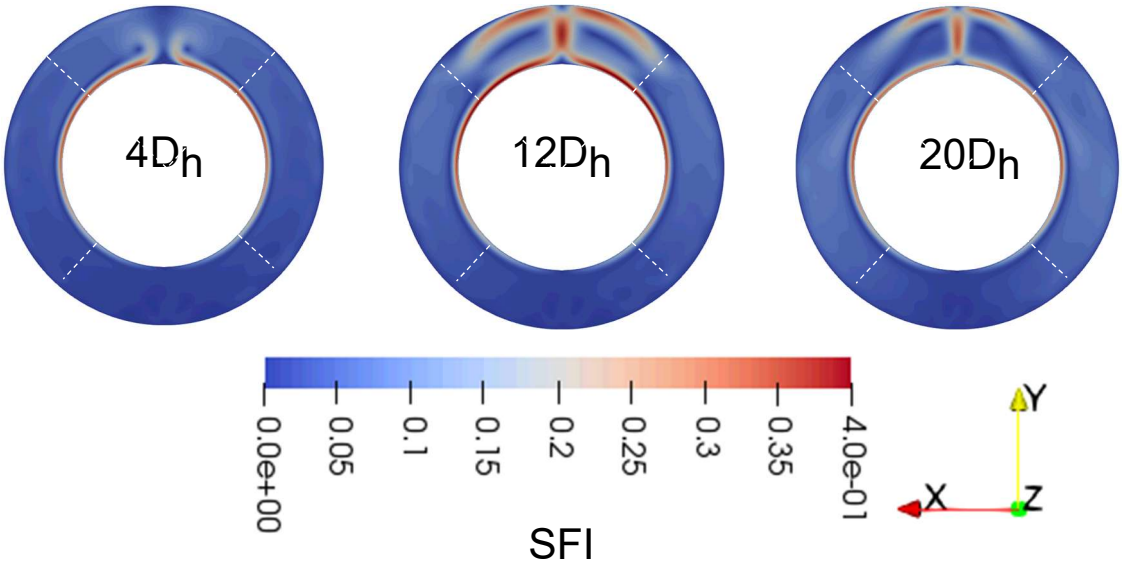

Figure 4.10. Annular pipe flow cross section of contour plots of SFI for case 2 (645-050-G).

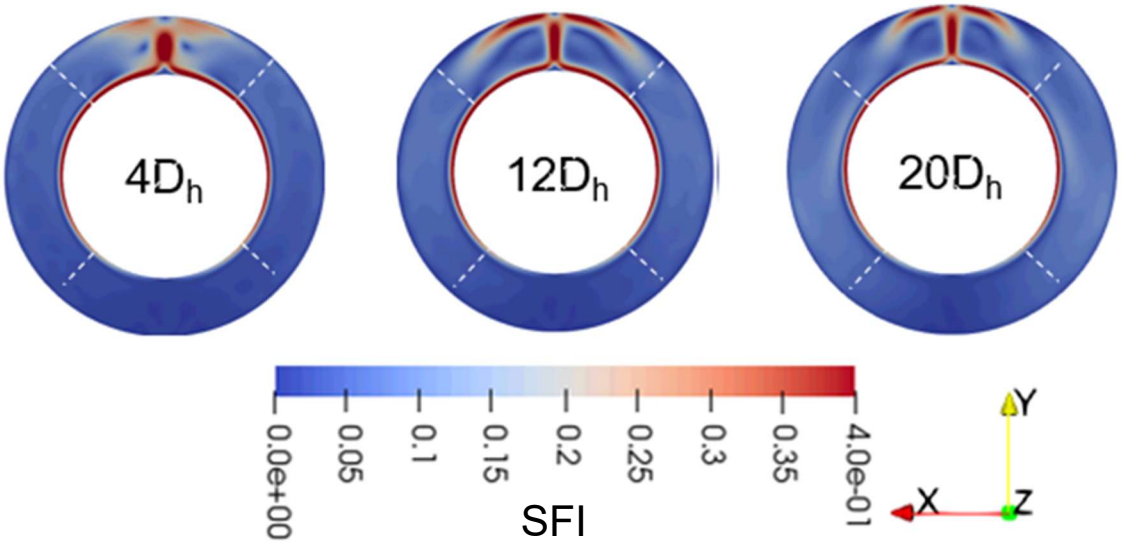

Figure 4.11. Annular pipe flow cross-section of contour plots of SFI for case 3 (645-100-G).

The flow re-development started with emergence of secondary flow by buoyancy effects and strong thermophysical property changes until the stabilization phase at the end of the heated part

driven by the heated, lighter fluid travelling can also be traced through mean temperature profiles in Fig 4.12.

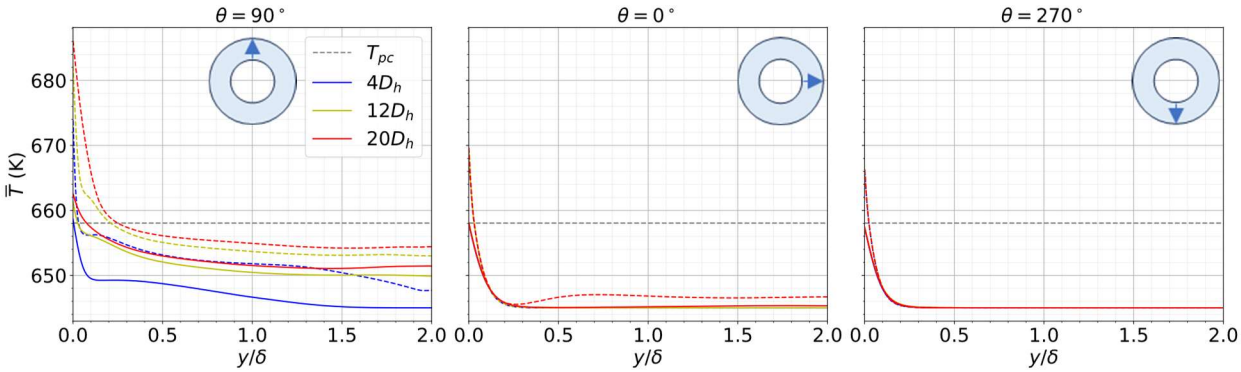

Figure 4.12. Changes in the mean temperature profile in the hated part for cases 2 “645-050-G” (solid line) and 3 “645-100-G” (dashed line).

The radial temperature profile at the top region of the annular pipe has risen gradually along with the formation of the stratified layer which is seen in Fig. 4.12 (left) as limited plateau formation appears at the early stages. In this area, the temperature gradient dropped to near zero after a rapid fall over a short distance from the heated wall. The formation dissipates within the progress of heated flow. The situation aligns with the stratified layer formation observed in the streamwise velocity profiles. The intensity of the formation increased with higher heat flux as well. The top region wall temperature reached 662.5 K for case 2 and 683.1 K for case 3. However, the monotonic fall of temperature was not disturbed in the other regions, where the profile drew a very steep fall near the heated wall and remained almost constant. The wall temperature was still higher for case 3; yet the temperature dropped to almost the same levels as case 2 at the core flow region. The only visible difference was in the side region, where temperature levels are elevated slightly at core flow region. Even though uniform heat flux was defined as a heat source, temperature development was not uniform between regions due to buoyant effects.

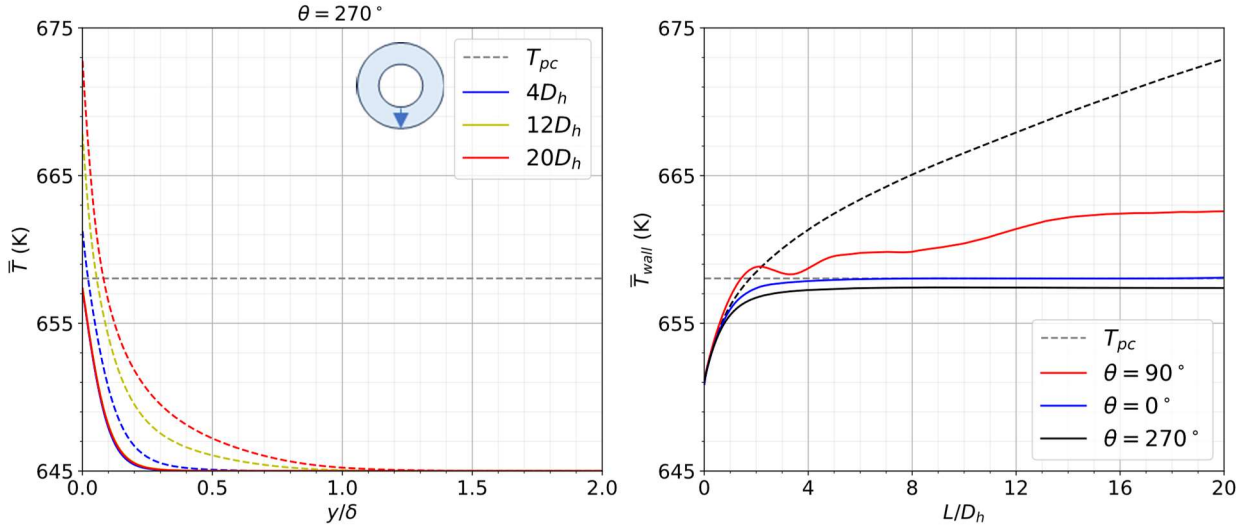

Figure 4.13. Changes in the mean temperature profiles for annular gap and inner wall in the heated part for cases 2 “645-050-G” (solid line) and 4 “645-050-N” (dashed line).

In Fig. 4.13, The temperature profile development for case 4 was shown. Temperature profiles grown symmetrically across flow cross section unlike case 2 as buoyancy effects removed. As heated fluid did not depart from the wall surface, temperature profile growth extended to the core flow as flow progresses. The wall temperature developed continuously in the case 4.

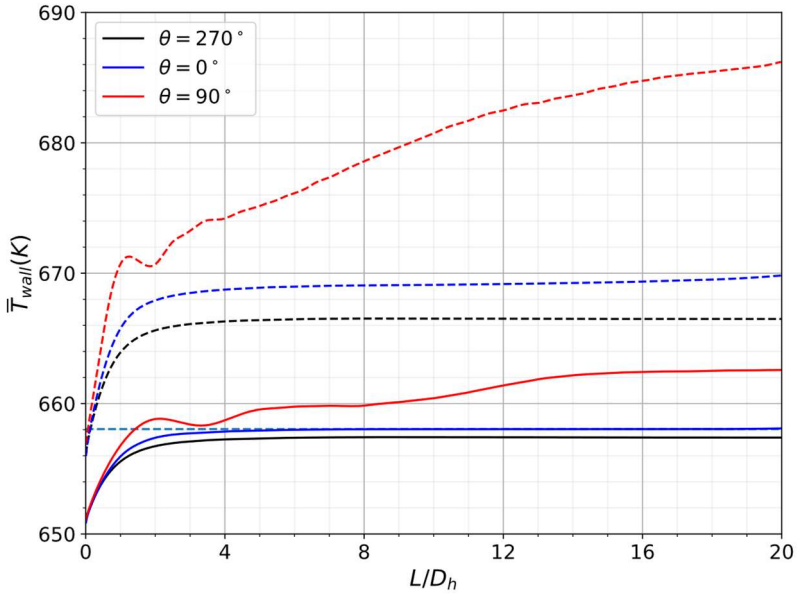

Figure 4.14. The mean wall temperature profile in the heated part for cases 2 “645-050-G” (solid line) and 3 “645-100-G” (dashed line).

In case 2, accumulation of heated fluid at the top region was reflected to the wall temperature development shown in Figure 4.14. The increase in the heat flux accelerated this development as initial rise concludes at the earlier location. Initial rise of the mean wall temperature noted as 6 K (case 2) and 12 K (case 3). It rose rapidly until it reached the local maximum point after crossing the critical temperature. However, the rapid rise was limited to the early stages, which dropped back to its local minimum point before it continued to increase. The initial oscillation after the rapid rise of the wall temperature was apparent at the entry stage for both cases. The range of the behavior in flow direction was shorter for the higher heat flux since case 3 wall temperature profile continued its rise after small oscillation. In further locations, mean wall temperature profile continued to rise with variable trend through the end of the annular pipe.

In Figure 4.15, the change in inlet temperature resulted in a shifted the development of the wall temperature profile in both elevation magnitude and axial location. The oscillating behavior also appeared in cases 1 and 5. Meaning that local changes at the early stage of the wall temperature do not necessarily cross the critical temperature to observe this behavior as case 1 experienced these oscillations inside colder side of the pseudo-critical region. The observed effect was the product of both entry effects and strong thermophysical property changes driven by heat input. The axial range of the oscillations were shortened as initial temperature rise but still persisted. The similarity noted in between case 5 and case 3 is visible in the wall temperature with certain characteristic difference as case 3 mean wall temperature profile was shifted upwards with its higher heat flux.

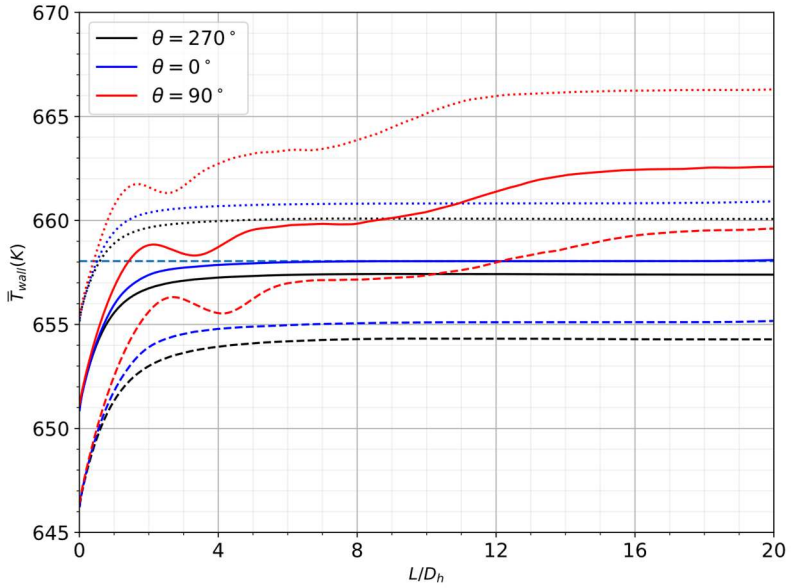

Figure 4.15. The mean wall temperature profile in the heated part for cases 1 “640-050-G” (dashed line), 2 “645-050-G” (solid line), and 3 “650-050-G” (dotted line).

Additionally, it should be noted that the changes observed in the comparison of cases with different inlet temperatures do not exactly show different stages of early flow re-development. There was a visible trend changes observed in the development of temperature profile due to the extent of the pseudo-critical region experienced. This analysis confirmed that the stronger drawback due to stratified layer is not only sourced by the heat flux strength but also the result of heating effects altogether. The observed changes in the formation of the stratified layer of the fluid highly dependent on the heat flux strength with small aid of the inlet temperature only at the entry phases of the heated channel where flow is in re-development phase due to entry effects.

These local trend changes indicate the traces of the local changes in heat transfer quality. Fig. 4.16 shows plots of the streamwise development of the bulk values of Reynolds number (left), Nusselt number (middle), and Richardson number (right) to understand the general behavior of the flow domain for cases 2 and 3. The rise in bulk Reynolds number indicates the effect of thermal acceleration of the flow in place at the global level. As the fluid is heated, viscosity and density of the fluid decrease drastically within the pseudo-critical region. The mass flux of the flow remains constant which leads to increase in the streamwise velocity at the bulk flow. Meaning that observed decrease in the velocity at the top region at Fig. 4.5 remains locally effective against total flow cross section which is compensated by the other regions. Thermal acceleration was found to be amplified by the heat flux strength throughout the heated part. The Nusselt number experiences a rapid fall as a counterpart to the rapid rise in wall temperature, as heat transfer suffers from the entry effects the heated annular pipe.

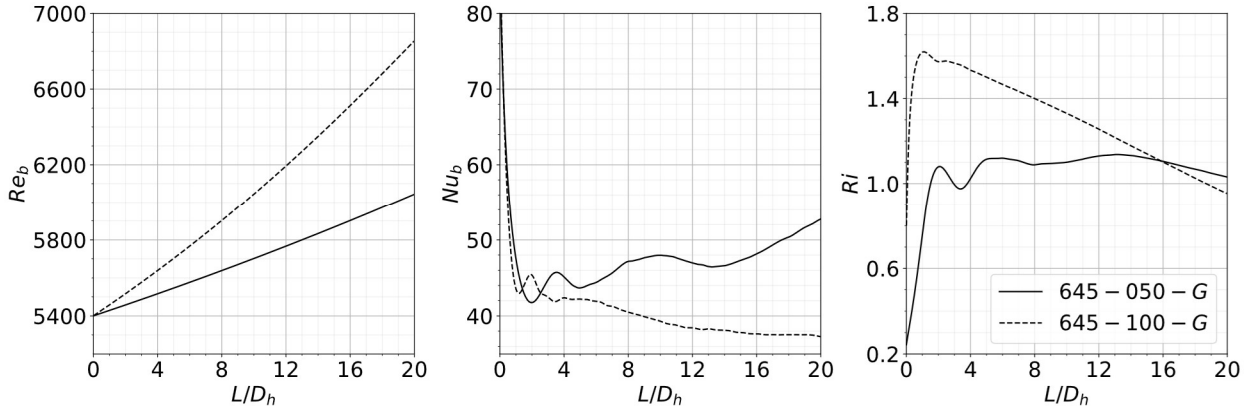

Figure 4.16. Profiles for bulk Re, Nu, and Ri numbers along the heated part for cases 2 "645-050-G" (solid line) and 3 "645-100-G" (dashed line).

The quantities shown in Fig. 4.16 calculated within bulk flow properties by considering bulk temperature across heated part within the equations provided in chapter 2. The oscillating behavior observed in the plots middle and right was due to response of the mean inner wall temperature profile in the top region of the annular pipe. Although the plot shows bulk data, the contribution of the other regions was small enough to be dominated by the top region. In the case of horizontal and buoyant flows, it could not be expected that each region would exhibit the same behavior in terms of heat transfer since temperature elevation around circumference of inner wall was different. The heated fluid is being transferred to the upper regions and will not sustain uniform heat build-up unlike vertical flows. Therefore, oscillations observed reflect the buoyancy effects associated with cross flow part of the secondary flow. The Richardson number, or buoyancy relevance of the flow, peaks with the elevated wall temperature of the top region and returns to stabilization trend in further stages. As stated before, increased heat flux on case 3 enhances the streamwise thermal acceleration of the flow. However, the Nusselt number did not recover in case 3, showing that heat transfer worsens as the flow progresses. Both cases validate the buoyancy criterion of Richardson number $(0.1 < Ri < 10)$ with values between 0.95 and 1.6. These values indicate that both cases were in mixed convection regime where buoyancy effects are considerable. In this context, cases can be considered as "weakly buoyancy relevant". Additionally, the Richardson number in case 3 exhibits a monotonic decline in the streamwise direction, despite the increasing inertia of buoyancy effects being experienced. Thermal acceleration was strong enough to alter the significance of enhanced buoyancy in comparison to case 2. It was expected that increased heat flux would result in more buoyant movement due to increased rate of change in thermophysical properties due to steeper temperature gradients. On the other hand, the initial peak of the (burst) of the buoyancy effect dissipated in the early stages and heated fluid with decreased density and viscosity started to escape in the streamwise direction rather than gravitational direction. Therefore, the effect of the heat flux on the buoyancy cannot be simplified with the proportionality of the single effects where such complex behavior exists.

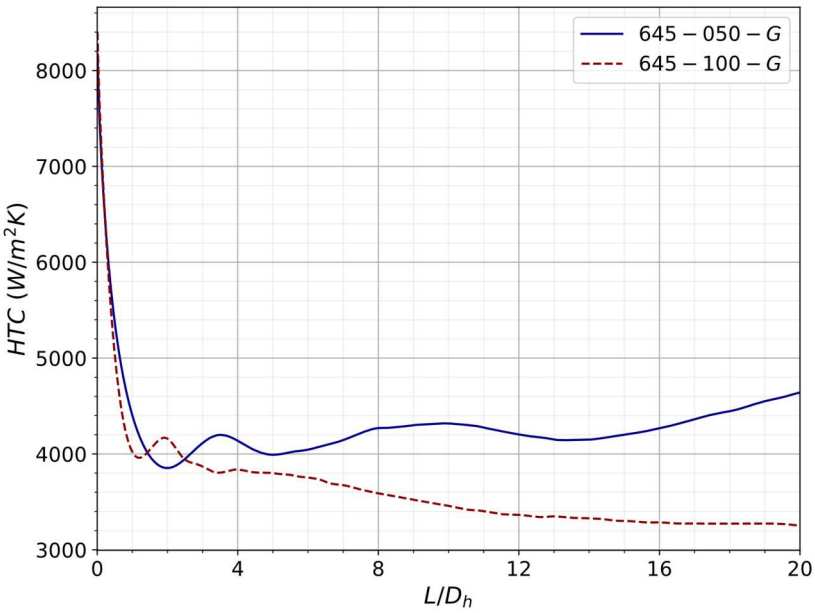

Figure 4.17. Comparison of heat transfer coefficients (HTC) for the heated part for cases 2 "645-050-G" (solid line) and 3 "645-100-G" (dashed line).

HTC profiles plotted for cases 2 and 3 along the heated part in Fig 4.17 to provide additional insight into heat transfer quality, alongside the Nusselt number. The local minima and maxima points noted for Nu were also valid for the HTC profiles. The observed fall in the HTC is very small compared to experimental studies [37], where the boundary conditions, as well as the wall temperature rise, are too large to be comparable. The heat transfer quality was still subject to changes, as it decreased rapidly due to entry effects and then recovered until the middle stages of the annular pipe. The recovery of HTC in the case 2 contains several local minimum and maximum points where overall trend was favoring recovery through further stages. On the contrary, the heat transfer quality in case 3 continuously diminished until the late stages of the annular pipe that supports the findings reported on the evaluation of the Richardson number discussed upon Fig. 4.16. The strong influence of buoyancy on the secondary flow initially induces the cross flow and mixing where flow re-development begins. The initial effects of the secondary flow increase the mixing at the early stages. However, the drastic drop of viscosity and density leads to increase in the streamwise velocity and diminishing turbulent activity at the near wall simultaneously. Therefore, a local laminarization event takes place and becomes part of the flow re-development process. Meantime, the heat transfer quality worsens on the case 3 as heated fluid cannot be carried further away from the wall efficiently due to decreased turbulent activity associated with the laminarization.

The DNS cases were investigated to provide an overview of the flow behavior in terms of buoyancy effects, thermal acceleration, and flow re-development and laminarization. These mechanisms are evaluated on a region-wise basis to understand how they operate across the annular pipe flow in provided boundary conditions. A detailed investigation is presented in following sections where obtained statistics regarding momentum transfer and turbulent heat flux are introduced. These statistics include two-point correlations, such as Reynolds stresses,

turbulence anisotropy, and turbulent heat flux and transport budgets of the turbulent kinetic energy and turbulent heat flux, respectively.

4.1.3 Summary

In the first section, the overview of the flow field was investigated within the fundamental data obtained from DNS results. These data consisted of the mean profiles of velocity and temperature. Five different cases were performed for these investigations to analyze overview picture on turbulence and heat transfer under supercritical pressure conditions for horizontal annular pipe. The main focus was given to effect of heat flux strength and presence of gravity to be able to separate secondary flow events and investigate their effect on the flow field. As flow entered heated part, redevelopment began and required more than half of the heated part to restabilize. The secondary flow appeared with the buoyant movement of the fluid due to heating which caused three characteristic angular regions simultaneously in its flow cross section. These regions referred as bottom, side, and top regions which are separated mainly by the intensity of the secondary flow. The initial rise of the fluid particles formed a stratified layer in the near heated wall region that affected both mean velocity and temperature statistics locally. Layer itself appeared to be connected to the buoyant movement of the heated fluid was visible in all regions. The intensity of the secondary flow was measured by SFI, which has increased by the heat flux. The strongest formations were observed in the top region where streamwise velocity has fallen to 80% (case 2) and 50% (case 3) of the bulk velocity of the inflow part at the near wall region. The path of the secondary flow did not only cover the top region; it was redistributed back to other regions by the curvature of the outer wall. Therefore, traces of enhanced mixing by secondary flow were visible in the side regions as well. The bottom region was the least affected one by the changes mentioned above. Heating effects could not extend beyond the near heated wall region since heated fluid was immediately removed by buoyancy. These regions also differed in terms of the wall temperature profile. The effective heat removal by buoyancy led to heat accumulation at the top region which resulted in steady wall temperature profiles in other regions across heated part. The cases investigated were checked to see whether the buoyancy criterion set for Richardson number (Ri) [32] was achieved. It was found that both cases were stationed at the lower edge of the onset of the buoyancy criterion where they were considered as “weak-buoyancy relevant”.

Side regions were affected by the secondary flow as heated fluid initially traveled by the curvature of the inner wall to merge in the top region and was redistributed back later by outer wall curvature. Layer formation was limited to the near wall region. The traces of enhanced mixing by heated fluid were observed in further locations of the heated part. The bottom region was the least affected region as heated fluid particles were immediately removed. However, thermal acceleration of the fluid was present around all regions of the flow cross-section due to reduced shear and expansion of fluid by temperature. These effects were amplified by increased heat flux which is physically relatable by only changing thermophysical properties of the heated fluid. Therefore, the term “effect of the heat flux” were not comprehensive enough to describe the cause of the changes in the heated flow. They were named as “heating effects” to describe complex mechanisms leading abovementioned changes. It was found that layer formation itself did not grow larger solely with higher heat flux, also it was a part of a flow development process observed in the case 5 that

stratified layer expanded its effective area in the during stabilization. However, the speed of the occurrence and the momentum in buoyant movement have increased by the increased heat flux.

These flow events also affected the quality of the overall heat transfer. In the early locations of the heated part, the Nusselt number had a steep fall due to entry effects for all cases. Later, case 2 entered a recovery state that persisted until the end of the heated part. This recovery had a variable rate due to evolution of the wall temperature. On the contrary, there was a continuous fall in the Nusselt number in case 3. It means that intensified and rapidly growing stratified layer led to decrease in the heat transfer quality even though thermal acceleration of the flow was significantly higher in comparison to case 2. The secondary flow intensity and as well as stratified layer in case 3 did not disperse fast enough to allow the recovery of heat transfer.

Abovementioned effects were effective under the presence of gravity. It was necessary to remove it to separate gravity connected effects and heating-only effects. It was found that decrease in the viscosity and density had a partial contribution on the thermal acceleration of the fluid. Thermal acceleration of the fluid was significantly weaker in comparison to other cases despite the greater development of the temperature received. It turned out that buoyancy movement also induced main flow direction part of the secondary flow.

4.2 Momentum statistics

Investigations made in this section mainly focused on the turbulence quantities in terms on Reynolds stresses and turbulent anisotropy. Later, these analyses were supported by the transport budgets of turbulent kinetic energy. Investigations are made to consider the effect of heat flux comparing two cases: case 2 (645-050-G) and case 3 (645-100-G) and presence of gravity by including case 4 (645-050-N). Other cases 1 (640-050-G) and 5 (650-050-G) were used to aid the analysis made. The investigation made under the context of buoyancy effect, laminarization, turbulent anisotropy and the transport of turbulent kinetic energy.

4.2.1 Buoyancy effect

In this subsection, Reynolds stresses (or fluctuating momentum components) on the cross-flow directions were used to investigate buoyancy effect on the heated annular pipe flow. Analysis made upon the emergence, and post effects on the flow field.

The y-direction component of Reynolds stress provides information on the buoyant movement of heated fluid particles. In Fig 4.18, the buoyant effect induced evolving flow re-development at the top region. The heated, lighter fluid travelled upward along the heated part in variable intensities. The intensity changes aligned with the SFI mapping in Fig. 4.11, which means that dominant response of the secondary flow was induced by the buoyancy effect. The late dispersion of the heated fluid by secondary flow was evident in the side region profiles, which exhibit two separate core locations. The first rise is due to buoyancy of the heated fluid in the near heated wall region.

The second one occurs within the return of the heated fluid by the curvature of the outer wall. Enhanced mixing by the secondary flow elevated y component stress profile in this region as secondary flow disperses to the lower regions.

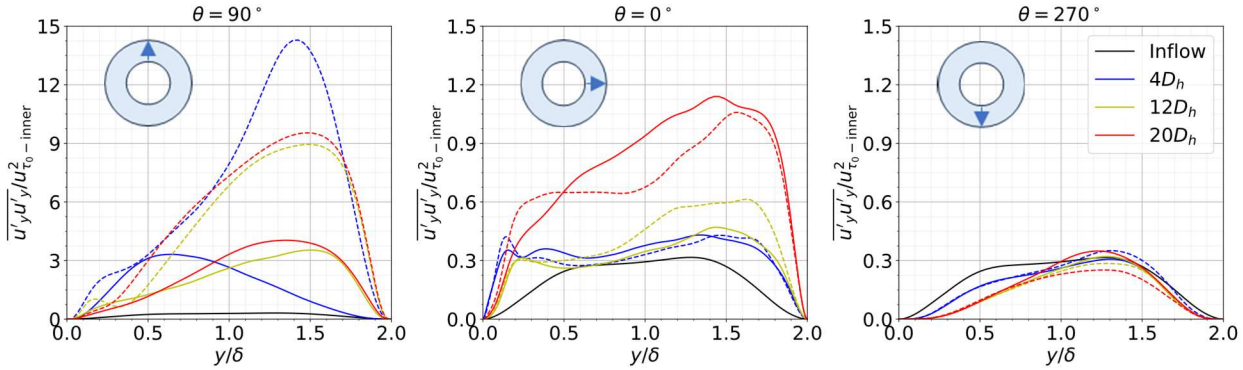

Figure 4.18. Comparison of y-direction Reynolds stress component profiles for three different angular positions along the heated part for cases 2 “645-050-G” (solid line) and 3 “645-100-G” (dashed line).

The bottom region was largely unaffected, as the heated fluid does not mix with the core flow; instead, it contributes to secondary flow by traveling upward. Increase in the heat flux resulted in the early overshoot of the top region y component stress (Fig. 4.18) which was entered stabilization trend starting from the middle streamwise locations.

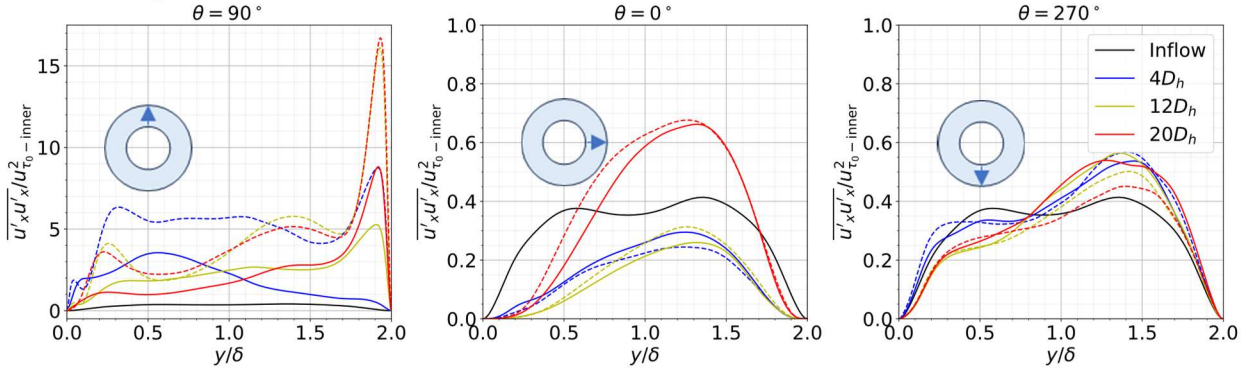

Figure 4.19. Comparison of x-direction Reynolds stress component profiles for three different angular positions along the heated part for cases 2 “645-050-G” (solid line) and 3 “645-100-G” (dashed line).

Enhanced mixing can be tracked in the Fig. 4.19 (left) by the profile of x (angular) component. In the top region heated fluid trajectory merged and traveled through the outer wall where it was redistributed back to lower regions. The peak near the outer wall confirms this behavior. The magnitude of this event was greater within the increase heat flux in case 3. However, the same behavior was not observed in the lower regions since the extend of the secondary flow had limited effects on the core flow part in these regions.

The correlation between the wall-normal and streamwise (shear) components plotted in Fig. 4.20, that quantifies the turbulent energy transferred between these two directions. In the top region, negative values of the stress profiles are caused by fluid particles moving upward with a greater-than-average. As they do, they slowdown in the streamwise direction. The combination of these

two events coincides with the elevation of the angular component that was linked with the enhanced mixing of the heated fluid. The interchange between three different locations indicates that described mixing event had not directed to single direction in the annular gap.

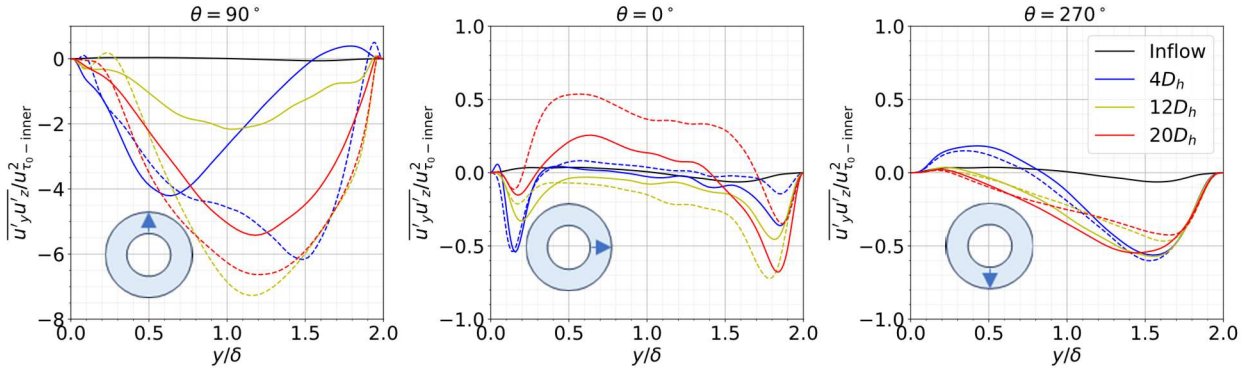

Figure 4.20. Comparison of y direction and streamwise direction correlation of Reynolds stress component profiles for three different angular positions along the heated part for cases 2 “645-050-G” (solid line) and 3 “645-100-G” (dashed line).

On the other hand, immediate rise at the vicinity of heated inner wall in Fig. 4.18 (left) continued with relatively stable profile instead monotonic growth within the wall distance. The stagnation in the growth of x component in Fig. 4.19 (left) and immediate rise of the y component in the core flow indicate that turbulence was suppressed at least in one direction. The instant behavior changes and existence of two distinct behaviors in the same region simultaneously are unusual for the wall bounded flows without heating effects within the absence of strong pressure gradient. The complex structure pictured here confirms the presence of a stratified layer in the flow. In Fig. 4.20, the extent of the stratified layer was not limited with the top region. In the side region, immediate rise of the y component Reynold stress at the vicinity of the inner wall exhibited a similar attribute with the angular component in the top region. Meaning that stratified layer occurs at the lower regions and strengthens with both elevation and flow progress.

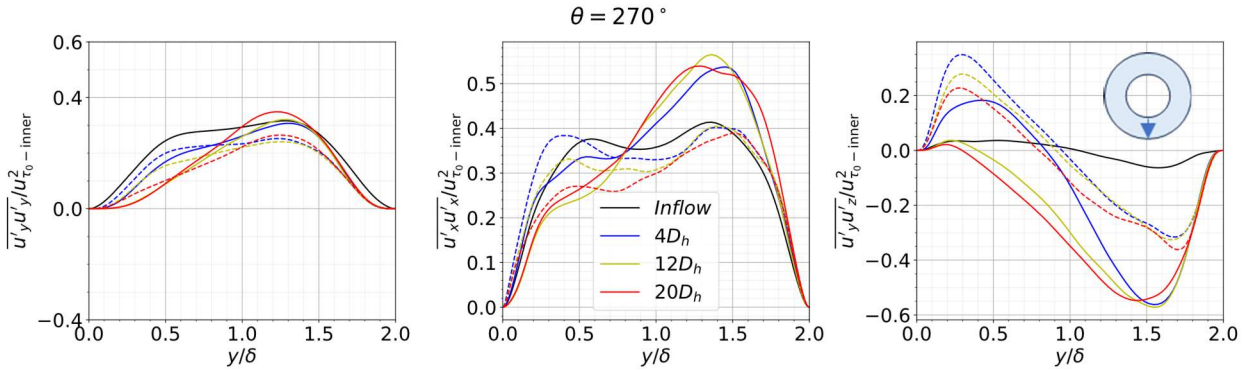

Figure 4.21. Comparison of y, x, and y-z correlation Reynolds stress component profiles along heated part for cases 2 “645-050-G” (solid line) and 4 “645-050-N” (dashed line).

The cross-flow part of the secondary flow is active within the presence of the gravity. The characteristic behaviors regarding the pronounced heated flow events in the case 2 were not observed in the case 4. Similarly to the previous section, wall normal, angular and shear stress components for the bottom region of the case 2 and case 4 were plotted for comparison in Fig. 4.21.

The trend changes due to cross flow were not valid for the case 4. However, the shear component presented higher values than case 2. If we consider similarities in the wall normal and angular stress components, the change in the streamwise direction fluctuation momentum component was larger which indicates that turbulence developed more in the single direction. Observed growth diminished significantly with the flow progress which indicates the laminarization event at the near heated wall.

The cross-flow part of the secondary flow was investigated in this subsection in terms of buoyancy and thermal stratification of the fluid. However, the laminarization is another important part of the secondary flow that needs to be investigated in detail due to its effect on the turbulence and heat transfer. These points were discussed in the next subsection with further remarks made regarding buoyancy effect and stratification of the fluid.

4.2.2 Laminarization

Heating provided not only caused the buoyancy, also altered the turbulence throughout the flow field. It was noted that the streamwise component of the Reynolds stress was the dominant component among principal stresses. Therefore, the change in the streamwise Reynolds stress component and turbulent kinetic energy were investigated for the further understanding regarding the local laminarization of the flow.

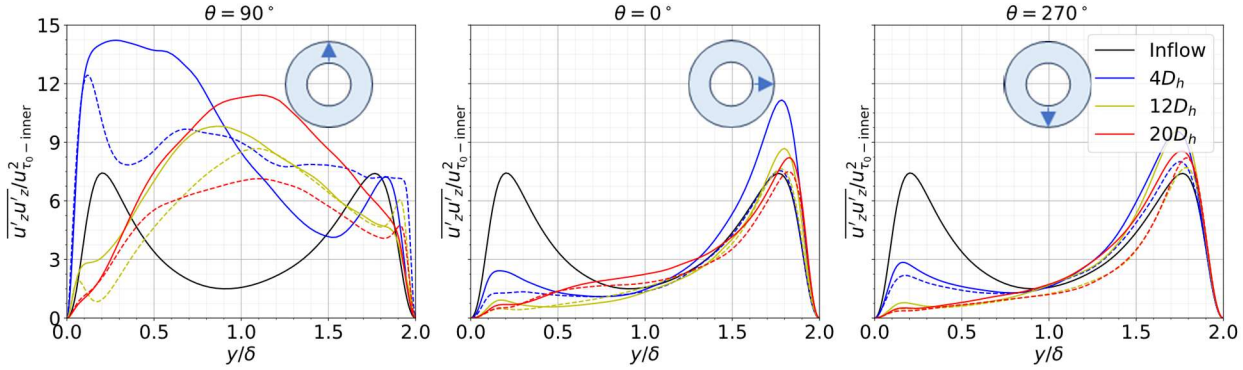

Figure 4.22. Comparison of streamwise Reynolds stress component profiles for three different angular positions along the heated part for cases 2 “645-050-G” (solid line) and 3 “645-100-G” (dashed line).

The streamwise component of the Reynolds stress profiles is plotted in Fig. 4.22 to understand the streamwise behavior of fluctuating momentum transfer. The initial rise observed at the top region for both cases was due to the early effect of heating. Case 3 exhibits a sharper peak at the near-heated wall and then attempts to form plateau for the further locations. Such behavior indicates the early formation of a stratified layer that separates near-wall region behavior from core flow region. Vortical structures mentioned in the SFI map (Fig. 4.11) also occurred in this region. In both cases, the stratified fluid layer acts as a barrier that creates two zones of turbulence. In the first part, streamwise component peak at the near wall, and enters the plateau in the second part that is location in the core flow region. Later, the initial rise significantly diminished and completely lost its near wall rise observed in the inflow part. This is clear evidence of the local laminarization of

the flow where Reynolds stresses are suppressed due to decreased viscosity of the heated fluid. The stratification event was experienced more intensely in case 3 that turbulence was immediately being suppressed after the near inner wall region. However, the cause of the immediate suppression was the product of the heating effects rather than heat flux alone. The heated flow redevelopment occurs in stages that was observed in the streamwise velocity profiles of the case 1 (640-050-G) and case 5 (650-050-G) in Fig. 4.6. Later, the top region streamwise turbulence significantly diminished and stabilized within the flow progress. The delay of the laminarization is connected to the initial burst of the buoyancy effect that temporarily created high mixing region. The local laminarization was not unique to the top region which appeared in all regions near heated wall locations. Unlike the top region, lower regions exhibited continuously decreasing streamwise Reynolds stress profiles along the heated part.

Figure 4.23. Comparison of turbulent kinetic energy profiles for 3 different angular positions along the heated part for cases 2 “645-050-G” (solid line) and 3 “645-100-G” (dashed line).

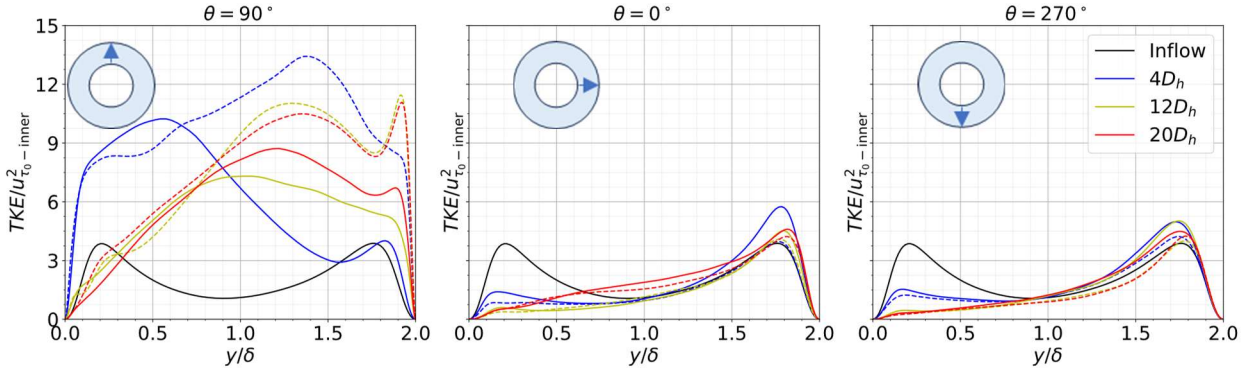

Turbulent kinetic energy profile in Fig. 4.23 provided an overall picture of the evolution of turbulence among all principal stress components investigated. The distinctive early sharp rise, primarily due to the streamwise stress component and partial contributions of cross flow components confirmed that flow exhibits two different behaviors that acts as layers. Additionally, laminarization of the flow can be observed through the suppressed turbulence especially after $4D_h$ location. Later, the contribution of cross flow components supports high turbulent kinetic energy at the core flow and near outer wall regions while near heated wall profile of turbulent kinetic energy diminishes. The reduction in this region was due to the decreased viscosity that reduced molecular interactions sourcing the formation of new eddies. In overall, turbulence in the top region is mainly driven by the interaction between the secondary flow and the main (streamwise) flow while its being suppressed by the laminarization at the near heated wall region. Further insight can be gained by the separation of the cross-flow components from the flow domain. The turbulence statistics of case 4 included the comparison by Fig. 4.24 to observe changes in the absence of the gravity.

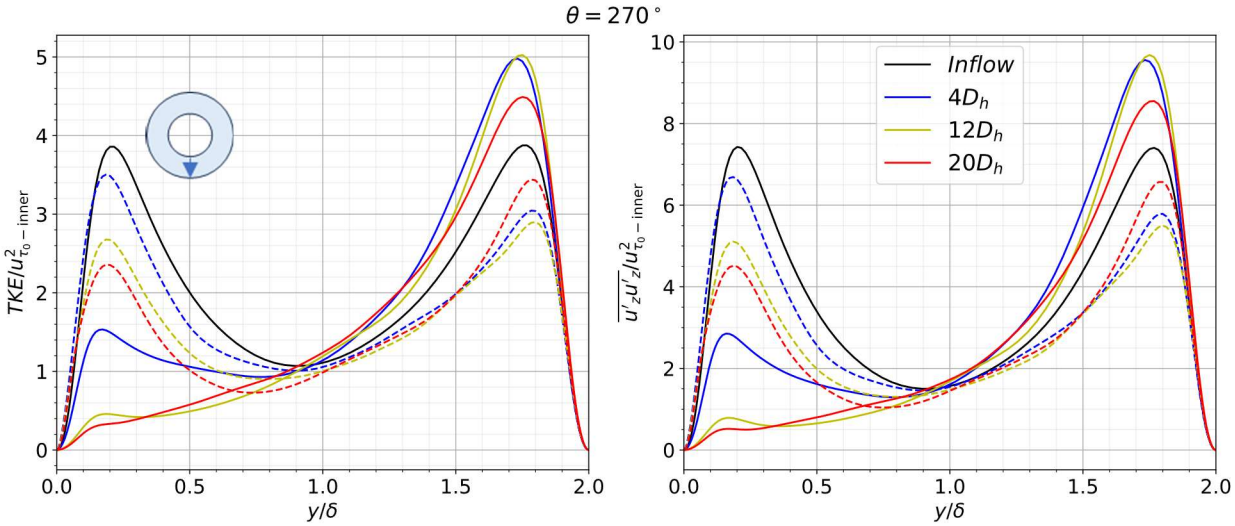

Figure 4.24. Comparison of turbulent kinetic energy and streamwise Reynolds stress component profiles along heated part for cases 2 “645-050-G” (solid line) and 4 “645-050-N” (dashed line).

It was observed that the degree of the laminarization was lower in the absence of gravity in comparison to the bottom region of the case 2. It means that the significant part the turbulent kinetic energy was being carried away by the buoyancy. However, the sole effect of the heating was still contributing the local laminarization of the flow due to decreased viscosity at the near heated wall. Furthermore, the evidence on the thermal acceleration of the flow was observed in the Fig. 4.24 as well. The streamwise stress component profile in the outer wall region exhibited gradual increase along the flow progress. This means that the extent of the expansion of the heated fluid along with the reduced shear also slightly affects the turbulence at the near outer wall regions through increased streamwise velocity.

Considering the information gathered by the investigation of all principal stress components, the flow domain exhibited highly anisotropic turbulent flow. In next subsection, the turbulent anisotropy of the flow is investigated to provide detailed picture regarding local changes of the anisotropic states of the heated turbulent flow.

4.2.3 Turbulent anisotropy

The barycentric invariant maps were plotted to observe the localized anisotropic states of the flow field. The response of the flow field on the secondary flow events was connected with the sweep and the ejection events of turbulence anisotropy.

The state of the turbulent structure depends on its rotational movement. In Fig 4.25, sampled data have been plotted with a color scale to identify the wall distance locations qualitatively. The red (warm) color symbolizes data obtained near the heated wall, and blue (cool) color refers to locations near the outer wall. Additionally, the data set for case 2 is shown with circles, and the data set for case 3 with triangles. The anisotropic state of the turbulence inflow part in Fig. 4.3 was clustered on the 1C turbulence oriented on the streamwise direction.

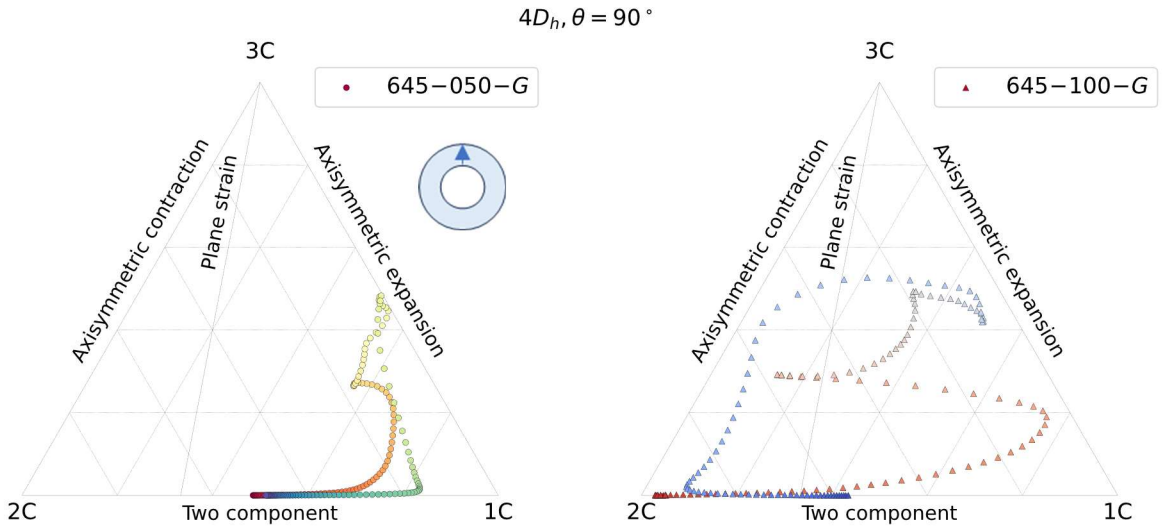

Figure 4.25. Comparison of barycentric maps of the anisotropy tensor for $4D_h$ location of the heated part at angular position of $\theta = 90^\circ$ for cases 2 (645-050-G) and 3 (645-100-G).

As the flow is heated, the heated fluid is subjected to upward movement (or stress) that also contributes to Reynolds stresses. The directional change by secondary flow shifts the data points obtained near the heated wall closer to a two-component state. The initial movement from the 1C corner to the 2C line results from buoyancy effect. As heated fluid particles have started to move away from the wall, contributing to the y-directional velocity/stress that resulted in an ejection of the turbulent structures in this direction. As those particles reach the top or the vicinity of the outer wall, another contribution comes from the enhanced mixing (thermally induced), which can be traced within the reaction of x-direction Reynolds stress component. The state of the structures approached a to a 3C state where both buoyancy effects and radial movement due to enhanced mixing are present. Later, as the buoyancy effect has lost its initial strength, the state of turbulent anisotropy approached to 2C state where eventually took a disc-like form at the near outer wall. The turbulent-anisotropy evolution was entirely different between case 2 and case 3. Higher heat flux exhibited stronger secondary flow events. Their presence against the main flow (streamwise) became more pronounced as mentioned. The plain strain line has drawn to indicate that the two principal terms (or movement of rotation) of Reynolds stress are almost equally dominant independently from the third principal term. This line has crossed multiple times due to a chaotic state in the core flow region. Furthermore, turbulent structures in case 3 were extending to the isotropic state already at the early stages heated part.

The flow re-development of case 2 reached its most chaotic state at the middle locations of the heated part. Flow stratification at the early and middle stages appeared in these regions where the evolution of the anisotropic state has evolved steadily, then subjected to chaotic instantaneous effects as the stratified layer is crossed. In the late stages, a new equilibrium was being established through the flow re-development.

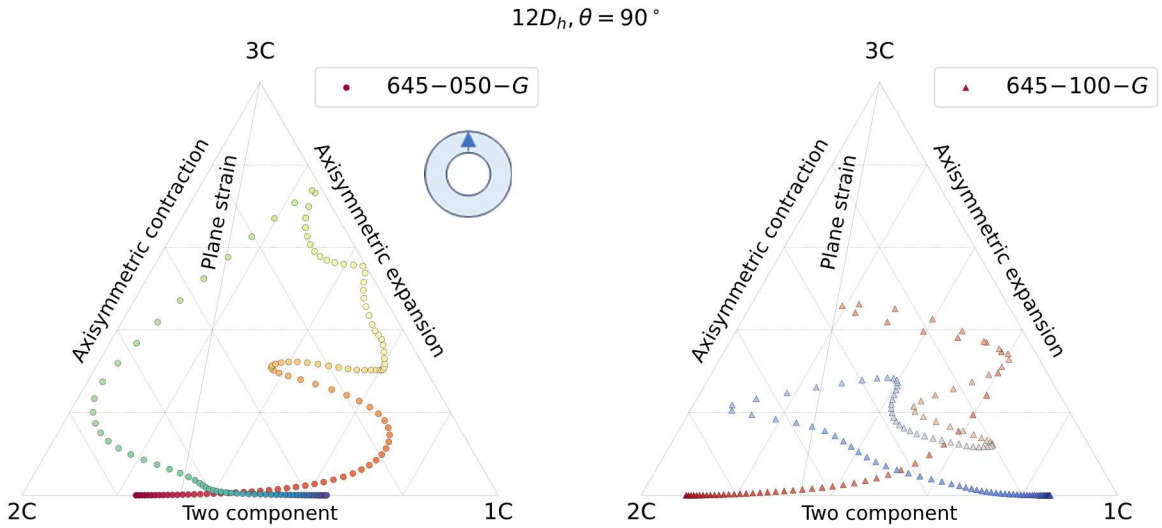

Figure 4.26. Comparison of barycentric maps of the anisotropy tensor for $12D_h$ location of the heated part for the angular position at $\theta = 90^\circ$ for cases 2 (645-050-G) and 3 (645-100-G).

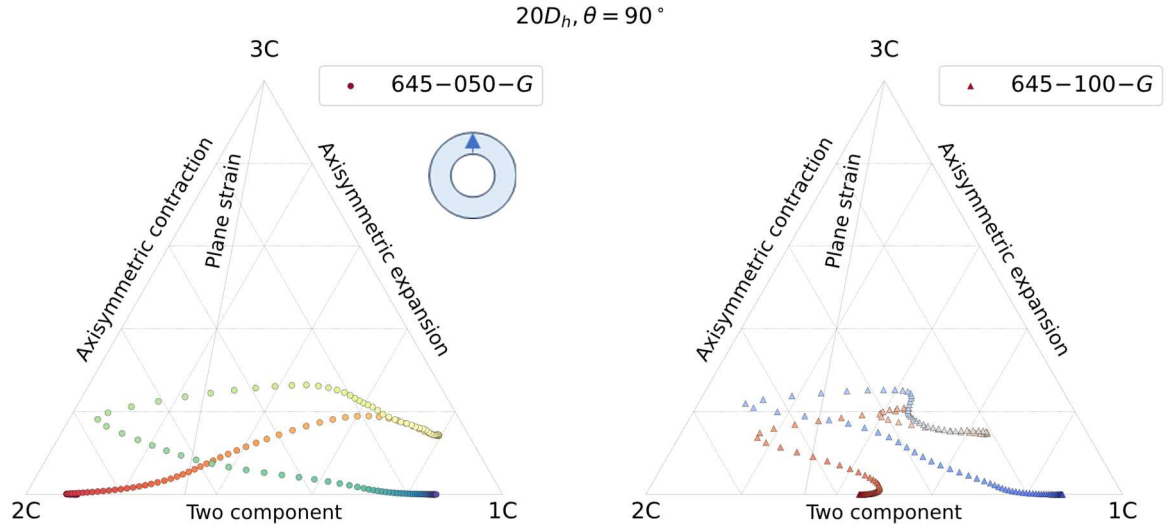

Figure 4.27. Comparison of barycentric maps of the anisotropy tensor for $20D_h$ location of the heated part for the angular position at $\theta = 90^\circ$ for cases 2 (645-050-G) and 3 (645-100-G).

The plotted evolution trajectory through the end locations of the heated part presented in Fig. 4.26 and 4.27. The evolution trajectory plotted for case 2 became steadier as flow re-development progresses under heating effects. However, very complex trajectory of anisotropic state still was observed for the case 3. Indicating that flow re-development has not reached its final state yet. In overall, turbulent structures became steadier and the distribution is broader at in between 1C and 2C states with small contribution of 3C within the barycentric map triangle. This formation aligns with the steady presence of buoyancy and enhanced mixing over dominant streamwise flow movement.

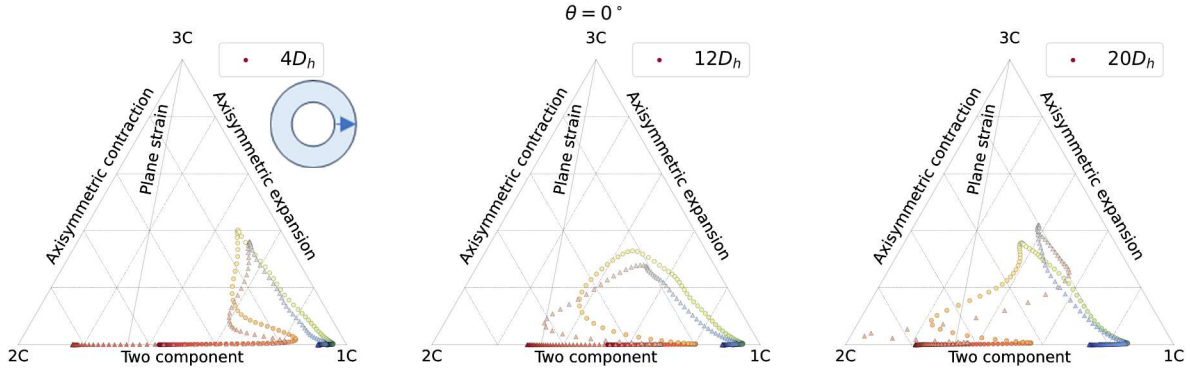

Figure 4.28. Comparison of barycentric maps of the anisotropy tensor for $4D_h$, $12D_h$ and $20D_h$ locations of the heated part for the angular position at $\theta = 0^{\circ}$ for cases 2 "645-050-G" (circles) and 3 "645-100-G" (triangles).

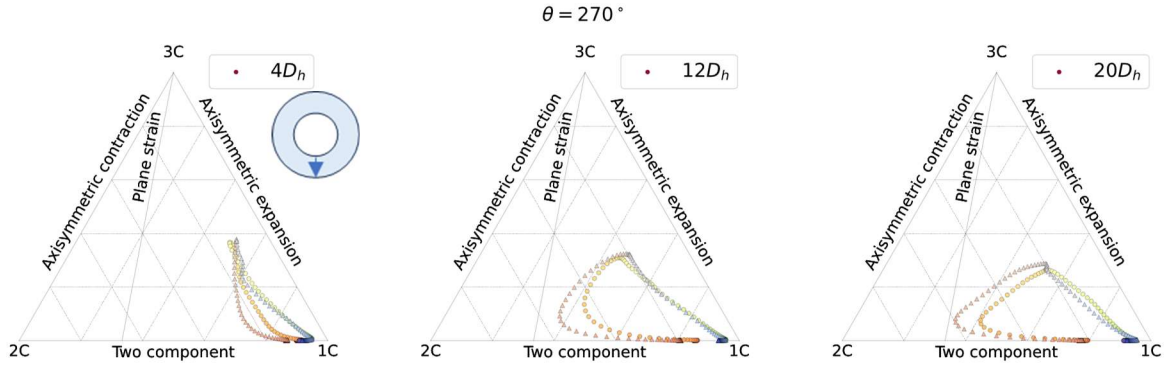

Figure 4.29. Comparison of barycentric maps of the anisotropy tensor for $4D_h$, $12D_h$ and $20D_h$ locations of the heated part for the angular position at $\theta = 270^{\circ}$ for cases 2 "645-050-G" (circles) and 3 "645-100-G" (triangles).

Other regions were not significantly affected by the simultaneous presence of secondary flow events, unlike the top region. The path trajectories of plotted data in Fig. 4.28 and 4.29 for angular positions θ=0° and θ=270° has shown a relatively similar trend, indicating shift to the 2C state near the heated wall and a more stable path of evolution for anisotropic state. 2C state at the near heated wall evolved closer to the 3C state for the core flow region. It is possible to distinguish the effect of buoyant movement and the laminarization events simultaneously active in the side region. In bottom region, upward movement of the fluid is not strong as side regions. Therefore, small shift to the 2C state (in comparison to side region) is linked to the flow laminarization / acceleration events. As side regions were affected more from the secondary flow, they presented more sophisticated evolution in the first half of the annular gap starting from the 2C state. The return path of the secondary flow affects the side region core flow locations. The presence of the enhanced mixing appeared as turbulent structures clustering more at the 3C state in the core flow region. In bottom region, these formations appeared without the presence of enhanced mixing in the core flow region where more linear approach to 3C state was observed. In both regions, the path continued similarly to the inflow part's 1C state in the second half of the annular gap. There was no distinctive behavior spotted regarding the effect of the heat flux in both side and bottom regions.

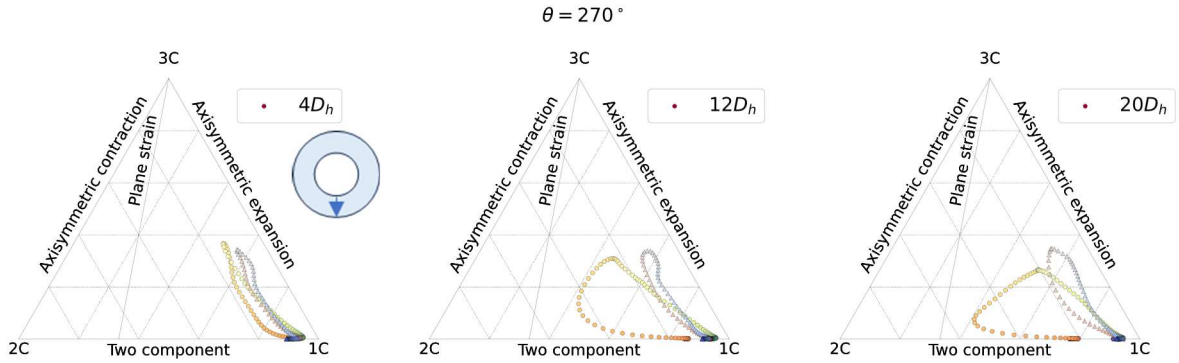

Figure 4.30. Comparison of barycentric maps of anisotropy tensor for $4D_h$, $12D_h$ and $20D_h$ heated part for the angular position for $\theta = 0^{\circ}$ for cases 645-050-G (circles) and 645-050-N (triangles).

The characteristic initial shift to 2C states followed by the approach to the 3C state of turbulence were observed under the presence of gravity that enables buoyancy effect and enhanced mixing of heated fluid. The anisotropic map for the case 4 was plotted to investigate the changes as cross flow events are discarded. The anisotropic states for case 4 were shown in Fig. 4.30 that exhibited limited development to heating effects so far in contrast to case 2. Sampled data were mainly clustered at the 1C corner with slight progress to the 3C state. This is due to the thermal acceleration of the flow that presented broadened from obtained in the inflow part. The return to initial state was possible for case 4 in near outer wall region since extend of heating effects were not strong enough to set discrepancy.

4.2.4 Transport of turbulent kinetic energy

The turbulence inside the flow field was subject to enhancement and suppression of turbulence by several phenomena, such as buoyancy, cross flow, laminarization and enhanced mixing due to heating effects.

Further understanding on the effects of these flow events on turbulence can be gained by the investigation of budget terms for the transport of turbulent kinetic energy. The initial efforts put on the understanding how turbulence kinetic energy transport reacts through flow domain by production, buoyancy, dissipation, and diffusion components.

The transport budgets of the turbulent kinetic energy and their development through the heated part at the top region for case 2 in Fig 4.31. The shear production term initially exhibits the peaks observed in the inflow part (Fig. 4.4) indicates that the production at the near wall regions was active at the beginning. Later, production in the near inner wall diminishes and changes its sign to negative (destruction) especially in the first half of the annular gap. In this region, the stratified layer of the fluid still exists which suppresses turbulence that eventually promotes local laminarization.

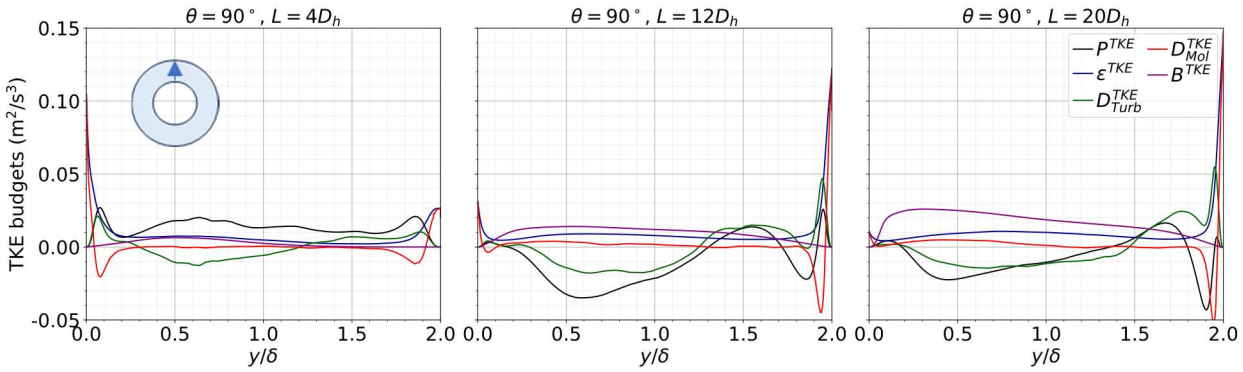

Figure 4.31. Comparison of turbulent kinetic energy transport budget profiles for angular position $\theta = 90^{\circ}$ along the heated part for case 2 (645-050-G).

The turbulence was being carried away by turbulent diffusion until to the point that secondary flow is being redistributed at the near outer wall region by enhanced thermal mixing. In this region, both production and turbulent diffusion terms return to positive indicating that turbulence both being produced and being imported to near outer wall regions by cross flow. Molecular diffusion is mostly effective in the bear wall regions where molecular interactions due to viscosity are important. However, its presence diminishes like other mechanisms due to laminarization. The dissipation of turbulent kinetic energy follows the overall trend change along heated part as turbulent activity diminishes, it loses its magnitude simultaneously. The buoyancy production term gradually evolves from the beginning to the end of the heated part that peaks within the stratified layer of fluid and loses its strength with elevation to the outer wall. The transport budget profiles plotted for case 2 heated part were used as basis for the further evaluation.

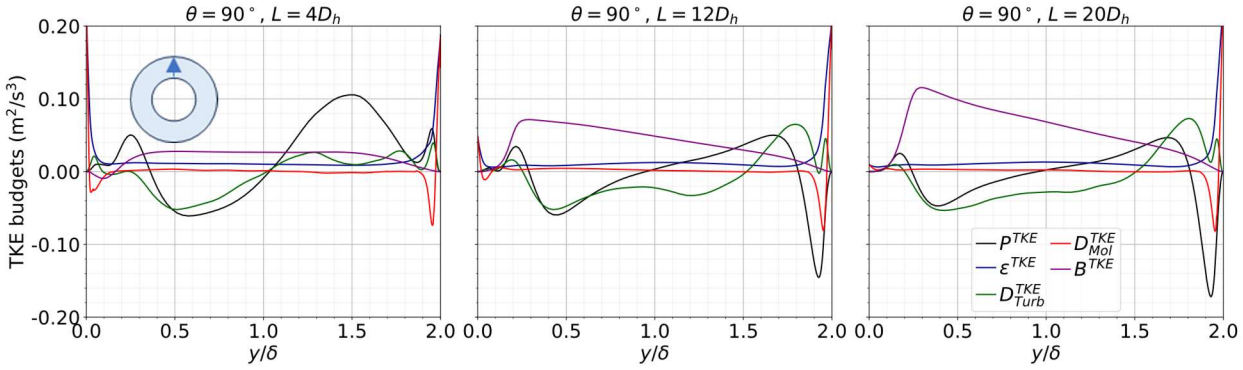

Figure 4.32. Comparison of turbulent kinetic energy transport budget profiles for angular position $\theta = 90^{\circ}$ along the heated part for case 3 (645-100-G).

In Fig. 4.32, budgets for turbulent kinetic energy transport plotted for case 3 in the same streamwise locations. The increased heat flux has a direct effect on the production of turbulent structures, as heating induced secondary flow-initiated interchange between directional momentum components. Turbulence production is mainly connected to two core mechanisms: shear and buoyancy. The production by shear weakened at the early stages of the annular pipe, where the turbulent heated flow was in the re-development phase. However, buoyancy contribution evolved with the flow progress. It was evident in Figures 4.31-4.32 that more distinctive stratified layer formations occur with increased heat flux. The stratified layer formation affected both shear and buoyant production as intensified layer created a local region where

production is peaked for a small distance from the inner wall. In general, the changes observed in the diffusion and dissipation terms were more pronounced in case 3 than in case 2.

The most distinctive separation is observed in the turbulent diffusion budget. Therefore, the shear production (Production), buoyancy production, and turbulent diffusion terms are investigated in detail to further assess the effect of heat flux. Other terms did not provide any distinctive information, since their main difference is that budget terms take greater values. Production terms and the turbulent diffusion term have been investigated by a comparative analysis between case 2 and case 3 heated parts.

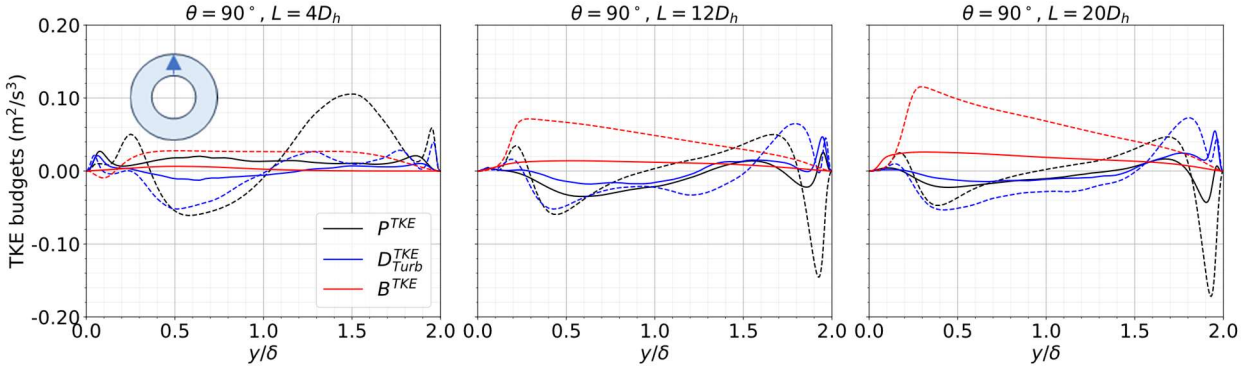

Figure 4.33. Comparison of shear production, buoyancy production, and turbulent diffusion budget terms for turbulent kinetic energy transport for angular position $\theta = 90^{\circ}$ along the heated part for cases 2 “645-050-G” (solid line) and 3 “645-100-G” (dashed line).

In Fig. 4.33, extent of the flow redevelopment can be observed through heated part. Weak shear production is caused by heating effects that result in decrease in viscosity, and thermal expansion of the fluid. These changes diminish the molecular interactions that are strong enough to produce new ones. The production by shear is responsible for the formation of new turbulent structures (positive production) that were intense enough to compensate for the destruction (negative production) of old ones by the bulk flow. Negative production was mainly observed at the first half of the annular gap closer to the heated wall and near the outer wall in the further stages. Abovementioned mechanisms led to laminarization of the flow. Existing and newly generated turbulent structures were carried away (exported) by negative turbulent diffusion term in the first half of the core flow region as they cross a stratified layer. In the second half of the annular gap, production by shear became positive along with the turbulent diffusion (import), as the dispersion of the heated fluid to other regions begins. These trend behaviors shift closer to the outer wall as the flow redevelops. The buoyancy contribution develops steadily in positive contribution across the annular gap. It peaks immediately after the near-wall region and then monotonically decreases as it approaches the outer wall. It should be reminded that destruction, exporting by diffusion and dissipation are different mechanisms. Apart from the other two, dissipation budget identifies turbulent structures are dissipating into smaller scales and eventually molecular internal energy.

In general, the above-mentioned changes are observed in greater magnitude in case 3 compared to case 2 with exception of several distinct local behavioral changes that have been observed in Fig. 4.33. Case 2 exhibits steady positive shear production at the beginning of the heated part across the core flow region. In this part, the stratified layer is not fully formed, unlike in the early burst of buoyancy observed in case 3. In case 3, buoyancy response caused a negative buoyancy

contribution at the near wall, meaning that heated fluid is pulled back to the wall surface during the emergence period. Additionally, stratified layer formed on inner wall surface appears as negative production by shear.

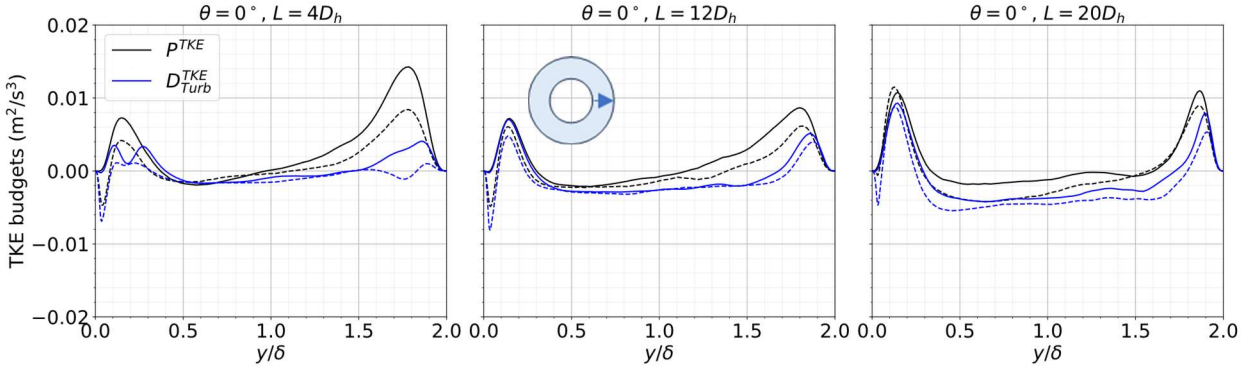

Figure 4.34. Comparison of shear production and turbulent diffusion budget terms for turbulent kinetic energy transport for angular position $\theta = 0^{\circ}$ along the heated part for cases 2 "645-050-G" (solid line) and 3 "645-100-G" (dashed line).

Unlike the top region of the annular pipe, the symmetric profile in the inflow part was less affected by the heating at the side region ($\theta = 0^{\circ}$) where production and turbulent diffusion budgets for turbulent kinetic energy were plotted in Fig. 4.34. The effect of the heating on transport budgets was limited in the near wall region at the angular position of θ=0^{0}. The production by shear suppressed by the entry effects that are reflected as early local laminarization for both cases. In case 3, observed decrease switched into destruction state under the effect of higher heat flux applied. Later, production budget entered recovery phase that continued until the late locations of the heated part for both cases. However, destruction state persisted in the core flow region throughout heated part especially for case 3. The recovery received from the near wall was not sufficient in this sense even though turbulent diffusion efficiently transports the turbulence. The balance of the budget terms allowed bulk flow to continue under laminarization and acceleration effects. The instant transition from destruction to production state in the near wall coincides with the location where the critical temperature is crossed. The buoyancy production term was only effective in the vicinity of the heated wall due to buoyant movement of the heated fluid. It is presence aligns with the SFI map in Fig. 4.10-11.

The bottom region was the least affected region by the secondary flow events. Therefore, case 4 statistics on the transport of the turbulent kinetic energy presented in Fig. 4.35 to assess the extend the laminarization and thermal acceleration on turbulent kinetic energy. The observed effect of laminarization was previously mixed with other effects of secondary flow in the case 2. As gravity removed, changes caused by decreasing fluid viscosity and density along the heated part were evident. A gradual decrease in the production and turbulent diffusion terms was confirming that turbulence is suppressed. The effect of the heating suppressed turbulence can be distinguished by the comparison of the inner wall and outer wall statistics. There was no further noticeable difference has been observed due to heating effects.

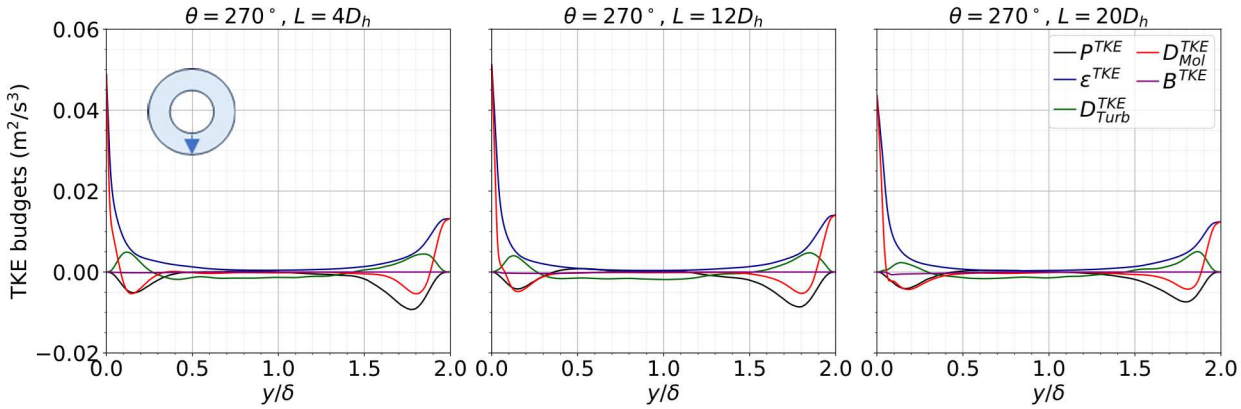

Figure 4.35. Comparison of turbulent kinetic energy transport budget profiles at $\theta = 270^{\circ}$ along the heated part plotted for case 4 (645-050-N).

Investigation of the turbulent kinetic energy transport budgets has made it possible to emphasize the mechanisms behind the changes in turbulent kinetic energy under heating effects that resulted in the complex effects of secondary flow induced.

4.2.5 Summary

The fluctuating momentum statistics were investigated within the flow phenomena's introduced in the section 4.1. The effective mechanisms covered in the secondary flow were separated to two main phenomena as buoyancy effect and laminarization.

In the case of the buoyancy effect, the cross flow related components of the Reynolds stresses were investigated for each region identified. Additionally, the shear component included into analysis to assess the effect of the streamwise flow component. It was possible to observe the presence of buoyancy through the wall normal component of the Reynolds stresses that appeared with the rapid emergence at the early stages which is stabilized through the heated region. The angular component provided the locations for the enhanced mixing in all regions that is aligned with the SFI map plotted. The extent of the buoyancy effect was being distributed by the curvature of the wall that affects the side region and slightly the bottom region for the case 3.

Flow laminarization was present through all heated part with the exception of the late emergence in the top region which was covered by the rapid emergence of buoyancy effect. Vortical structures that appeared in this area as heated fluid immediately cross the pseudo-critical region, where buoyancy response is covered by the suction of the colder fluid. These structures caused local enhanced mixing at the near wall that contributed to the rapid rise of the turbulent kinetic energy due to the immediate rise of all principal components of the Reynolds stress tensor. In the same locations, viscosity decreases drastically along with the density which damps the reproduction of turbulent structures and contributes to the thermal expansion of the fluid. Decreased shear and mass balance led to the bulk velocity rose continuously that formed thermal acceleration part of the secondary flow. These events completed the picture for the stratified layer of the fluid that

created plateau regions for the streamwise component of the Reynolds stresses aligned with the streamwise mean velocity profile.

The anisotropic state of the turbulence was very responsive to flow events in the heated part. It is important to mention that the flow field provided by the inflow part was already highly anisotropic due to the narrow annular gap provided. As the streamwise stress component dominated the principal Reynolds stresses, initial anisotropic state of the flow was close to the 1C state. The return of isotropy [16] was not ideally possible in the provided flow conditions, even though evolution trajectory followed the path to the 3C state with limited freedom provided by the annular gap. As flow was subjected to the heating, immediate shift to the 2C state occurred due to ejection of turbulent structures by buoyancy in the near heated wall. Also, evolution trajectory approached to the 3C state in the core flow region by the help of secondary flow. These changes were experienced in a broader range for the case 3 due to stronger heating effects. In case of side region, the layer that was carrying heated fluid upwards caused further shift to the 2C state. The bottom region remained relatively stable as the least affected region. However, the evolution of the anisotropic state approached further to the 3C state due to the effect of the laminarization. Other directions of fluctuating momentum transfer became more important as streamwise component of Reynolds stress diminished throughout heated part.

These changes are mainly driven by the production, buoyancy, and turbulent diffusion budgets of the turbulent kinetic energy transport. The contribution of production budget was challenged under the presence of the stratified layer that suppressed both transport and production of the new turbulent structures in the first half of the annular gap near the inner wall. The joint effects of the reduced shear, buoyancy movement were not sufficient to contribute the balance positively in these regions. The trend turned positive in the second half of the annular gap by the aid of enhanced mixing that is initiated by the dispersion of the heated fluid.

The simultaneous presence of the effects mentioned above summarizes the momentum part of the flow field. These outcomes were supported with the turbulent heat transfer part of the flow field in the next section. In this way, temperature fluctuations, and their unified contribution with the velocity fluctuations to the flow field were investigated.

4.3 Turbulent heat transfer statistics

Investigations made in this section mainly focused on the turbulent heat transfer and its transport budgets to describe how heat is distributed in the throughout flow domain. The temperature fluctuations, two-point correlations of velocity – temperature fluctuations and transport budgets were analyzed for this purpose. Sampled data obtained from cases 2 (645-050-G), 3 (645-100-G) and 4 (645-050-N) to consider the effect of heat flux and presence of gravity. Later, solid wall statistics including mean temperature profiles, temperature variance and temperature gradient plotted to observe behavior of these quantities against different provided boundary conditions of the flow under supercritical pressure conditions.

4.3.1 Secondary flow

Temperature fluctuations and turbulent heat flux profiles as velocity-temperature correlations were plotted analyze how secondary flow events mainly driven by the buoyancy effect and enhanced mixing affects temperature field and turbulent heat transfer.

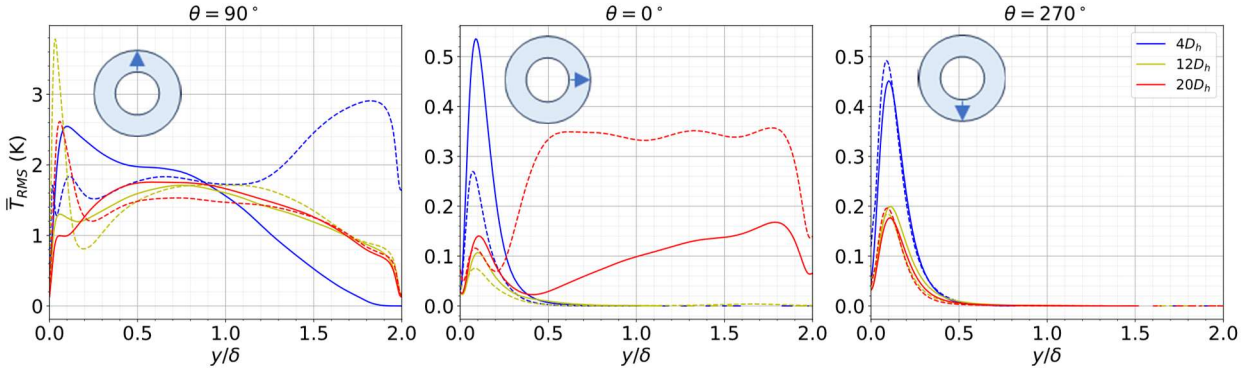

Figure 4.36. Changes in the temperature variance profile in the heated part for cases 2 "645-050-G" (solid line) and 3 "645-100-G" (dashed line).

Temperature variance profiles in Fig. 4.36 plotted in addition to mean temperature profiles presented in section 4.1. The temperature variance presented very chaotic picture that was caused by the several resources. The peak observed in the variance profile indicates that heat transfer is not only driven by temperature gradient. The turbulent transport was effective especially after the conductive sublayer where heat transfer by temperature gradient was dominant. As expected, the temperature variance is higher in regions with higher mean temperature values. However, its magnitude is also highly dependent on local changes in the flow field. The main source of these changes caused by the secondary flow events like buoyancy and thermal stratification of the fluid. At the top region, the main source of the near wall peaks due to buoyancy movement of the heated fluid almost at the solid – fluid interface which was followed by the plateau formation. Also, the presence of the enhanced mixing especially near outer wall inhibits instabilities in the flow at both near inner and near outer wall regions. The separation was more apparent in case 3 that initiated by the burst of buoyancy.

The contribution of enhanced mixing was observed clearly at the side region, where a slightly elevated mean temperature profile led to significantly higher temperature variance. In addition to this global trend evolution, it was observed that temperature variance surged at the near wall region, where the mean temperature profile crossed the pseudo-critical temperature. This rapid change in the temperature variance is sourced by changes in the thermophysical properties in the temperature range of the pseudo-critical region. The presence of the wall and its finite heat capacity treated the temperature fluctuations as preventing them to be overpredicted as a typical use of iso-flux boundary condition in the fluid wall surface [7]. However, the pseudo-critical region caused the damping of temperature fluctuations were partly offset due to instabilities in the near wall region.

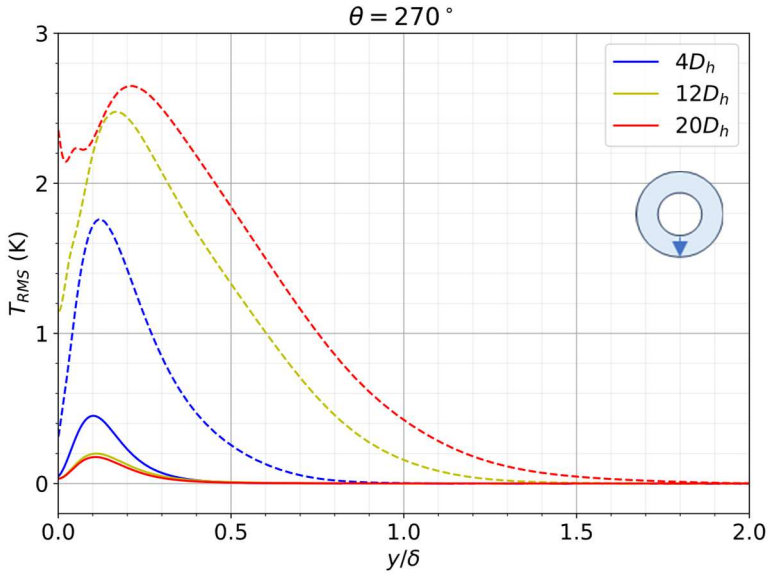

Figure 4.37. Changes in the temperature variance profile in the heated part at angular position of $\theta = 270^{\circ}$ for cases 2 “645-050-G” (solid line) and 4 “645-050-N” (dashed line).

The damping of the temperature fluctuations were challenged in the absence of the secondary flow as shown in the temperature variance profiles shown for case 4 in Fig. 4.37. Temperature oscillations obtained from the middle to end section of the annular pipe exhibited irregular profiles in comparison to early stages. As shown in Fig. 4.13, mean temperature profiles observed in case 4 reached further into annular gap since heated fluid did not escape due to absence of cross flow phenomena. Increased temperature and lack of enhanced mixing that transporting heated fluid away from the wall challenged the effect of the conjugate heat transfer. This means that temperature fluctuations sourced from the heat flux boundary at the inner side of the solid wall were able to penetrate wall thickness if the cooling were not supported by the secondary flow.

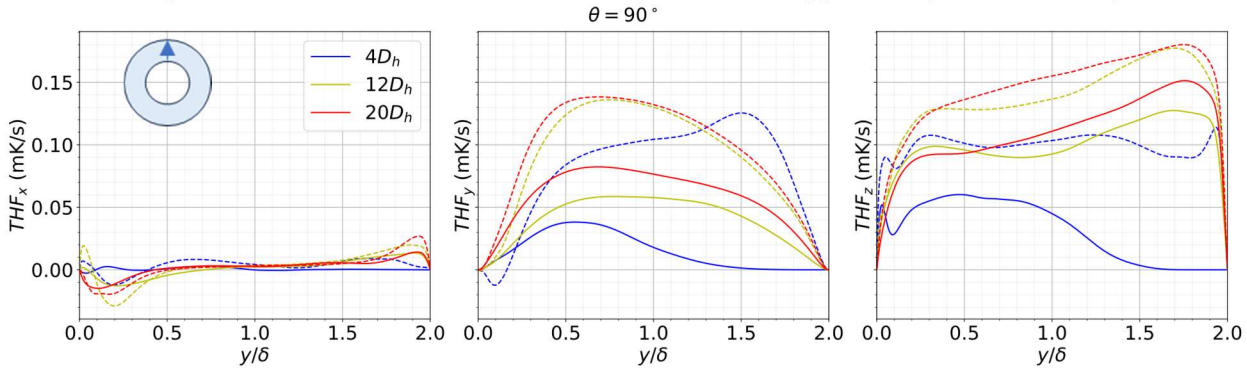

Figure 4.38. Comparison of turbulent heat flux profiles in 3 directions for angular position of $\theta = 90^{\circ}$ along the heated part for cases 2 “645-050-G” (solid line) and 3 “645-100-G” (dashed line).

Temperature variance highlighted instabilities on the temperature field in presented cases. However, temperature fluctuations were one of the two components the turbulent heat flux. Two-point correlations of velocity and temperature fluctuations allow us to analyze turbulent heat flux

behavior across flow field. For this reason, these correlations were investigated as they represent characteristic behavior of turbulent heat flux.

The turbulent heat flux consists of three components, as it includes velocity fluctuations and temperature fluctuations averaged over time. The development of the secondary flow also carries heated fluid away, where conductive heat transfer from the heated wall is no longer effective. Figure 4.38 shows that turbulent heat flux shaped by the secondary flow. In cases 2 and 3 buoyancy and thermal stratification features of secondary flow were predominant in the wall-normal and streamwise components. In the top region, trend development in the wall normal component (y direction) was driven by buoyant movement of the heated fluid. The streamwise direction trend development consisted both the effects of thermal stratification and enhanced mixing that was amplified by the increased heat flux. Both cases follow the similar development unlike the differences spotted in previous statistics. The sharp peak observed in the near heated wall was due to the response of streamwise component of the velocity and very steep fall of temperature profile that is followed by relatively stable path through outer wall. The initial burst of buoyancy led to the rapid development of the turbulent heat flux profile, which was the reason of near wall negative values in wall normal component. In detail, buoyancy effect was strong enough to pull colder fluid to the wall surface for a moment that formed a negative turbulent heat flux spot.

The contribution of temperature fluctuations was weaker in comparison to its momentum counterpart. In other regions, contribution received from temperature fluctuations becomes a limiting criterion for the turbulent heat flux since heated fluid immediately travels upward. Obtained statistics in Fig. 4.39 show that turbulent heat flux was only effective at the near inner wall region due to the steep fall of the temperature profile and limited presence of the secondary flow.

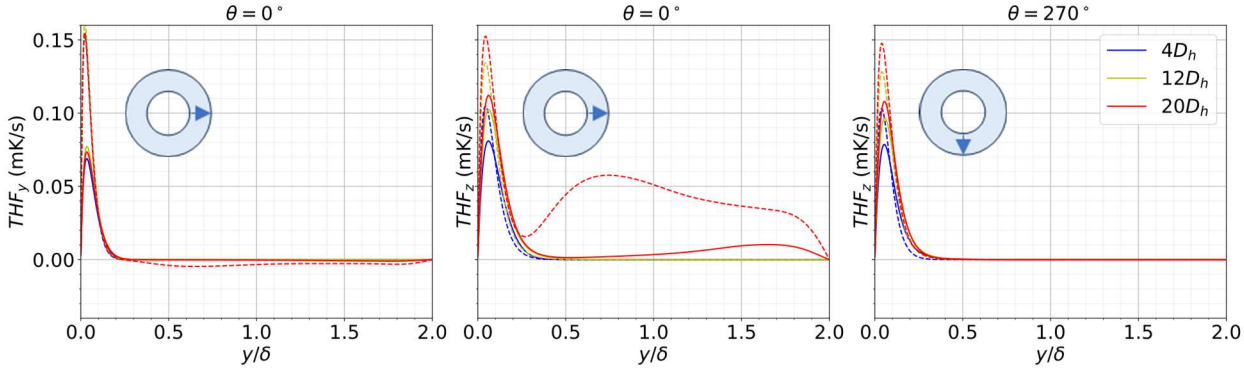

Figure 4.39. Comparison of selected turbulent heat flux profiles in y and z directions for angular positions $\theta = 0^{\circ}$ and $\theta = 270^{\circ}$ along the heated part for cases 2 “645-050-G” (solid line) and 3 “645-100-G” (dashed line).

The absence of enhanced mixing and buoyancy effect and elevated mean temperature profiles resulted in higher values in the streamwise turbulent heat flux component in case 4. However, absent cross flow led to negligibly small values in wall normal and angular directions. Therefore, only the streamwise component was plotted in Fig. 4.40 since there was no further evaluation possible.

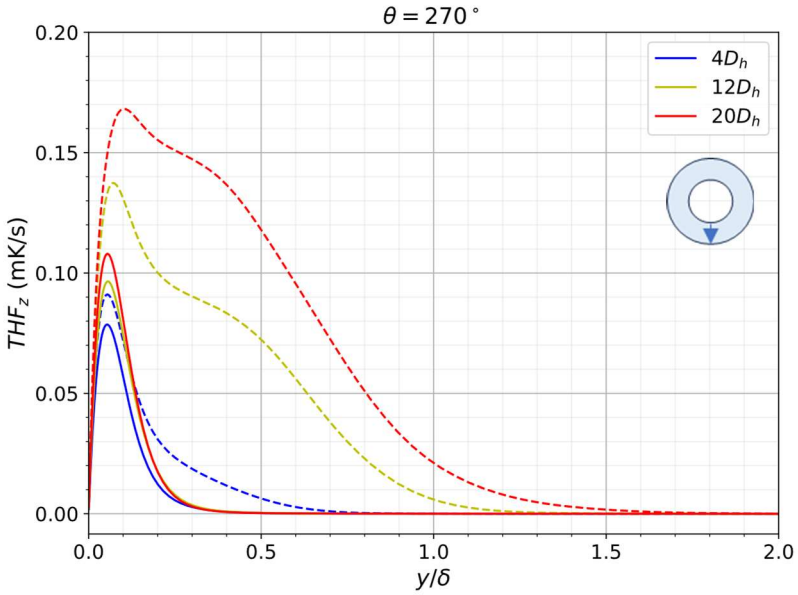

Figure 4.40. Comparison of streamwise turbulent heat flux profiles at $\theta = 270^{\circ}$ along the heated part for cases 645-050-G (solid line) and 645-050-N (dashed line).

In both cases, the streamwise components presented a peak at the near heated wall region. These peaks were broadened and amplified at the case 4 as temperature levels elevated significantly higher within the flow progress. The extent of the streamwise turbulent heat flux component was able to reach far ends of the annular gap through outer wall. Further details regarding the transport of the turbulent heat flux discussed in the following subsection.

4.3.2 Transport of turbulent heat flux

Investigation on the transport budgets of turbulent heat flux provides more insight about its productions, dissipation and diffusion mechanisms take place. It is crucial to state the physical meaning of the turbulent heat flux transport budget terms and their contributions, whether positive or negative. There are two production terms stated as, production 1 and production 2. Production 1 term represents the contribution from interactions between the temperature gradient and shear stress. Production term 2 is the interaction of turbulent heat transfer and bulk flow by means of velocity gradient. The diffusion terms resemble the transport of turbulent heat flux with related interactions, including turbulent, thermal (conduction), and molecular (viscous) effects. The local positive sign indicates production budget terms, meaning it produces turbulent heat flux at the location with a relevant interaction mechanism. The negative signs mean that turbulent interactions are being destroyed by the bulk flow connected to the relevant interaction mechanism again. Diffusion terms are transporting turbulent heat flux in (positive) or transferring out (negative) from neighboring regions. Lastly, the dissipation term describes the irreversible dissipation of turbulent heat flux to the smallest scales by both viscous and conductive mechanisms, causing them to disappear.

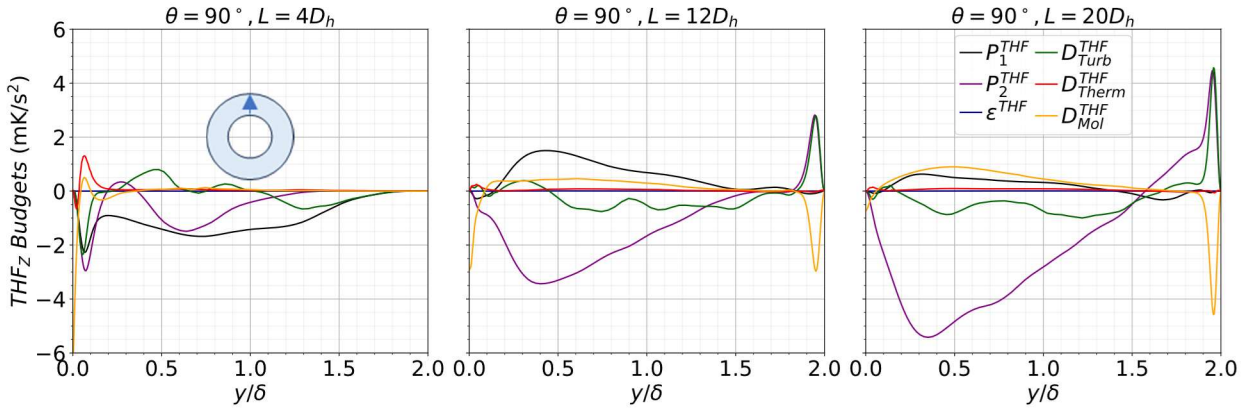

Figure 4.41. Comparison of z direction turbulent heat flux transport budget profiles for angular position $\theta = 90^{\circ}$ along the heated part for case 2 "645-050-G".

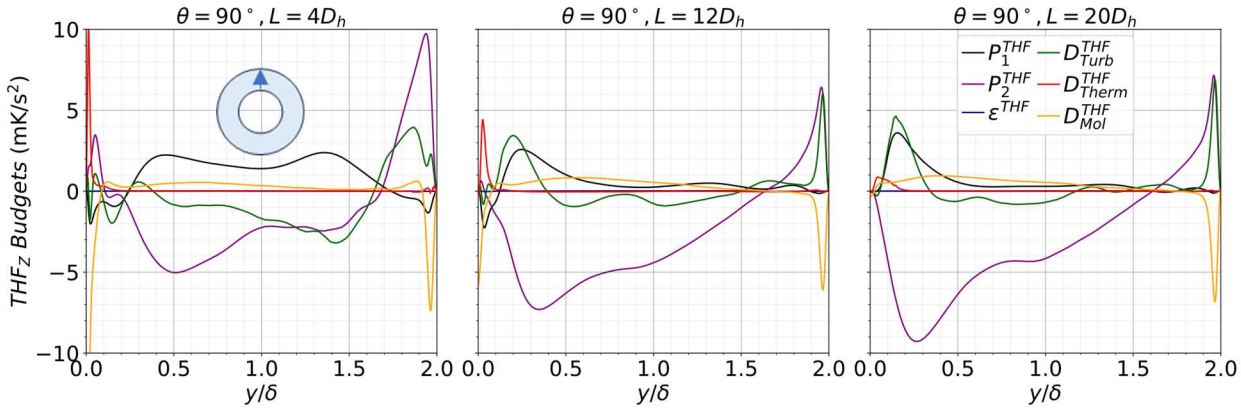

Figure 4.42. Comparison of z direction turbulent heat flux transport budget profiles for angular position $\theta = 90^{\circ}$ along the heated part for case 3 "645-100-G".

As the z-direction heat flux term shows the highest magnitude in comparison to the other components, transport budget profiles were plotted for the top region at the angular location of θ=90° that is shown in Fig. 4.41-4.42 for a prior look before comparative analysis. Although they were exhibiting similar trends, some budget terms have shown distinctive behavior. For this reason, the main focus has been given to budgets dealing with effective diffusion mechanisms and production terms. In both figures, thermal (conductive) diffusion term exhibited a sharp peak at the near inner wall region that was diminishing to the core flow region. The thermal diffusion term drives heat away from the heated wall surface by means of conduction. However, its extent is limited only within the conductive sublayer. The molecular diffusion budget is responsible of the heat transport through molecular interactions, meaning that turbulent heat flux is transported to outer regions with the help of fluid particle interactions. Both diffusion mechanisms lose their strength in the further regions of the annular pipe especially away from heated wall region.

The production 1 term (Reynolds stress – temperature gradient interaction) becomes effective by the distance further away from the inner wall. Initially it contributed to the bulk flow with destruction of turbulent heat flux in the stratified layer and changed its behavior to production state as temperature gradient approached to the zero. The turbulent diffusion term functioned as a counter - term that transports the produced turbulent heat flux away from the inner wall region through annular gap. Meantime, the production 2 term (turbulent heat flux – velocity gradient

interaction) has removed the turbulent heat flux to contribute to the bulk flow except in the near outer wall region, where enhanced mixing of heated fluid was observed. In overall, the turbulent heat flux was being carried away or removed by the acting flow mechanisms where these events were more pronounced in case 3 rather than case 2, since higher heat flux was applied. Production terms and turbulent diffusion terms have been selected for comparative analysis in Fig.4.43, as other budget terms are negligible or their significance among all budget terms were limited.

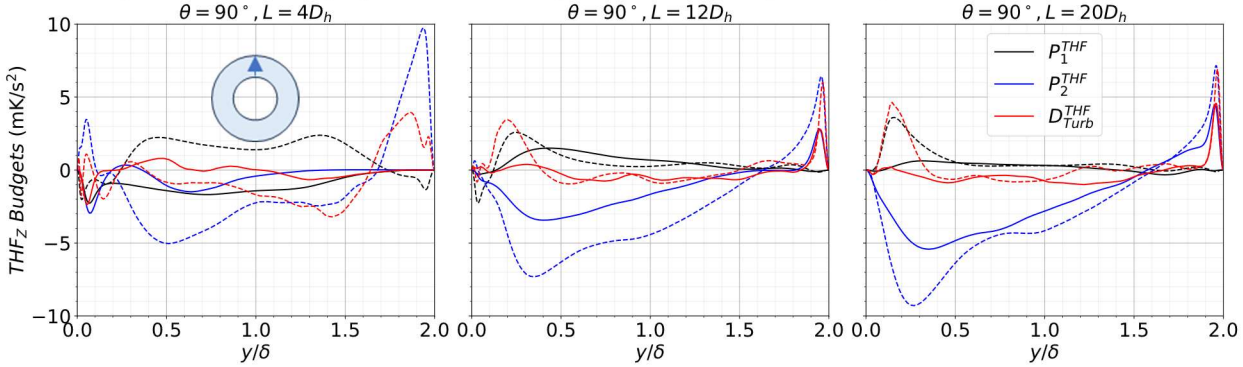

Figure 4.43. Comparison of production 1, production 2, and turbulent diffusion budget terms for the z component of turbulent heat flux transport for angular position $\theta = 90^{\circ}$ along the heated part for cases 2 “645-050-G” (solid line) and 3 “645-100-G” (dashed line).

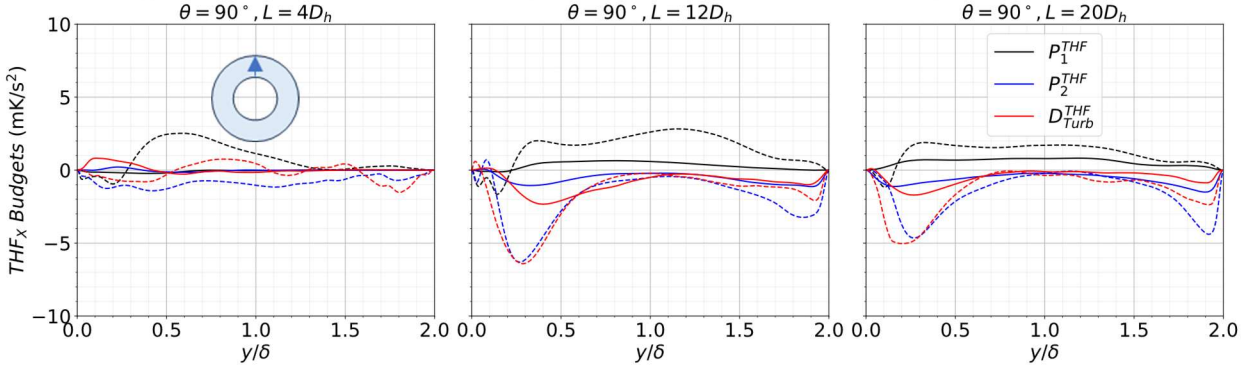

Figure 4.44. Comparison of production 1, production 2, and turbulent diffusion budget terms for the x component of turbulent heat flux transport for angular position $\theta = 90^{\circ}$ along the heated part for cases 2 “645-050-G” (solid line) and 3 “645-100-G” (dashed line).

The x-axis component symbolizes angular direction in the top region. The x-direction turbulent heat flux in the top region is the weakest component compared to the other components. However, effect of the heated flow redevelopment process through heated part is still observable as shown in Fig. 4.44. In top region, x component turbulent heat flux was subject to both the destruction by Production 2 term for and export by turbulent diffusion term. These two budgets reached the highest magnitude where secondary flow paths are merged at the first half of the annular gap. Meantime, production 1 term provides a steady contribution to the flow after stratified layer has crossed. The negative terms indicate that the turbulent heat flux is being destroyed by the two production terms and energy transferred to the bulk flow inside stratified layer. Turbulent diffusion term has exported the remaining part of the balance through core flow region.

The wall-normal component heat flux in the top region had suffered these events in more severe level according to the trend evolution observed in Fig. 4.45. The production 2 term has exhibited its destructive state to y direction turbulent heat flux balance in the first half of the annular gap. The destructive state has turned productive contribution starting from the core flow region.

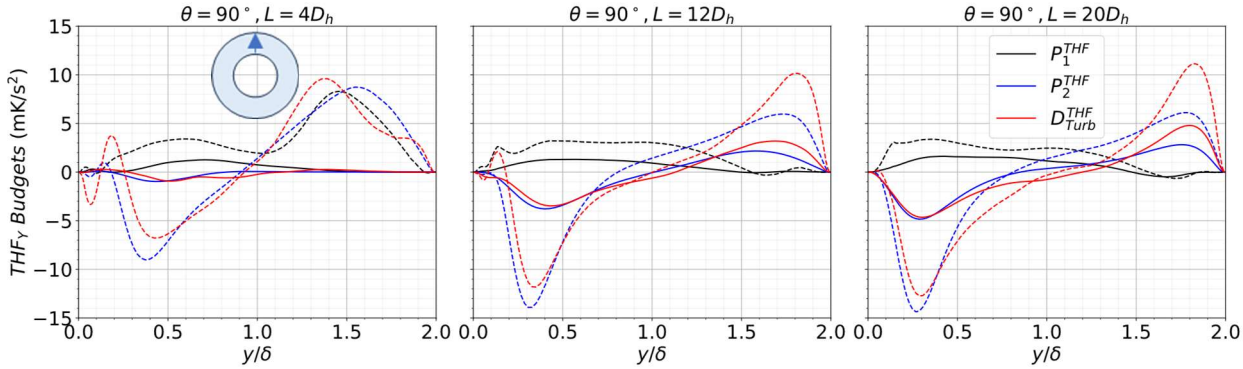

Figure 4.45. Comparison of production 1, production 2, and turbulent diffusion budget terms for the y component of turbulent heat flux transport for $\theta = 90^{\circ}$ along the heated part for cases 2 "645-050-G" (solid line) and 3 "645-100-G" (dashed line).

The direction change in the second half is mainly due to direction change in the bulk velocity gradient. The decreasing local velocity and accumulated heat by the secondary flow imports the turbulent heat flux into the region at the point where heat transfer by temperature gradient is not efficient / noticeably present anymore. Therefore, heat has transferred to the near outer wall by turbulence. The return to the productive state has initiated with the presence of enhanced mixing observed throughout heated part. The production term 1 has continued its positive contribution along the flow depth similar to the other components but was not over-responsive to early trend changes since it has linked to buoyancy of the fluid.

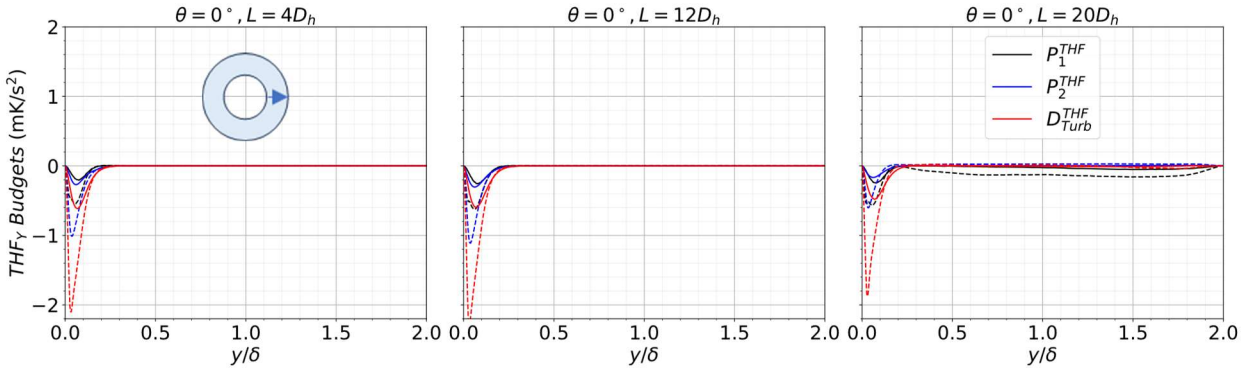

Figure 4.46. Comparison of production 1, production 2 and turbulent diffusion budget terms for y component of turbulent heat flux transport for $\theta = 0^{\circ}$ along heated part for cases 2 "645-050-G" (solid line) and 3 "645-100-G" (dashed line).

Figures 4.46 and 4.47 represent the transport budgets of turbulent heat flux in the angular position of θ=0°. In the side region, cross flow created by heated fluid was travelling upward at the near-heated wall region which altered the turbulent heat flux budgets as well. The turbulent heat flux was being immediately carried away or destroyed Production 1 to the bulk flow. Production 2 has a limited contribution in a noticeably short distance from the inner wall. These events are observed in greater magnitude for case 3 as in the top region. The wall normal component in this location

was not presented as it is negligibly small in magnitude. The bottom region exhibits a similar picture to the side region. Therefore, no further analysis is possible except the effect of the presence of gravity.

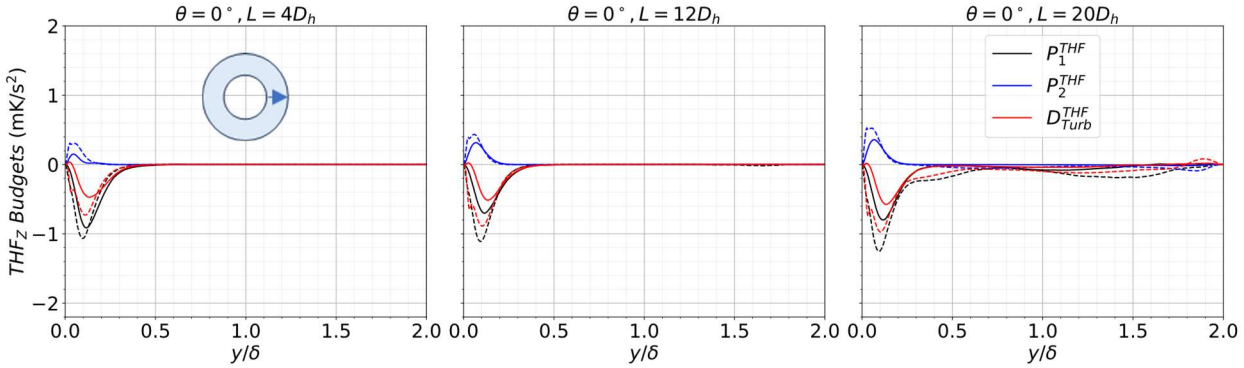

Figure 4.47. Comparison of production 1, production 2, and turbulent diffusion budget terms for z component of turbulent heat flux transport for $\theta = 0^{\circ}$ along the heated part for cases 2 "645-050-G" (solid line) and 3 "645-100-G" (dashed line).

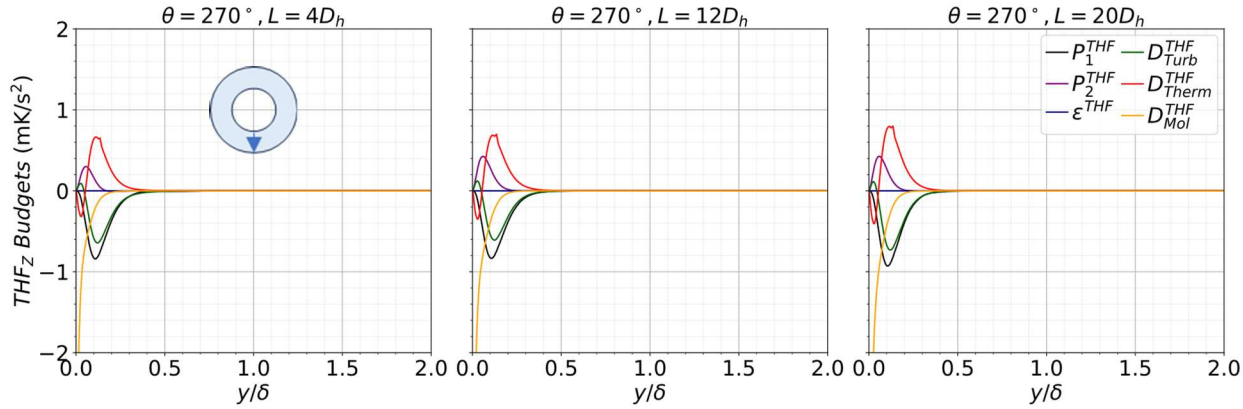

Figure 4.48. Comparison of z direction turbulent heat flux transport budget profiles for angular position $\theta = 270^{\circ}$ along heated part plotted for the case 2 (645-050-G).

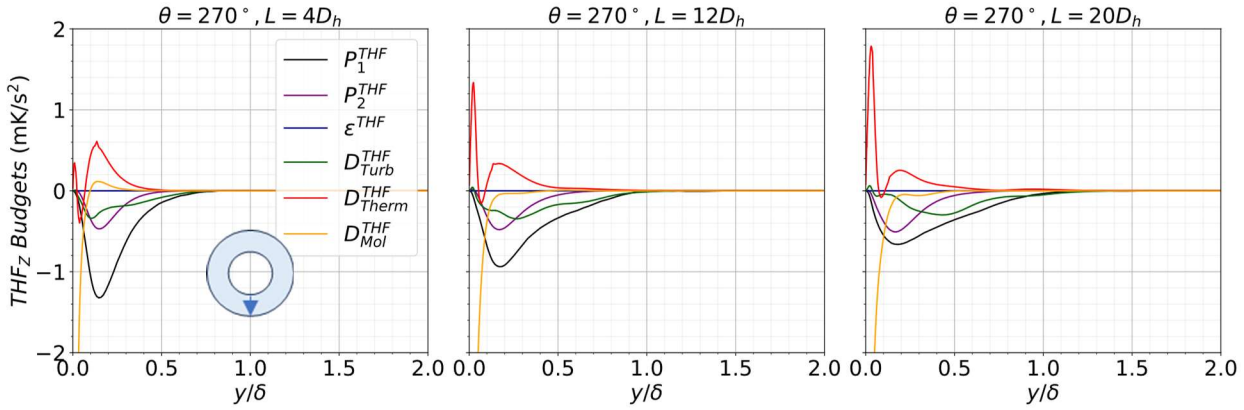

Figure 4.49. Comparison of z direction turbulent heat flux transport budget profiles for angular position $\theta = 270^{\circ}$ along heated part plotted for the case 4 (645-050-N).

In the absence of cooling by cross flow in case 4 (Fig. 4.49) temperature levels develop further both in magnitude and distance in comparison to case 2 (Fig. 4.48). The trend development for

turbulent heat flux budgets in case 4 showed broadening of turbulent heat flux transport near to the centerline of the flow. The production terms were more active with destruction state since they exhibit greater negative contribution. The contribution of the turbulent diffusion mechanism was diminished in comparison to case 2 while still carries turbulent heat flux away from the heated wall. The thermal diffusion term showed an oscillating behavior with initial peak at the close region to heated wall surface, then reached to the local minimum before it stabilizes through core flow region. The oscillation behavior aligns with the location whereas pseudo-critical region being crossed. The loss in the turbulent diffusion was partially compensated by thermal diffusion and production terms working to transfer turbulent heat flux away from the heated wall. However, these mechanisms were not efficient enough to remove heat as turbulence itself. Therefore, damping of the temperature fluctuations by the presence of the wall diminished by the excessive temperature elevation near wall and led to instabilities.

In overall, the transport budgets of the turbulent heat flux bring further understanding to how heat is being transported in addition to the knowledge provided by turbulent heat flux distribution. As heat removal driven by molecular interactions, which is the less efficient mode of transport, overall turbulent heat transfer by turbulence is worsened, especially in case 3. This information aligns with the decreasing heat transfer quality observed in previous subsections. The stratified layer in the top region stands as one of the obstacles to both heat and turbulence transport in this region. The damping of the temperature fluctuations worsened in the case 4 which is reflected to effective mechanisms spotted in the turbulent heat flux transport. The extent of the fluctuating components of temperature and turbulent heat transfer as well became a concern for the distribution of temperature statistics in the solid domain.

4.3.3 Features of conjugate heat transfer

The purpose of the conjugate heat transfer is utilized for this study to utilize the DNS within more realistic boundary conditions rather than idealized iso-flux and iso-thermal boundary conditions. The presence of the wall provides damping for temperature fluctuations as discussed before [44]. However, the detailed profile of the resulting dampening effect still requires further discussion. For this reason, the statistics inside the wall domain are evaluated to investigate available statistics.

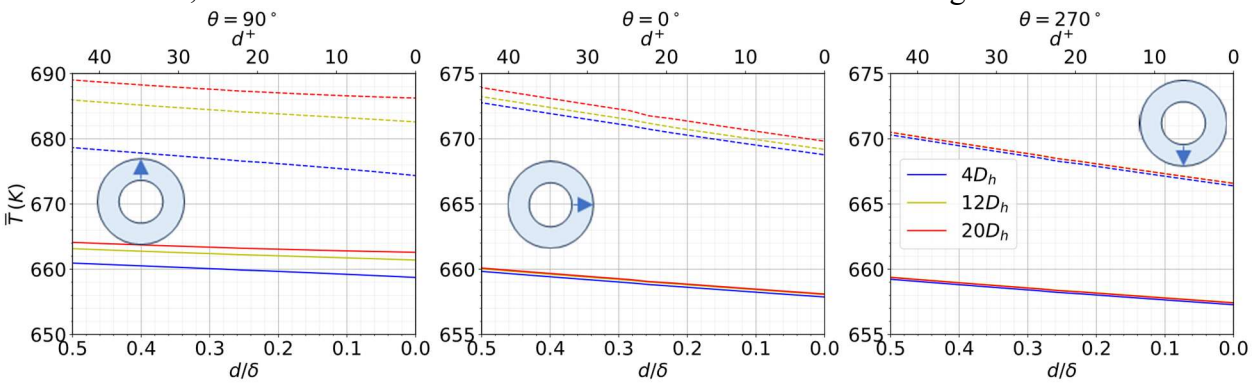

Figure 4.50. Comparison of mean temperature profiles in the solid region for three different angular positions and three different streamwise locations along the heated part for cases 2 “645-050-G” (solid line) and 3 “645-100-G” (dashed line).

In Figure 4.50 the mean temperature profiles across wall thickness were plotted for different angular positions and streamwise locations. The sampling direction is taken normal to the wall surface, starting from the heat flux imposed inner wall to outer wall which is the solid-fluid contact interface. The first x axis (below) values in the plot are set accordingly to the depth from outer wall to inner wall of the solid. The wall normal distance in the solid is denoted by d which normalized by the half thickness of the annular gap with the form d/δ. The second x axis is defined for the dimensionless wall normal distance in the solid d^+ to obtain measure of wall distance over characteristic turbulent quantities similar to the y^+ for the turbulent flows.

The temperature elevation differences observed in the fluid domain temperature statistics were visible in the Fig. 4.50. The differences in the temperature development were more visible in the solid domain statistics for side ($\theta = 0^\circ$) and bottom ($\theta = 270^\circ$) region that shows the effect of the stratified layer causing elevation and asymmetry in the obtained statistics throughout the simulation domain.

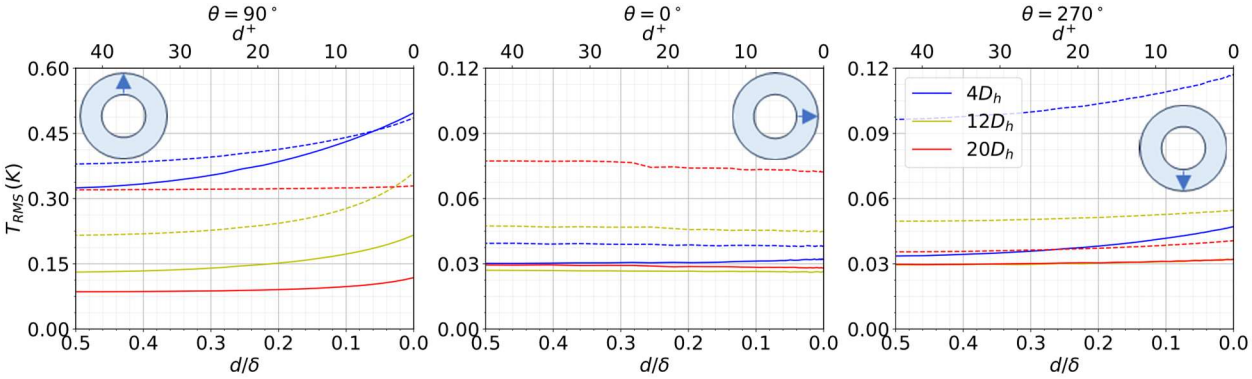

Figure 4.51. Comparison of temperature variance profiles in the solid region for three different angular positions and three different streamwise locations along the heated part for cases 2 “645-050-G” (solid line) and 3 “645-100-G” (dashed line).

In the next step, temperature variance statistics are plotted in Fig. 4.51 for the same locations, respectively. As mentioned in the Chapter 2 that dimensionless wall normal thickness d^+ should be greater than 10 in order to observe the damping effect of the presence of the wall over temperature fluctuations [45], [46]. The wall has depth of d^+=44.69 which exceeds beyond this threshold. The obtained statistics show that damping effect was experienced in various degrees in the wall domain depending on the local events observed in the fluid domain. As discussed before, the increase in the temperature also contributes to the magnitude of the temperature fluctuations. However, observed profiles represented partly different development trends along the heated part. In case 2, temperature variance at the top region exhibited more than two times higher values at the early stages in comparison to end locations. The magnitude is comparable with its case 3 counterpart which can be considered exceptionally higher than usual. This is due to both early rise of the temperature and drastic thermophysical property changes in the pseudo-critical temperature region in the fluid. The simultaneous presence of these two events altered temperature fluctuations at the near wall region (Fig. 4.12-13). In the side region, the exceptionally higher temperature variance can be linked with the elevation observed in the end of heated part for case 3. The other sampled locations showed steady dampened temperature variance development away from the solid-fluid interface and they were tending to stabilize in flow direction within the progress of the heated flow redevelopment.

The inner wall of the solid domain was supplied with uniform heat flux. On the other hand, the temperature profile development did not advance as uniform due to cross flow movements of the heated fluid. Therefore, temperature gradients inside the solid domain for each direction were plotted to observe the anisotropic distribution of uniformly imposed heat flux.

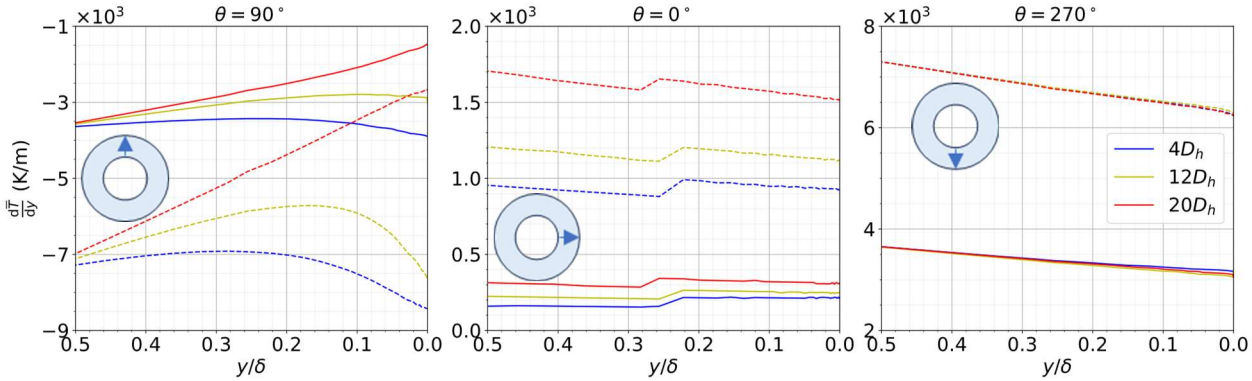

Figure 4.52. Comparison of y direction temperature gradient profiles in the solid region for three different angular positions and three different streamwise locations along the heated part for cases 2 “645-050-G” (solid line) and 3 “645-100-G” (dashed line).

The y direction temperature gradients for three different angular positions along heated part were plotted in Figure 4.52. It is observed that developing thermal field of the turbulent flow affected the distribution of the direction heat flux as well. The buoyancy effect leads to accumulation of hotter fluid at the top region which leads to non-uniform temperature distribution across the path from the top region to the bottom region. In the top region, the wall normal component gradually developed along streamwise direction but the sign of the gradient changes in other locations since they remain colder. The curve trends change as top region distributes heat to the other regions while closing to the solid-fluid interface.

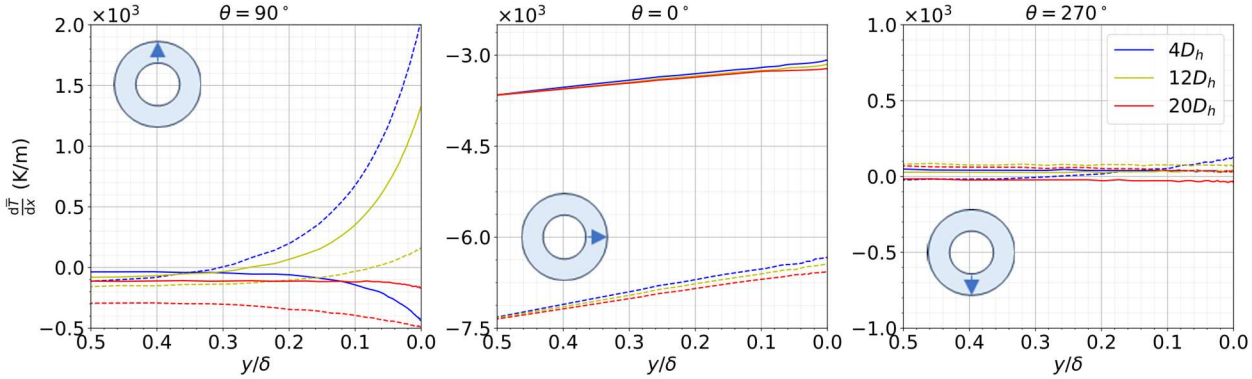

Figure 4.53. Comparison of x direction temperature gradient profiles in the solid region for three different angular positions and three different streamwise locations along the heated part for cases 2 “645-050-G” (solid line) and 3 “645-100-G” (dashed line).

Heat distribution by the top region shifts the heat diffusion to x component as can be seen in Fig. 4.53. The wall normal component of the side region drew a steady curve that separates with the flow progress. The secondary flow is weak in this region which provided very small effect on the temperature gradient. Therefore, the temperature gradient did not significantly change.

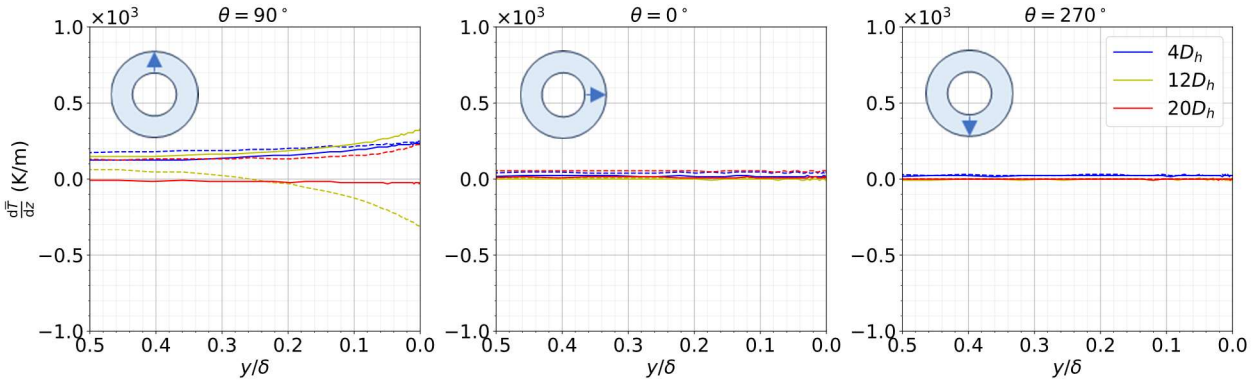

Figure 4.54. Comparison of z direction temperature gradient profiles in the solid region for three different angular positions and three different streamwise locations along the heated part for cases 2 “645-050-G” (solid line) and 3 “645-100-G” (dashed line).

The streamwise component of the temperature gradient (Fig. 4.54) has a negligible contribution except the early locations. In the early locations, streamwise component also receives limited contribution from the wall normal gradient. The horizontal flow of supercritical water in heated annular pipe could not provide uniform cooling due to buoyancy effect in the spanwise directions of the solid domain. The uniformly imposed heat flux could not be preserved as elevated temperatures of the top region leads to redistribution across cross section, especially to the downwards where cooling can be done more effectively.

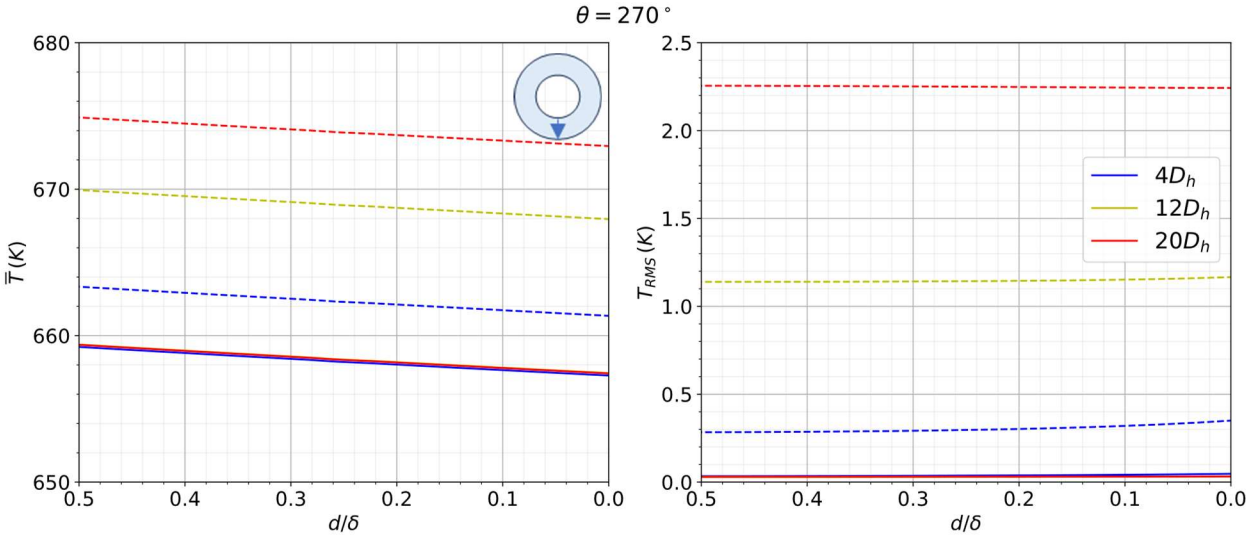

Figure 4.55. Comparison of mean temperature and temperature variance profiles in the solid region for the bottom region ($\theta = 270^{\circ}$) and three different streamwise locations along the heated part for cases 2 “645-050-G” (solid line) and 4 “645-050-N” (dashed line).

Similarly to the previous subsections, the bottom region of case 2 exhibits similar behavior to case 4 where flow development is symmetric in the absence of buoyancy effects. Similar comparison was made observe the effect of the presence of the solid wall. The mean temperature and temperature variance profiles were compared in Fig. 4.55. The mean temperature profiles presented similar trend across solid domain for both cases. The only significant difference observed is that elevated temperature profiles in case 4 showed gradual increase along the heated part within the absence of cooling effect provided by cross flow. Therefore, temperature gradient

profiles were not presented since the behavior in the bottom region of case 2 and case 4 were remarkably similar. Heat flux anisotropy remains primarily in the radial (wall normal) direction in case 4 as well. These similarities were not valid in terms of the temperature variance for case 4 which exhibited very high (more than 10 times) RMS values in comparison to case 2. In Fig. 4.55, the RMS profile of temperature showed negligible changes within the distance from the solid-fluid interface. The only difference between the cases was the removal of gravity that cancels cross flow part of the secondary flow. The significant loss of the cooling mechanism caused very high temperature fluctuations and limited the damping effect of the solid wall. Therefore, effective cooling mechanisms of the buoyant turbulent flow were necessary to reduce thermal strain of the solid material received from temperature fluctuations.

4.3.4 Summary

Statistics regarding the fluctuating component of the temperature and its correlation with the fluctuating velocity for the turbulent heat flux term investigated for the heated flow field. Additionally, temperature statistics for the solid domain analyzed for its response on the secondary flow behavior and its response on the damping effect to the fluctuating temperature component.

The responses of the temperature variance on the secondary flow presented a complex picture, especially on the top region. It was expected that elevated temperature would increase the magnitude of the temperature fluctuations. However, the effect of the buoyancy that pulls heated fluid upwards and following stratified layer altered the temperature variance profile. The plateau formation observed in the momentum statistics were present as well. As stratified layer crossed, further evolution of the temperature variance was visible. This evolution can be addressed to enhanced mixing that appeared as the sole effect in the end locations of heated part side region statistics.

In case of the turbulence heat flux, it is found that the angular component in the top region is negligibly small. The wall normal component is mainly driven by the buoyancy effect that forms relatively stable growth. However, the streamwise component both suffers from the stratification of the fluid duo to streamwise fluctuating velocity component and also steep fall of the temperature profile away from the heated wall. These two separate effects present a unified, variable growth of turbulent heat flux that was amplified by the increased heat flux.

As stratified layer suppresses turbulence, the similar distinction between the first half of the annular gap and the second gap was present for the turbulent heat flux as well. It was observed that heat transport by turbulence suppressed this layer and could not be compensated until the second half. The active diffusion mechanism was turbulent diffusion within the presence of the secondary flow. Cooling of the heated surface was highly dependent on these mechanisms. As gravity removed from the system, turbulent diffusion lost its significance due to loss of cross flow. Thermal diffusion term became dominant for the case 4. However, it was not possible to remove heat efficiently that resulted in the excessive evolution of the temperature statistics.

The uniform heat flux imposed on the inner surface the wall was the sole source of the heating in modeled DNS domain. However, non-uniform presence of the secondary flow led to anisotropic distribution of the temperature gradient across the solid domain. High and variable values of the temperature variance were recorded within the presence of variable temperature gradient across solid thickness. These changes challenged the damping of the temperature fluctuations within the presence of solid wall. Also, temperature variance effected from the elevated temperature profiles in case 4 where solid wall was unable to damp these statistics.

The feature of the solid wall to damp thermal stress is challenged in the case of horizontal buoyant flows where buoyancy induced non uniform secondary flows exist. The capability of this feature is dependent on the temperature levels, effectiveness of the cooling and its uniformity.

5 A priori assessment of RANS turbulence and heat flux closures: Analysis with DNS data

5.1 Theoretical background

The Reynolds Averaged Navier Stokes (RANS) simulations are the least computationally expensive approach that relies on the modeling the Reynolds stresses. The aim is to calculate averaged flow quantities and predict general behavior of the flow domain. It is important to recall the Reynolds decomposition,

$$\phi(t) = \overline{\phi}_i + \phi_i'(t) \tag{2.2}$$

The index i refers to the vector component of the quantity ϕ_i. In this decomposition, a quantity is split into mean and fluctuating components. The continuity equation provided in Eq. 3.20 takes the following form for steady state, compressible flow,

$$\frac{\partial(\overline{\rho u_i})}{\partial x_i} = 0 \tag{5.1}$$

The momentum equation balances the forces acting on the fluid. The infamous closure problem appears here [11],

$$\rho \overline{u}_j \frac{\partial \overline{u}_i}{\partial x_j} = -\frac{\partial P}{\partial x_i} + \rho g_i + \frac{\partial}{\partial x_j}\left(\mu\left(\frac{\partial \overline{u}_i}{\partial x_j} + \frac{\partial \overline{u}_j}{\partial x_i}\right) - \overline{u_i' u_j'}\right) \tag{5.2}$$

The separation of flow quantities as mean and fluctuating parts creates a "closure problem" where the number of unknowns is greater than the number of equations. Several approaches have been developed to overcome the closure problem mainly by treating turbulent stresses with modeling. These approaches are classified as linear eddy viscosity, non-linear eddy viscosity, Reynolds stress transport, and algebraic stress models [84] that offering various approaches on turbulence modeling. Among all of these models, eddy (turbulent) viscosity models are widely used in the current state of the art [85], [86], [87] due to their simplicity and adaptability for wall-bounded

flows under supercritical pressure conditions. Among the turbulent viscosity models, k-epsilon model form is frequently preferred by researchers.

The turbulent viscosity models rely on the Boussinesq' s turbulent viscosity hypothesis [88]. Here, the effective viscosity term is calculated by sum of the laminar viscosity μ and turbulent-viscosity ν_t (eddy-viscosity) term to solve closure problem.

$$\nu_{eff} = \nu + \nu_t \tag{5.3}$$

The hypothesis assumes the turbulent momentum flux (Reynolds stress) is proportional to the mean velocity gradient.

$$-\overline{u_i' u_j'} + \frac{2}{3} k \delta_{ij} = \nu_t \left(\frac{\partial \overline{U}_i}{\partial x_j} + \frac{\partial \overline{U}_j}{\partial x_i} \right) \tag{5.4}$$

The term S_{ij} is the mean strain rate tensor. In this way, turbulent viscosity can be calculated by velocity gradients and turbulent viscosity. Yet, Reynolds stresses are still unknown without information of turbulent viscosity. The turbulent viscosity can be calculated by following formula [89],

$$\nu_t = C_\mu \frac{k^2}{\varepsilon} \tag{5.5}$$

Where C_μ is a model constant set to be 0.09. k and ε refers to turbulent kinetic energy and turbulent dissipation rate. This approach has been refined and developed over time as different models proposed based on the core k-epsilon model. A damping function is included to the model function to improve predictions in the near wall-region, especially for low Reynolds number flows.

$$\nu_t = C_\mu f_\mu \frac{k^2}{\varepsilon} \tag{5.6}$$

Several models have been tested and evaluated under supercritical pressure conditions with different flow orientations such as vertical [90] and horizontal [91], [92]. Yet, there is no consensus reached, since prediction performance of these models varies depending on mass flux, buoyancy relevance, heat flux parameters which makes it challenging to conclude on single model. Therefore, most of these models do not consider turbulent anisotropy, which may affect prediction quality. Two models are selected for this purpose to observe potential differences that might occur under highly anisotropic flow conditions. The Chien k-epsilon (Chien) model has been selected as one of the well performing isotropic models in supercritical flows. Reynolds stresses for Chien model are calculated using the same equation provided for standard k-epsilon model (Eq. 5.4). The damping function defined for the Chien model used to calculate turbulent viscosity term,

$$f_\mu = 1 - e^{-0.0115 y^+} \tag{5.7}$$

As a counterpart, Lien k-epsilon (Lien) model is selected as an anisotropic model to be included for further analysis [93], [94]. The Lien model also uses Eq. 5.4 for the same procedure with much more complex form of tensor operations,

$$-\overline{u_i'u_j'} + \frac{2}{3}k\delta_{ij} = 2\nu_t S_{ij} + \nu_t \frac{k}{\varepsilon}(S_1 + S_2 + S_3) \tag{5.8}$$

$$S_1 = C_1\left[S_{ik}S_{kj} - \frac{1}{3}\delta_{ij}S_{kl}S_{kl}\right] \tag{5.9}$$

$$S_2 = C_2\left[\omega_{ik}S_{kj} + \omega_{jk}S_{ki}\right] \tag{5.10}$$

$$S_3 = C_3\left[\omega_{ik}\omega_{jk} - \frac{1}{3}\delta_{ij}\omega_{kl}\omega_{kl}\right] \tag{5.11}$$

S_{ij} and ω_{ij} are strain rate and rotation tensors given in Eq 5.12 and 5.23,

$$S_{ij} = \frac{1}{2}\left(\frac{\partial \overline{U}_i}{\partial x_j} + \frac{\partial \overline{U}_j}{\partial x_i}\right) \tag{5.12}$$

$$\omega_{ij} = \frac{1}{2}\left(\frac{\partial \overline{U}_i}{\partial x_j} - \frac{\partial \overline{U}_j}{\partial x_i}\right) \tag{5.13}$$

Indices introduced in the Eqs. 5.12-5.13 appear in various forms that represent different mathematical operations. The i and j indices (free indices) denote the components of resulting second order tensors like forms $S_{ik}S_{kj}$ and $\omega_{ik}S_{kj}$. The operation $\omega_{kl}\omega_{kl}$ that uses k and l results in a scalar (no free indices) value. Any available indices k and l elements are summed over again for tensor operation which is known as "Einstein notation" [95]. C terms appearing in the S denoted terms are dynamic values dependent on the strain rate and rotation tensors [93]. The equation for the turbulent viscosity still follows the form of Eq. 5.6. C_μ and f_μ terms are given below,

$$C_\mu = \frac{0.667}{1.25 + \frac{k}{\varepsilon}\left(\sqrt{\frac{1}{2}S_{ij}S_{ij}} + 0.9\sqrt{\frac{1}{2}\omega_{ij}\omega_{ij}}\right)} \tag{5.14}$$

$$f_\mu = \left(1 - e^{-0.0198y\sqrt{k}/\nu}\right)\left(1 + \frac{5.29}{y\sqrt{k}/\nu}\right) \tag{5.15}$$

Since Reynolds stresses are modeled, the turbulent kinetic energy and the turbulent dissipation rate are calculated using their respective transport equations. The transport equation for turbulent kinetic energy for the k-epsilon model with buoyancy production budget [96] is given below,

The transport equation for turbulent kinetic energy,

$$\frac{\partial k}{\partial t} + \frac{\partial(\overline{u_i}k)}{\partial x_i} = \underbrace{\upsilon\frac{\partial^2 k}{\partial x_j^2}}_{D_{Mol}^{TKE}} + \underbrace{\frac{\partial}{\partial x_i}\left(\frac{\nu_t}{\sigma_k}\frac{\partial k}{\partial x_i}\right)}_{D_{Turb}^{TKE}} - \underbrace{\overline{u_i'u_j'}\frac{\partial \overline{U_i}}{\partial x_j}}_{P^{TKE}} - \underbrace{B_{model}}_{B_{model}^{TKE}} - \underbrace{\upsilon\overline{\frac{\partial u_i'}{\partial x_j}\frac{\partial u_i'}{\partial x_j}}}_{\varepsilon^{TKE}} \tag{5.16}$$

The transport equation for turbulent kinetic energy is similar to the one presented for the DNS study in Eq. 3.25. The turbulent diffusion budget term for the turbulent kinetic energy transport without further modeling is given in Eq. 5.17.

$$D_{Turb}^{TKE\text{-}DNS} = -\frac{1}{2}\frac{\partial \overline{u_j' u_j' u_i'}}{\partial x_i} \tag{5.17}$$

The closure problem introduces differences in the turbulent diffusion budget term of the turbulent kinetic energy transport that require further investigation. In RANS modeling, the modeled turbulent diffusion budget terms take the form in Eq. 5.18.

$$D_{Turb}^{TKE\text{-}model} = \frac{\partial}{\partial x_i}\left(\frac{\nu_t}{\sigma_k}\frac{\partial k}{\partial x_i}\right) \tag{5.18}$$

The turbulent diffusion term was the most dominant diffusion mechanism throughout the heated part according to results provided in chapter 4. The other difference is due to the buoyancy contribution term since only averaged flow quantities are available, turbulent heat flux is not calculated directly in RANS simulations. Therefore, the turbulent heat flux term in the buoyancy production budget in Eq. 5.18 is modeled.

$$B_{model}^{TKE} = -\beta g_i \left(\overline{u_i' T'}\right)_{model} \tag{5.18}$$

There are three approaches emphasized in the current state of the art which are called as "simple-gradient diffusion hypothesis" (SGDH), "generalized gradient diffusion hypothesis" (GGDH) and "algebraic flux models" (AFM) [97]. The SGDH is the simplest and most practical, with a form similar to the turbulent viscosity hypothesis,

$$\overline{u_i' T'}_{SGDH} = -\frac{\nu_t}{Pr_t}\frac{\partial T}{\partial x_i} \tag{5.19}$$

Pr_t denotes the turbulent Prandtl number set for the given flow conditions. Initial preference in the literature was to set turbulent Prandtl number as a constant [98]. However, a constant Prandtl number can lead to poor predictions at the flow conditions where buoyancy is considered. For supercritical flows, strong thermophysical property variations also challenge the prediction quality. The constant values of 0.85 (sCO_2) and 0.9 (sH_2O) have not been found adequate enough [99]. Several approaches have been presented to better assess the turbulent Prandtl number to be competent against rapid changes in the supercritical flows [100], [101]. Unfortunately, there are very few studies on the horizontal flows under supercritical pressure conditions, and fewer with supercritical water as working fluid focusing on the improvement of turbulent heat flux prediction. Most of the developed correlations on this topic refer to vertical flows.

GGDH draws a bit more complex structure as it includes Reynolds stress. Stress information also carries turbulent anisotropy information into the calculation of turbulent heat flux.

$$\overline{u_i'T'}_{GGDH} = C_\theta \frac{k}{\varepsilon}\left(-\overline{u_i'u_j'}\frac{\partial T}{\partial x_j}\right) \tag{5.20}$$

The coefficient C_θ has been selected as 0.3 in previous studies under supercritical pressure conditions [86]. However, there is no definitive criterion for this constant. There are various AFM for turbulent heat flux prediction and higher order models are presented to improve GGDH and overcome its weaknesses [102]. These models are not mentioned here as they are not widely covered by the literature yet.

In this chapter, the prediction capabilities of two different RANS models (closures) and two different turbulent heat flux models are assessed by a priori analysis for their prediction capabilities upon DNS data produced and presented in chapter 4. The selection is made regarding the turbulent anisotropy awareness of the models. The determined models are Chien (isotropic), and Lien (anisotropic) model for RANS closures. Other two models selected for turbulent heat flux prediction are SGDH and GGDH. The SGDH model is considered due to its simplicity and reliance on the model functions considering turbulent viscosity and turbulent Prandtl number. GGDH is selected to observe the contribution of turbulent anisotropy information on turbulent heat flux prediction. The procedure for the a priori analysis method is explained in the section 5.2.

5.2 Methodology: A priori assessment

The RANS closures and turbulent flux models mentioned in this chapter have been put into priori assessment by feeding them with DNS data presented in chapter 4. In this way, the prediction performance of modeling and general behavior of closures were tested without the need of solving actual RANS simulations [103], [104]. This method isolates the model from the information loss due to low-grid resolution and numerical errors by using model generated mean flow data by RANS simulation.

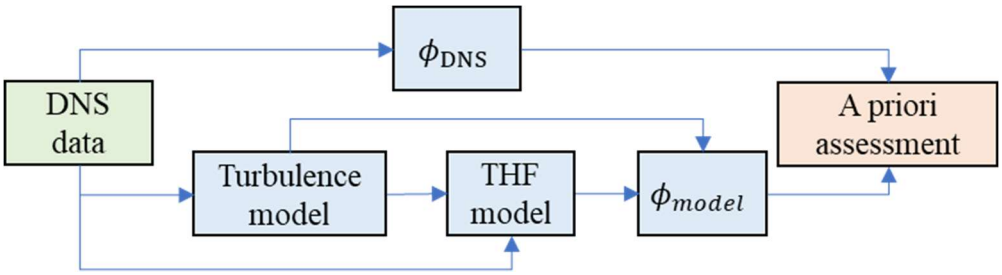

Figure 5.1. The flow chart for the priori assessment method for elaborated models.

The a priori test procedure shown in Figure 5.1 does not generate reference results as DNS does but gives an insight how models fare in comparison to reference DNS results which were noted to be highly anisotropic. The complete RANS simulation results from the given models are expected to be differ than a priori assessment results but their overall behavior are reflected to the assessment results. The key idea is to feed the selected models with unfiltered DNS mean flow data to observe their response and investigate them further if there is room for improvement.

The procedure initiated with the recalculation of Reynolds stress tensor by model equations given by Eq. 5.4 and 5.8. DNS mean flow quantities and turbulence data were used in these equations to calculate a priori turbulent viscosity and Reynolds stresses for the inflow region. Later, turbulent diffusion and production budgets of the turbulent kinetic energy transport were recalculated for comparison with budgets terms originally calculated by DNS. The same procedure was repeated for the heated part. In heated part, additional effort was put into the buoyancy budget term by investigating turbulent heat flux models with the same methodology to investigate their capability to predict turbulent heat flux. In further analysis, following topics were discussed by considering the top (most complex) region of DNS results presented for the effect of heat flux:

- The need for a dynamic turbulent Prandtl number function instead of a constant value by provided flow conditions.
- The possibility on the increasing awareness of the GGDH model to the provided flow conditions.

Reporting of results and further investigations regarding a priori analysis are presented in section 5.3.

5.3 Results

A priori assessment of the selected closures presented in this part with their reference results obtained from DNS data. In the first step, Reynolds stress, turbulent viscosity parameters were calculated. Later, production and turbulent diffusion budgets of turbulent kinetic energy transport investigated in the scope of the a priori analysis. In the second step, these quantities calculated for the heated part to observe the response of the closures under highly anisotropic, horizontal flows under supercritical pressure conditions. Turbulent heat flux closures were also included into a priori assessment procedure for the heated part.

5.3.1 Momentum statistics

In the first step, Reynolds stresses for selected RANS closures have been recalculated for the inflow part. First, the results of the a priori analysis for the inflow part are compared with the DNS statistics for cases number 2 (645-050-G). RANS models are labeled as “RANS – CH” for the Chien model and “RANS – LIEN” for the Lien model. It was observed that all principal stresses calculated almost identical with small discrepancies. Loss of anisotropy information in the recorded stress data even though provided dataset is highly anisotropic. The anisotropy information was omitted by the dominance of the isotropic part of the turbulent stresses. Due to the loss or insensitivity of the anisotropic state of the flow, the streamwise stress component was underpredicted and other components were overpredicted in the a priori analysis that is shown in Fig. 5.2.

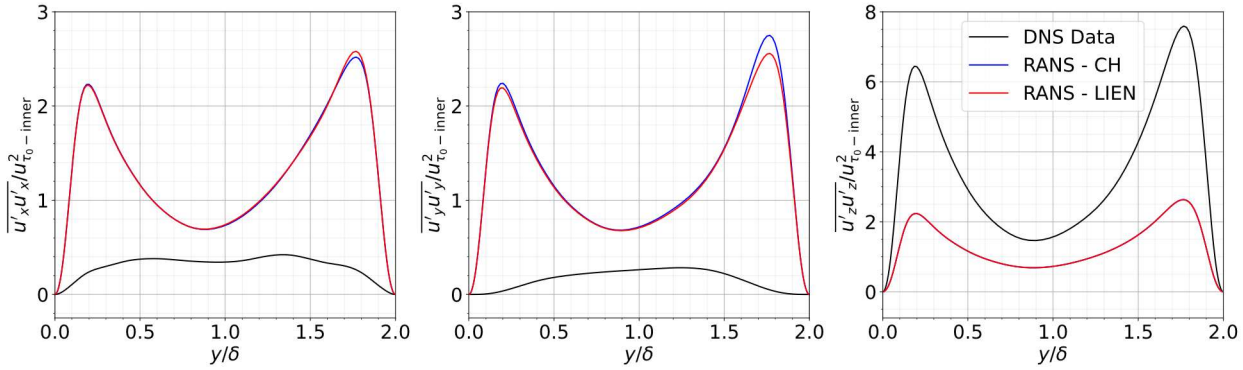

Figure 5.2. Comparison of major components of Reynolds stress tensor profiles calculated for the a priori assessment in comparison to DNS statistics for inflow part.

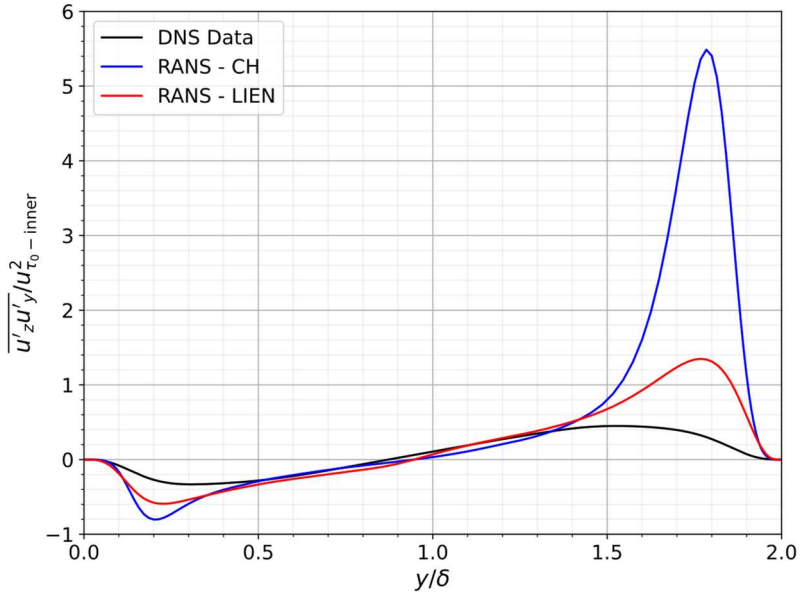

Figure 5.3. Comparison of wall-normal and streamwise direction correlation Reynolds stress component profiles calculated for the a priori assessment in comparison with DNS statistics for the inflow part.

On the other hand, the shear component with a streamwise –wall normal direction correlations drew a different picture (Fig. 5.3) in the a priori analysis. The anisotropic model provided far better prediction performance at the near wall regions. The difference was caused by the isotropic term contains turbulent kinetic energy parameter in the recalculation of Reynolds stress components poses dominance over other components in the Eq. 5.4. Therefore, the principal components of the Reynolds stress were dominated by the isotropic term in the both of the selected models. However, other components of the Reynolds stress do not have this term. The Lien model also deals with the rotation rate tensor in addition to the strain rate tensor. The rotation rate tensor mathematically describes the deformation behavior of a turbulent structure which provides a positive contribution on the prediction of non-principal components. The formulation of the Boussinesq approximation on the turbulent viscosity [105] provides the following mathematical definition,

This approximation works well for cases where turbulence eventually manages to return to anisotropy. The DNS results presented here posed attributes such as strong anisotropy, secondary

flow mechanisms, strong property changes, and wall curvature, which the linear relationship in between stress and strain rate is challenged (Eq. 5.4). Turbulent viscosity is relevant in the viscous sublayer and buffer zone regions within this formulation since the components of the Eq. 5.21 result in an unphysical representation of the turbulent viscosity as the velocity gradient component given in formula crosses zero point (Fig 5.4) at the same location.

$$\nu_t = -\frac{\overline{u_z' u_y'}}{d\overline{U}_z/dy} \tag{5.21}$$

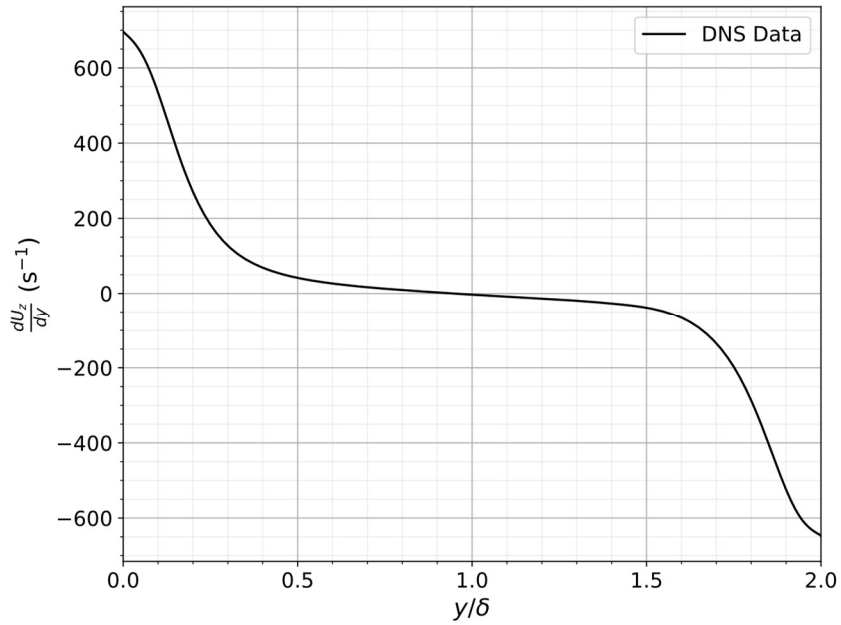

Figure 5.4. The streamwise velocity wall normal gradient profile for the inflow part.

Even though the Eq. 5.21 fails at the core region due to ill-conditioning of the parameters involved, which streamwise velocity gradient approaches to zero and changes its sign that makes turbulent viscosity term highly sensitive to small changes in the resolved shear stress. This can lead to non-physical turbulent viscosity values. However, it is still a valuable parameter to describe momentum transfer by the turbulent interactions. Its importance is also bound with the RANS closures as it directly involved in the calculation of modeled quantities such as Reynolds stresses, turbulent diffusion budget of turbulent kinetic energy transport and turbulent heat flux of SGDH model. A priori assessment of turbulent viscosity performed for the near wall region including the area where $y^+ < 30$ to assess the prediction capabilities of selected RANS closures against the results from Eq. 5.21 calculated from DNS data. The comparison is shown in the Fig. 5.5 including both inner wall and outer wall.

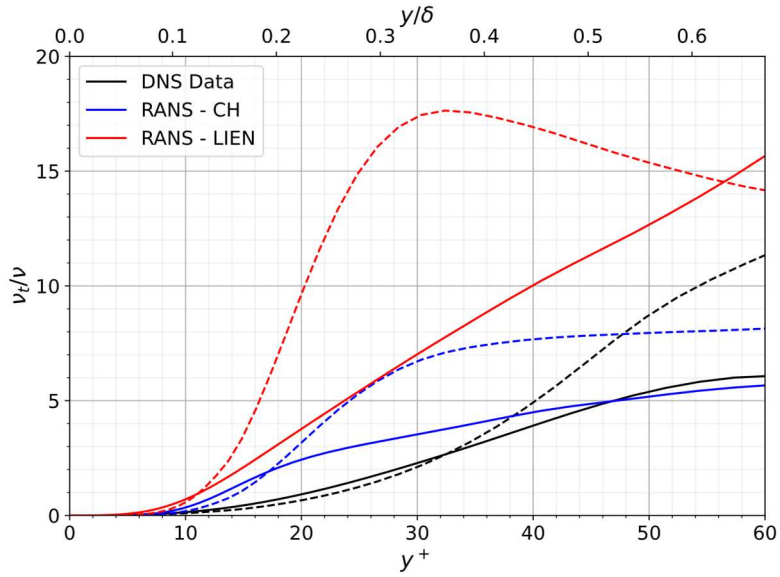

Figure 5.5. Turbulent viscosity profiles calculated from DNS data and the a priori analysis of RANS models. Solid line: Wall distance from the inner wall, dashed line: Wall distance from the outer wall.

The turbulent viscosity develops to greater values at the near outer wall by the effect of curvature. Higher development correlates with the turbulent kinetic energy profile. The discrepancies observed in the a priori analysis results were mainly caused by the discrepancies in the damping functions provided in the investigated models. The Chien model presented better a priori assessment results than the Lien model on the prediction of turbulent viscosity.

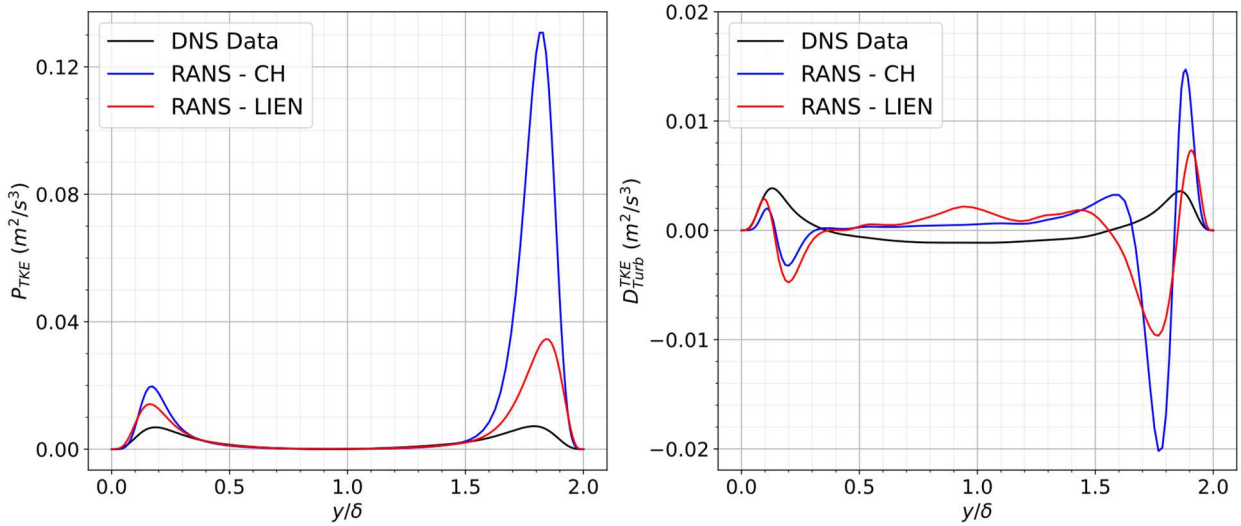

Figure 5.6. Production and turbulent diffusion budgets of turbulent kinetic energy calculated from DNS data and the a priori analysis of RANS models.

The prediction performance of tested models in the a priori analysis showed different evolution on the turbulent kinetic energy production and turbulent diffusion budget terms (Fig. 5.6). Lien model presented far better prediction performance by taking anisotropy information into account sourced from DNS data. However, such a difference could not be seen in the a priori assessment of

principal Reynolds stresses. Overprediction of turbulent diffusion budget term was the reflection of the turbulent viscosity profile calculated during the a priori analysis. Also, the simple gradient diffusion theory used to calculate the turbulent diffusion budget that cannot capture the near wall behavior completely as in the DNS results. This is one of the tradeoffs being made to use simple models for predicting turbulent flow behavior.

A priori assessment regarding the inflow part presented the prediction capability of RANS closures within provided DNS data. Discrepancies observed were connected to the structure of the closures as flow was not subjected to strong local changes. The same procedure applied to the heated part where flow domain was under simultaneous effects by buoyancy, stratification, enhanced mixing laminarization, and thermal acceleration of the flow.

Three principal stresses were plotted for early stages in Fig. 5.7 with the a priori assessment methodology of RANS models. The a priori testing was successful in predicting general behavior of stress component profiles obtained from DNS results. The underprediction of the streamwise component and overprediction of the other two principal components persisted at the early stage of the heated part. Yet, this picture has changed for the case with higher heating where the a priori tested models started to overpredict the reference especially at the second half of the annular gap while closing to outer wall. The stratification of the fluid at the near heated wall could not be predicted well as stratification intensifies with increased heating. In general, the a priori test results were able to follow general trend with identified discrepancies with respect to the reference data. The emergence of the buoyant movement, and stratified layer were the main causes of these discrepancies.

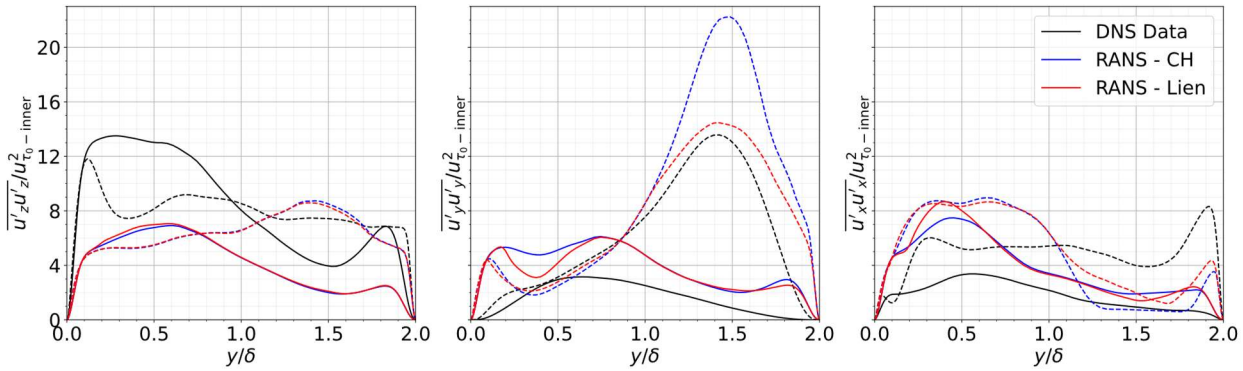

Figure 5.7. Comparison of major components of Reynolds stress tensor profiles calculated for the a priori assessment with DNS statistics at $4D_h$ location in the heated part for cases 2 “645-050-G” (solid line) and 3 “645-100-G” (dashed line).

The oscillating behavior at the near heated wall region appeared at the a priori assessment results presented in Fig 5.8 as well. However, predicted results from the case 2 data were fairly well predicted at the buffer and core flow region. Prediction performance has worsened by the increased heat flux. It was evident that increased heating challenged the a priori test result that prediction curves did not follow the trend evolution in case 3 results.

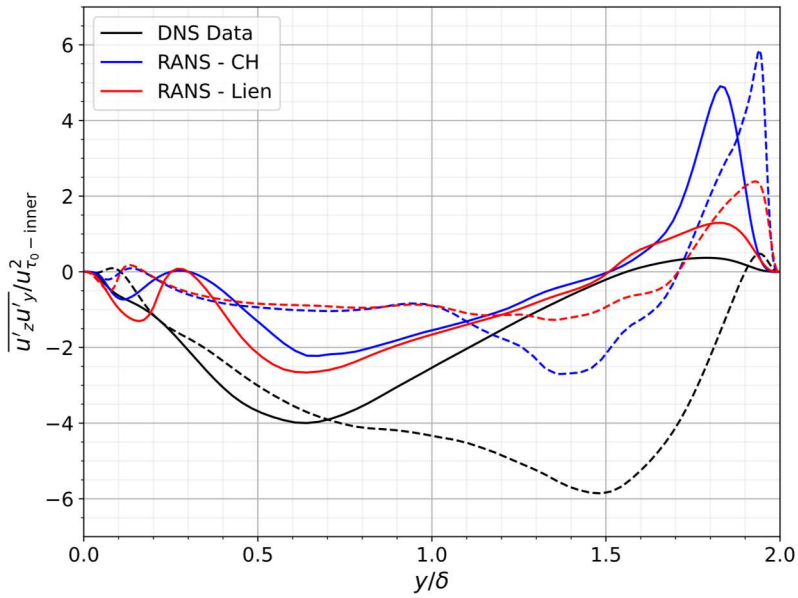

Figure 5.8. Comparison of wall-normal and streamwise direction correlation with Reynolds stress component profiles calculated for the a priori assessment with DNS statistics at $4D_h$ location in heated part for cases 2 "645-050-G" (solid line) and 3 "645-100-G" (dashed line).

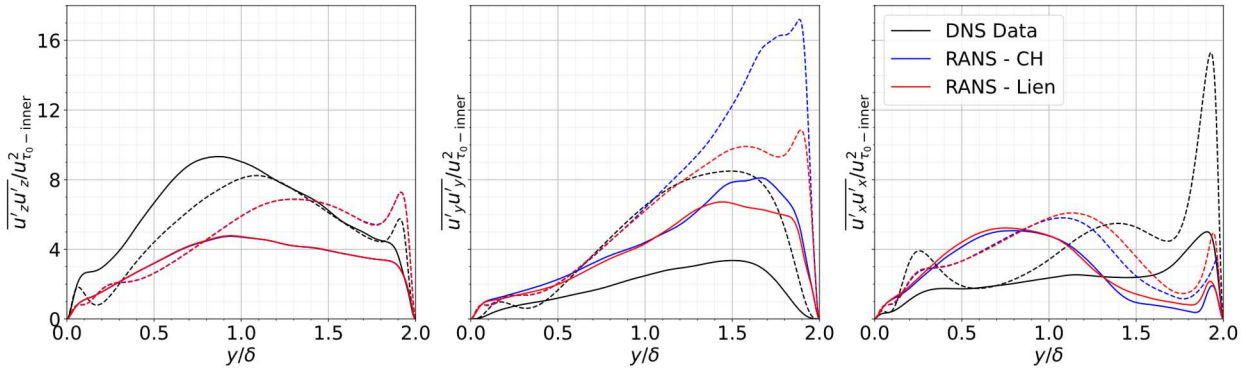

Figure 5.9. Comparison of major components of Reynolds stress tensor profiles calculated for the a priori assessment with DNS statistics at $12D_h$ location in the heated part for cases 2 "645-050-G" (solid line) and 3 "645-100-G" (dashed line).

Despite the clear discrepancies in magnitude of the a priori assessment results and reference DNS results, the predicted results were able to follow the trend evolution at middle stages of the heated part. These trend tracking capabilities were not effective in the near outer wall region where enhanced mixing is observed. The streamwise component profiles shown in Fig. 5.9 were able to follow the physical behavior. However, wall-normal and angular components showed significant breakouts in this region. These differences reached up to four times the reference data. Lien model performs fairly better by capturing trend changes in case 3 with higher heat flux. Yet, both models performed similar predictions for the case 2. The shear component predictions (Fig. 5.10) were not successful for the same locations.

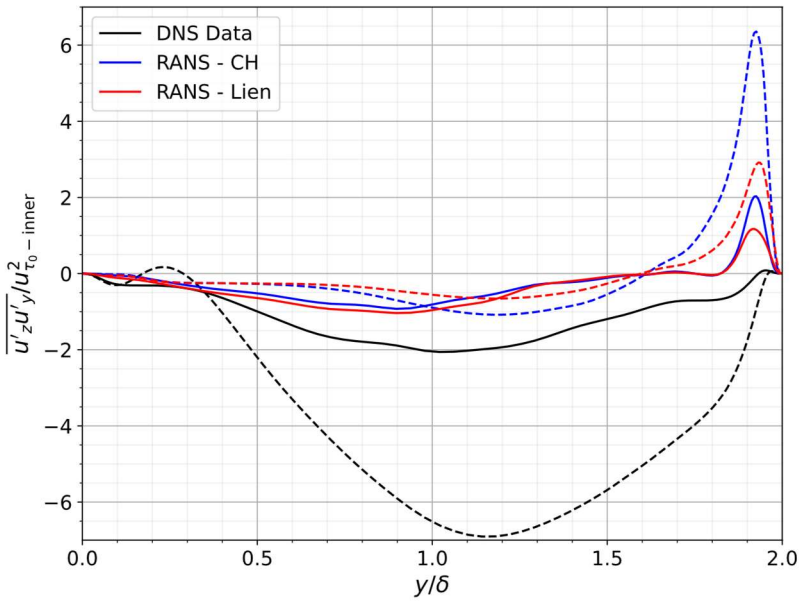

Figure 5.10. Comparison of wall-normal and streamwise direction correlation Reynolds stress component profiles calculated for the a priori assessment in comparison to DNS statistics at $12D_h$ location in heated part for cases 2 "645-050-G" (solid line) and 3 "645-100-G" (dashed line).

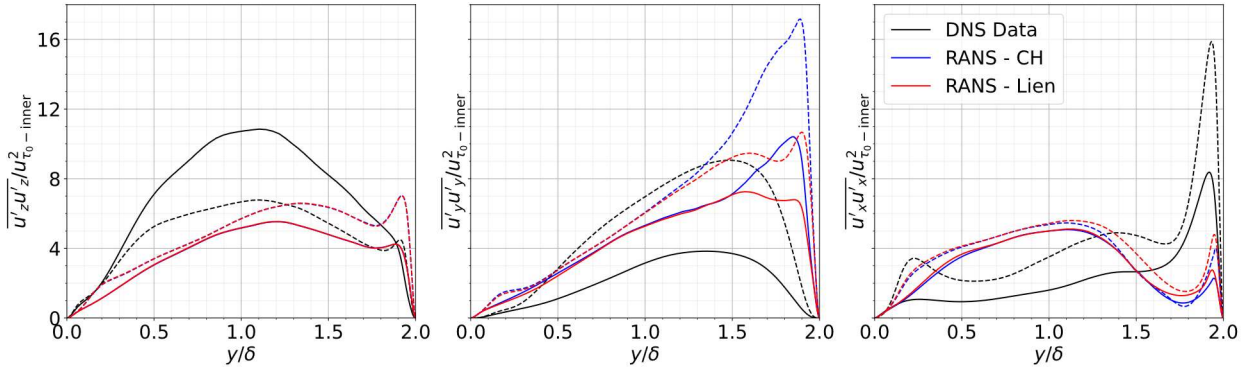

Figure 5.11. Comparison of major components of Reynolds stress tensor profiles calculated for the a priori assessment with DNS statistics at $20D_h$ location in the heated part for cases 2 "645-050-G" (solid line) and 3 "645-100-G" (dashed line).

There is no further improvement observed in predicting redeveloped heated turbulent flow regime since the Reynolds stress profiles did not significantly change between $12D_h$ and $20D_h$ locations. The same situation persists on the principal stress components in Fig. 5.11, which could not be predicted by the trend as well. It has become certain that selected models are not able to perform reasonably well predictions on the secondary flow events like stratification of fluid and enhanced mixing even though flow is not under rapid, radical changes. It is evident that selected models require further modifications to be able to follow secondary flow events in horizontally oriented supercritical flows. In overall, the Lien model performed better in the a priori assessment on the Reynolds stress data as it has caught general trend fairly better in comparison to the Chien model. The observed differences highlight the importance of anisotropic components included in the model. The production and turbulent diffusion budgets are calculated for further insight.

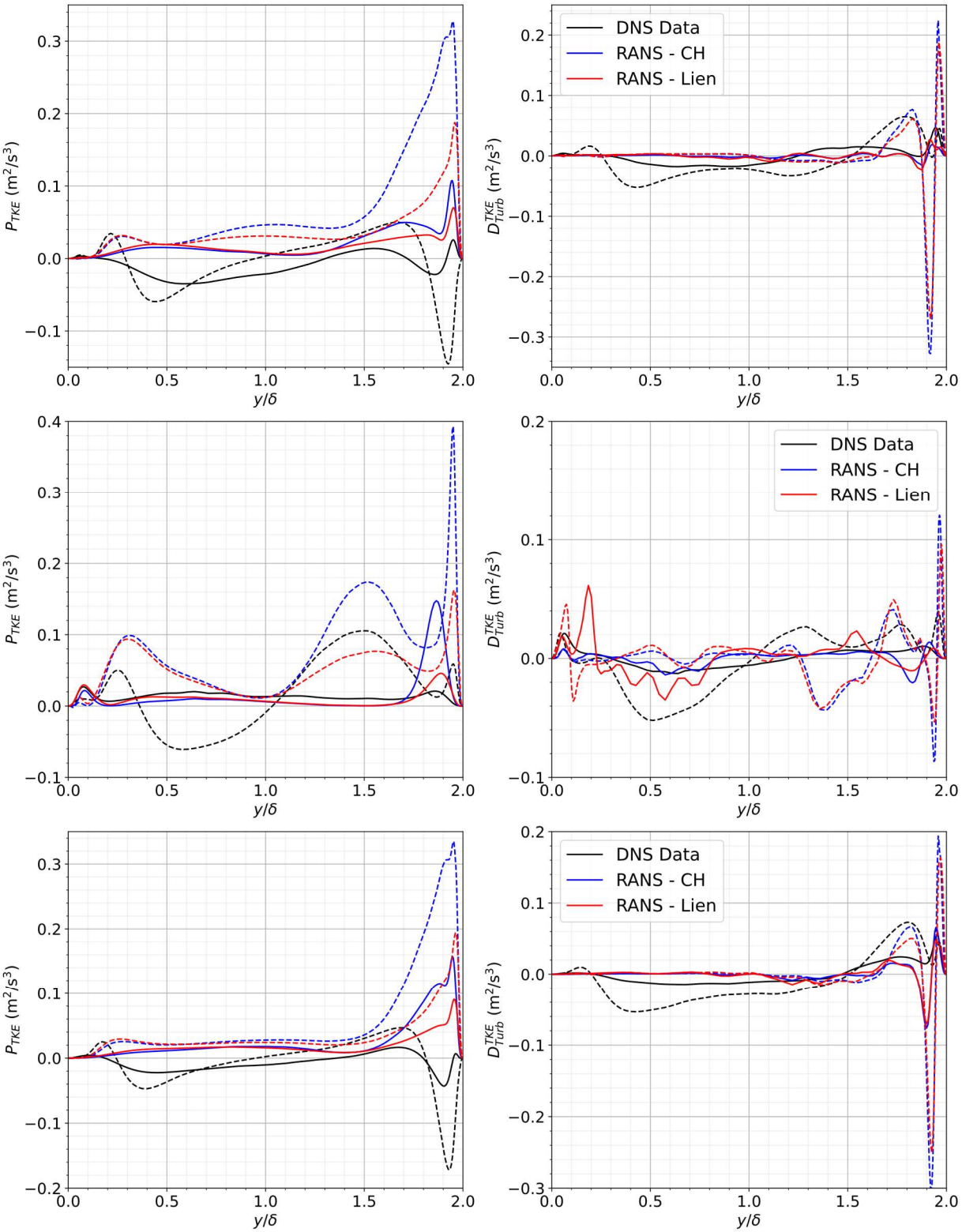

Figure 5.12. Production (left) and turbulent diffusion (right) budgets of turbulent kinetic energy calculated for the a priori assessment with DNS statistics at $4D_h$ (top), $12D_h$ (middle), $20D_h$ (bottom) locations in heated part for cases 2 “645-050-G” (solid line) and 3 “645-100-G” (dashed line).

In Fig 5.12, production (left), and turbulent diffusion (right) budgets of turbulent kinetic energy for the a priori test was plotted on the same locations with their respective budgets obtained from DNS. It was observed that the negative production or destruction of turbulent structures could not be identified by the a priori test results. Both models failed to predict these events as they reflected it as a positive production within similar absolute values. Prediction of physical phenomena breaks out more significantly under the higher heat flux. The breaking location indicates the area where flow behavior changes from the stratified layer to bulk flow. As previous findings on the a priori tests for the Reynolds stresses considered, the separation in the cross-flow prediction has led to collapse in the prediction on the destruction state of the production budget. On the other hand, the turbulent diffusion mechanism prediction was extremely poor or failed since the prediction by turbulent viscosity models and turbulent kinetic energy gradient which were not sufficient enough.

5.3.2 Turbulent heat flux statistics

The prediction of the buoyancy budget term of the turbulent kinetic energy transport directly connected to how correlation of velocity-temperature fluctuations is modeled (Eq. 5.18). In this section, a priori assessment continued with the SGDH and the GGDH modeling approaches to predict turbulent heat flux. Both models include the temperature gradient to predict turbulent heat flux aided by the modeling function provided. SGDH includes the ratio of turbulent viscosity and turbulent Prandtl number (Eq. 5.19) that both were modeled. GGDH hypothesis includes the tensor multiplication of Reynolds stresses and temperature gradient (Eq. 5.20). Results of the a priori assessment performed with their respective DNS results to assess their prediction capability.

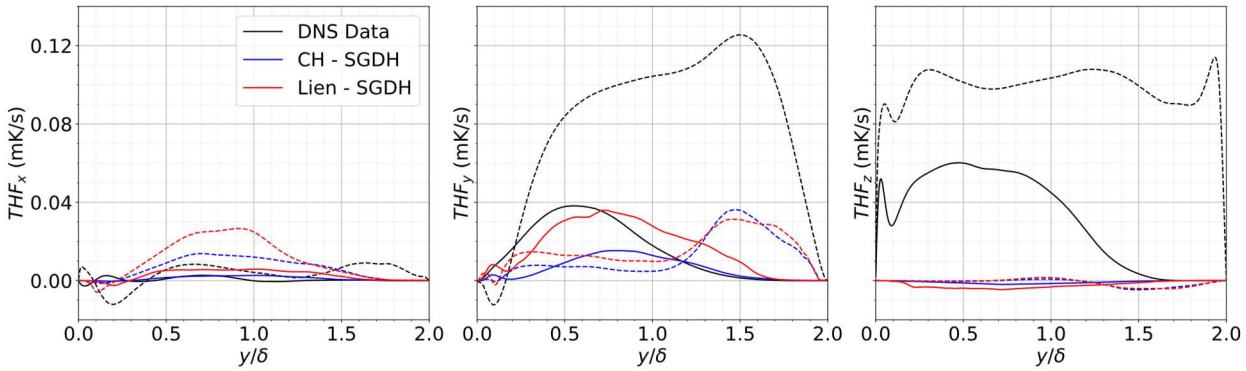

Figure 5.13. The components of turbulent heat flux profiles for the a priori assessment with SGDH compared with DNS statistics at $4D_h$ location in heated part for cases 2 “645-050-G” (solid line) and 3 “645-100-G” (dashed line).

SGDH hypothesis relies on vectoral components of the temperature gradient for general evaluation. A priori assessment results for SGDH model shown in Figures 5.13-15 along with the tested RANS closures for the heated part. In the early stages, the temperature gradient made it possible to follow profile development of turbulent heat flux on the wall normal direction for case 2. However, the prediction performance for other directions and also wall normal direction for case 3 were poor. In particular, the discrepancy was too high in the streamwise direction to consider the model approach reasonable. The cause of the poor prediction performance has two parts:

Modeling applied on the turbulent viscosity and the turbulent Prandtl number is one part that can be evaluated. Another part is the use of temperature gradient that follows steep decline within the wall distance. Also, the streamwise temperature gradient is exceedingly small in comparison to the wall normal temperature gradient. These possibilities were investigated in detail in following sub-sections.

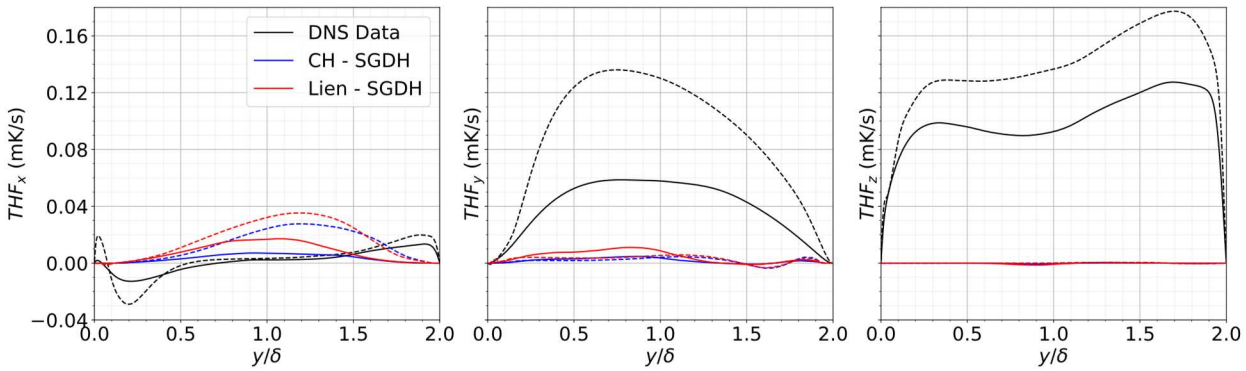

Figure 5.14. The components of turbulent heat flux profiles for the a priori assessment with SGDH with DNS statistics at $12D_h$ location in heated part for cases 2 "645-050-G" (solid line) and 3 "645-100-G" (dashed line).

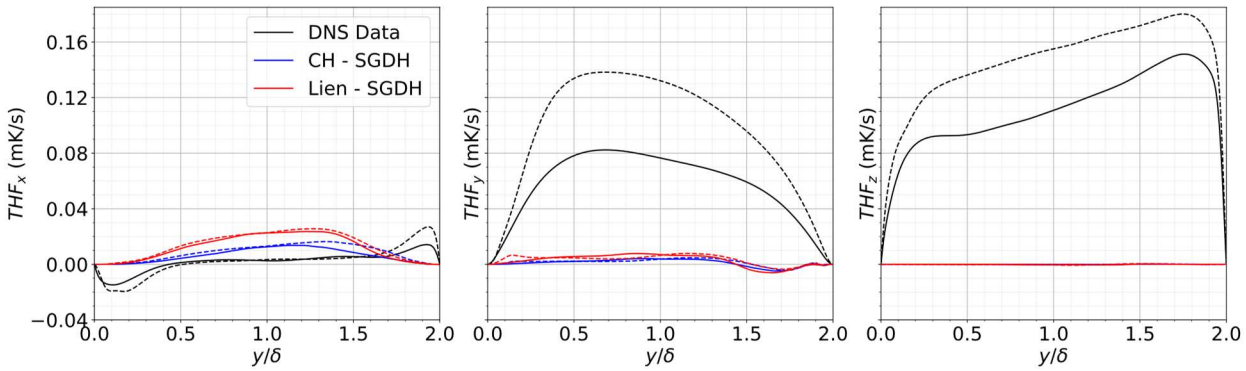

Figure 5.15. The components of turbulent heat flux profiles for the a priori assessment with SGDH with DNS statistics at $20D_h$ location in heated part for cases 2 "645-050-G" (solid line) and 3 "645-100-G" (dashed line).

In further stages, SGDH the a priori analysis prediction near zero profiles which were completely different than turbulent heat flux data obtained from DNS results. Even though temperature gradient has developed further within the redeveloped heated flow, laminarization effect significantly decreased the modeled turbulent viscosity to dampen the modeled turbulent heat flux. The SGDH model did not present any competencies at this point in terms of the prediction of the turbulent heat flux.

The GGDH is expected to capture the anisotropic behavior of turbulent flow to a limited extent due to turbulent stress information carried in the model. In contrast, the SGDH model relies on the constant turbulent Prandtl number which do not provide any directional contribution in the turbulent heat flux prediction.

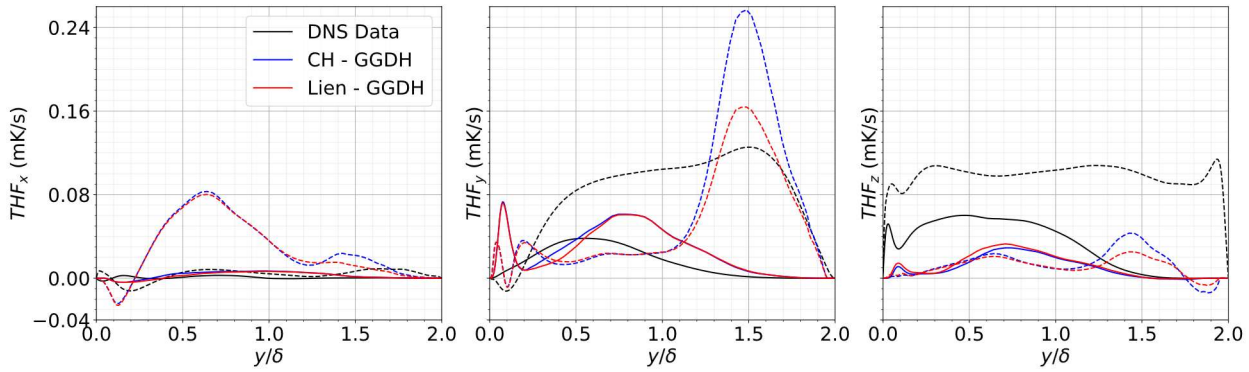

Figure 5.16. The components of turbulent heat flux profiles for the a priori assessment with GGDH with DNS statistics at $4D_h$ location in heated part for cases 2 "645-050-G" (solid line) and 3 "645-100-G" (dashed line).

The presence of Reynolds stress in the calculation contributes to directional behavior awareness that reflected into priori assessment results as model is more responsive in both wall normal and streamwise directions. At the early stage (Fig. 5.17), it was observed that angular direction term is overpredicted. The wall normal and the streamwise directions have better prediction than SGDH the a priori assessment results provided non-zero values with mostly correct sign values. However, the predicted results posed oscillating or peak regions that break off steady profile in the span of annular gap. The chaotic picture of temperature gradient and turbulent stresses under stratification of the fluid were the main causes for these regional behaviors, causing variable trend in the modeling output for a priori assessment.

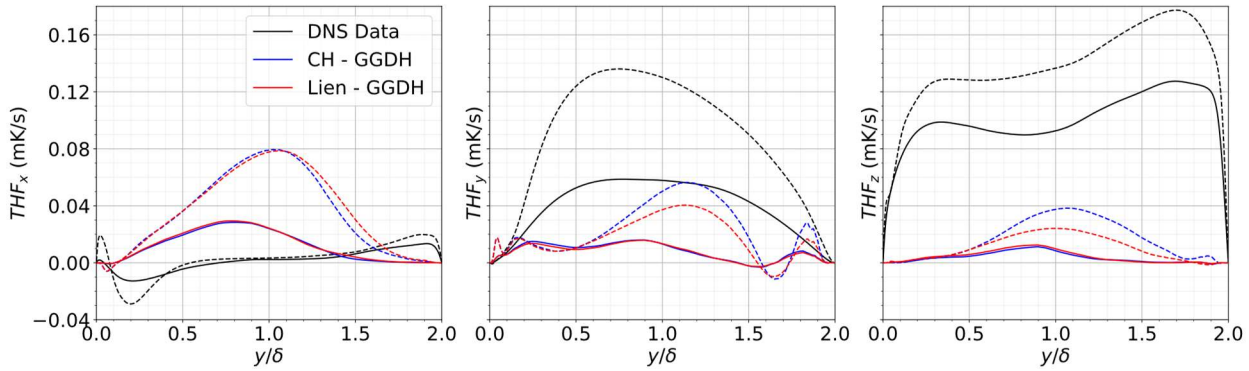

Figure 5.17. The components of turbulent heat flux profiles for the a priori assessment with GGDH in comparison to DNS statistics at $12D_h$ location in heated part for cases 2 "645-050-G" (solid line) and 3 "645-100-G" (dashed line).

The prediction performance of GGDH by a priori assessment results did not improve in the middle and end locations of the heated part shown in Fig. 5.16-18. However, model was produced predictions that results more responsive to the changes in the turbulent stresses (anisotropy) and changes in the heat flux. This improvement did not mean that results were improved, since angular direction prediction overshoot both reference and SGDH model prediction. Also, there variable trend is observed in the predicted results that did not cope with the reference data trend development.

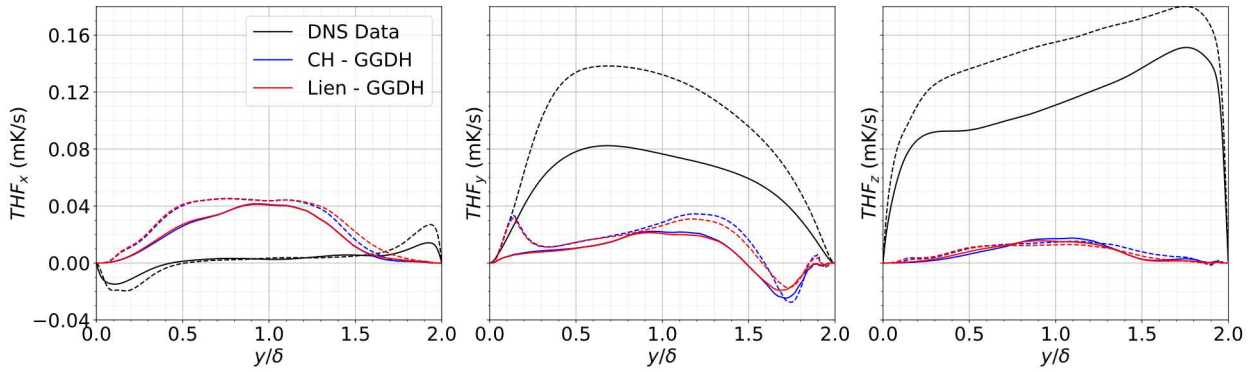

Figure 5.18. The components of turbulent heat flux profiles for the a priori assessment with GGDH in comparison to DNS statistics at $20D_h$ location in heated part for cases 2 "645-050-G" (solid line) and 3 "645-100-G" (dashed line).

It is important to mention that produced results were calculated by the a priori calculation of the Reynolds stresses for provided RANS closures. The contribution of these predicted results did not provide any conclusive information regarding which set of the closures needs to be used for better prediction since the performance of the combined a priori test of the closures presented similar predicted results in case of the use of GGDH model with both RANS closures. The GGDH hypothesis stands promising for further improvement in the prediction of turbulent heat flux (or buoyancy contribution budget) for a challenging turbulent flow conditions as provided by DNS of the turbulent flow of supercritical water within the attributes of highly anisotropic, horizontal, and buoyant flows.

5.3.2.1 Assessment of isotropic model

As both SGDH and GGDH models are investigated, it was evident that temperature gradient aided modeling is not sufficient enough to predict turbulent heat transfer reasonably well. The a priori assessment is made to get rid of uncertainties caused by low-grid resolution of RANS simulations and information loss at the fundamental quantities by modeling. In this way it is possible to focus on sole modeling error at the given cases. Yet, discrepancies were too large by two turbulent heat flux models introduced. Further focus was given to detailed investigations regarding modeling approach within the same flow conditions that data is presented. The modeling in SGDH relies on turbulent Prandtl number which was defined as the ratio of turbulent viscosity and thermal diffusivity.

$$Pr_t = \frac{\nu_t}{\alpha_t} = \frac{\overline{u_z' u_y'} / d\overline{U}_z / dy}{\overline{u_y' T'} / d\overline{T} / dy} \tag{5.22}$$

The common assumption on turbulent Prandtl number to be constant was not suitable for supercritical flows. The resulting effects of the secondary flow events together with strong thermophysical property changes creates a flow condition that makes this assumption does not

valid anymore. The turbulent viscosity calculated with DNS data by Eq 5.21 exhibits large peaks and frequent trend changes along annular gap.

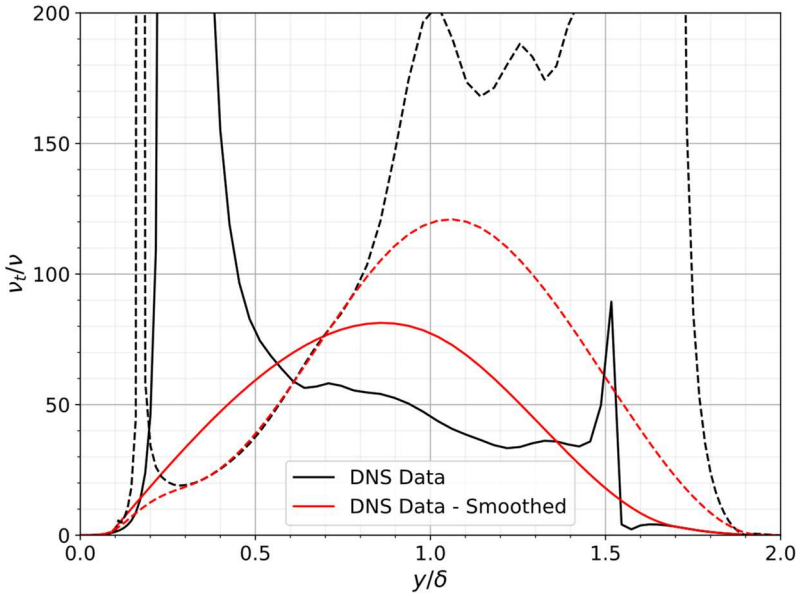

Figure 5.19. The turbulent viscosity profiles for DNS statistics and their smoothed curves at $4D_h$ location in heated part for cases 2 "645-050-G" (solid line) and 3 "645-100-G" (dashed line).

The presence of various effects simultaneously leads to ill conditioning of the velocity gradient and wall normal – streamwise shear components since DNS results present detailed picture of the flow field. The observed peaks were the result of the division of near zero or reverse velocity gradient that reaches extremely high ratio of ν_t/ν in the flow field. These values do not carry any physical meaning regarding flow conditions as they occur due to numerical instabilities. For this reason, presented profiles in Fig. 5.19 have been smoothed for further analysis regarding the observed changes in both turbulent viscosity and turbulent thermal diffusivity. Data smoothing has been performed with Savitzky-Golay filters that are used in turbulence research for data smoothing and noise reduction purposes [106], [107]. The method uses moving least squares method to fit data over low – degree polynomials making it useful for localized data smoothing.

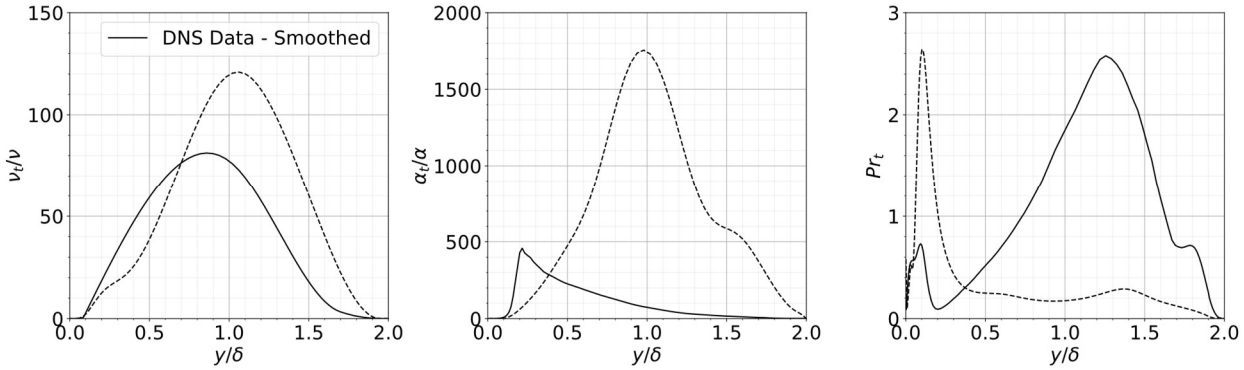

Figure 5.20. Turbulent viscosity, turbulent thermal diffusivity and turbulent Prandtl number profiles (smoothed) for DNS statistics at $4D_h$ location in heated part for cases 2 "645-050-G" (solid line) and 3 "645-100-G" (dashed line).

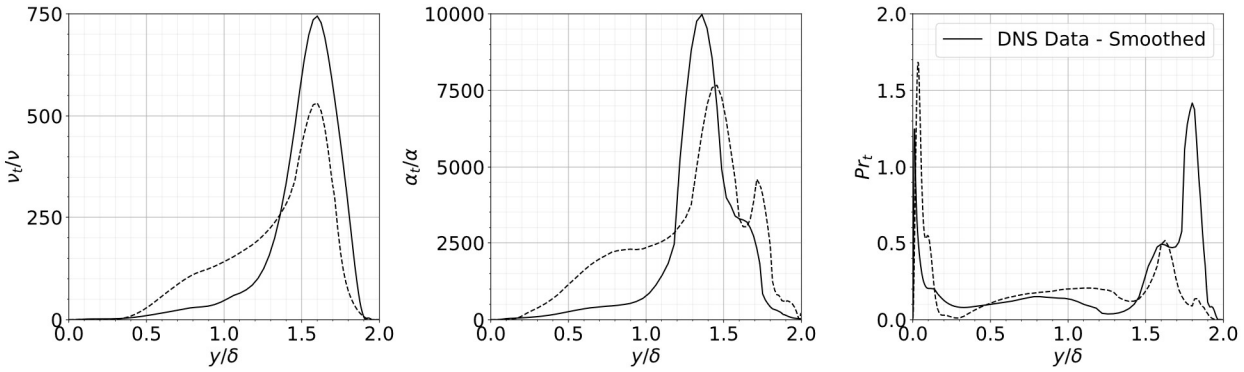

Figure 5.21. Turbulent viscosity, turbulent thermal diffusivity and turbulent Prandtl number profiles (smoothed) for DNS statistics at $12D_h$ location in heated part for cases 2 "645-050-G" (solid line) and 3 "645-100-G" (dashed line).

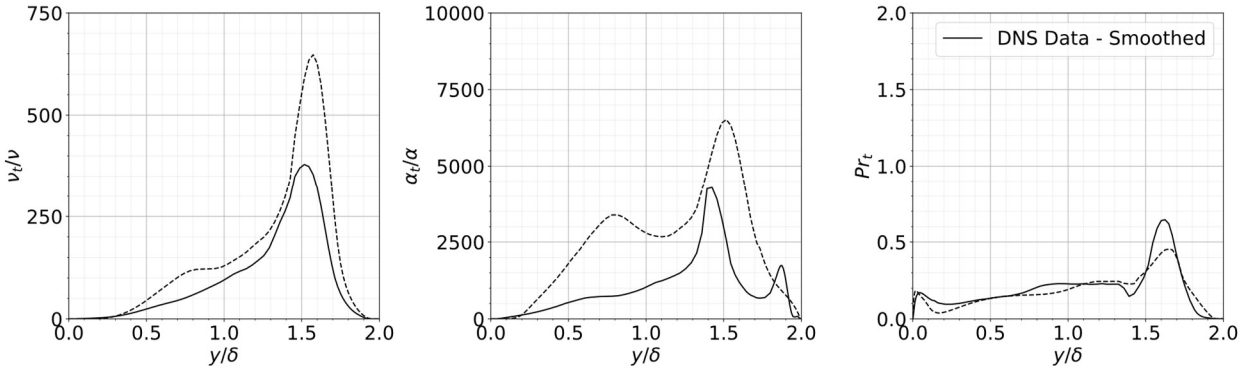

Figure 5.22. Turbulent viscosity, turbulent thermal diffusivity and turbulent Prandtl number profiles (smoothed) for DNS statistics at $20D_h$ location in heated part for cases 2 "645-050-G" (solid line) and 3 "645-100-G" (dashed line).

The turbulent viscosity is responsible to describe turbulent diffusion term in the RANS modeling. The pictures seen on figures 5.20-22 confirm the development path of turbulent diffusion term as shown in chapter 4. The development curve of the turbulent viscosity evolves and shifted with the flow progress in the heated part that was stationed where enhance mixing was observed. Meantime, the turbulent thermal diffusivity showed more activity on the same locations where turbulent viscosity curve peaks. The ratio of these parameters formed a very complex response that is presented along the heated part even though smoothed data is processed to calculate turbulent Prandtl number. The turbulent Prandtl number did not show stable profile in given flow conditions. In this case, it is clear that constant value assumption fails to accurately model the physical behavior. The distribution obtained from Eq. 5.22 exhibited the complex behavior of the turbulent viscosity and turbulent thermal diffusivity. Instant peaks at the near inner wall region coincided with the stratified layer where turbulence production was being suppressed and turbulent heat transfer was supported by high wall normal temperature gradient. Later, near wall peak diminished as flow development progresses through heated part. The rise in the second half of the annular gap was milder than the previous one. The response due to enhanced heating by the unusual rise of the turbulent viscosity was partly covered relatively weak response of the turbulent thermal diffusivity as turbulent heat transfer develops along with the production / diffusion mechanisms of turbulent kinetic energy transport.

The idea to develop a dynamic function is a challenging study for the buoyant horizontal flows since there is no symmetry that can be achieved in the radial direction. The dynamic function would require different settings for different angular positions at the same streamwise location. There are various models developed [101] for vertical flows under supercritical pressure conditions which rely on the ratio of turbulent viscosity over dynamic viscosity that can be useful for flows were not suffering from chaotic flow behavior like the one presented in this study. The proposed correlation also must be independent from any geometric properties of fluid domain and should not suffer from the entry effects for reasonable assessment. These attributes of flow research cannot be achieved within the scope of flow conditions presented in this thesis. Also, it is clear that SGDH hypothesis was not able to capture anisotropic behavior of turbulent heat transfer sourced from the highly anisotropic flow regime.

5.3.2.2 Assessment of anisotropic model

GGDH hypothesis was more aware to anisotropy of the turbulence as it shares the stress component. Also, It presented more stable prediction performance compared to SGDH in the a priori analysis results. Although, the use of temperature gradient carries the information on heat transfer, it was not sufficient enough to predict the wall normal and the streamwise component of the turbulent heat flux. GGDH hypothesis has already extended in several attempts [98] to include anisotropy or higher order correlations to improve its prediction performance. However, prediction of the streamwise component still needs further improvement. In Figures 5.23-24, results obtained by applying the GGDH model equation provided in Eq. 5.20 directly to the DNS data were used observe potential weaknesses of the GGDH model as if the input data were free of any additional modeling errors.

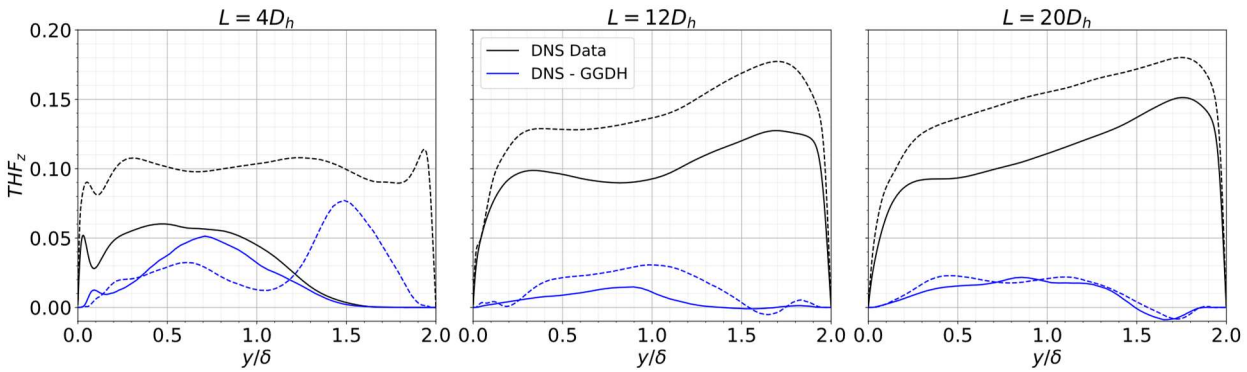

Figure 5.23. The comparison of the streamwise direction turbulent heat flux component results from DNS, GGDH prediction calculated by DNS data for different stages at the top region of the heated part for cases 2 “645-050-G” (solid line) and 3 “645-100-G” (dashed line).

As the GGDH model utilized with the DNS data, model performed slightly better in comparison to the results obtained by the joint a priori assessment with the RANS closures selected. However, model presented mean error value of 92.69% which cannot be considered reasonable prediction performance against reference data.

The model fails to capture several features of the flow field presented.

- The use of temperature gradient was not sufficient enough to capture reference turbulent heat flux distribution since the temperature gradient was only effective at the near wall but the presence of the turbulent heat flux reaches to collapse all annular gap provided.
- Model was not able to capture highly anisotropic state of the turbulent flow. Provided Reynolds stress component for the Eq. 5.20 showed limited responsiveness even though flow anisotropy focused on the streamwise direction.

The wall normal direction turbulent heat flux profiles were plotted in addition to assess the degree of poor prediction performance.

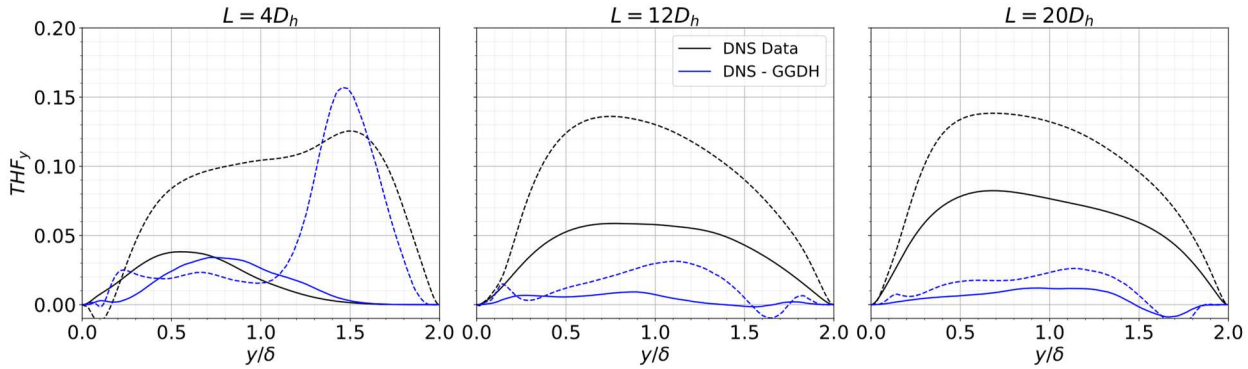

Figure 5.24. The comparison of the wall normal (y) direction turbulent heat flux component results from DNS, GGDH prediction calculated by DNS data for different stages at the top region of the heated part for cases 2 “645-050-G” (solid line) and 3 “645-100-G” (dashed line).

The wall normal component turbulent heat flux profiles showed that the model also performs poorly in the provided flow conditions. The prediction for the early stages had a relatively good agreement the other locations, but the overall performance still was not sufficient. Therefore, it was observed that model awareness is not sufficient for the increase in the heat load as the discrepancies for the case 3 considered.

The structure of the model lacks the explicit mechanism to successfully describe streamwise heat transport under highly anisotropic turbulent flow under supercritical pressure conditions. The development frame is suggested to improve prediction capability of the GGDH model on the streamwise direction and also partly in wall normal direction within following boundaries,

- Improvement should not bring any computational difficulties (model order e.g.),
- Heat load awareness should be improved,
- Directional turbulent anisotropy awareness should be improved.

In this way, GGDH prediction performance can be improved and become more responsive on the streamwise turbulent heat flux predictions for the buoyant, horizontal circular channel turbulent flows conditions.

5.4 Summary

The a priori assessment on selected two RANS closures under supercritical pressure conditions was performed to investigate how these closures respond when they are supplied with DNS data, without the influence of any filtering or modeling on the fundamental quantities unlike actual RANS simulations. The selection made to set one isotropic and anisotropic model to assess their capability to capture turbulent statistics already generated by DNS. The Reynolds stresses recalculated for this purpose by using mean velocity gradients and turbulence quantities. It was observed that the response of anisotropic model on the principal stress components was very weak and presented very close a priori assessment results, since a large fraction of the anisotropic information is lost by due to the dominance of isotopic part of the modeled stress. However, there were significant discrepancies observed at the shear component where anisotropic model (Lien model) performed fairly well at the priori assessment. Based on the model-predicted stresses, production and turbulent diffusion budgets of turbulent kinetic energy were recalculated. The similar behavior was observed here as well that responsiveness of Lien model to the secondary flow events under highly anisotropic turbulent flow was better than Chien model. Nevertheless, oscillating-noise like behavior still persisted at the a priori analysis on the prediction of turbulent diffusion budget. Even though the complex flow behavior and failure of the Boussinesq turbulent viscosity hypothesis were suspected in provided flow conditions, the main cause was the very poor prediction of the turbulent diffusion budget term was still inconclusive which should be investigated further.

The a priori assessment continued with the statistics obtained for the heated part. The results of cases 2 and 3 were used for this purpose to include the effect of heat flux. The turbulent flow field provided to the heated part exhibits highly anisotropic and intense secondary flow attributes. The responsiveness of the Lien model to predict such flow conditions by the a priori analysis was fairly well for principal components of Reynolds stress for both cases. However, the similar performance could not be pronounced for the shear component. In next step, the production and turbulent diffusion budgets of turbulent kinetic energy has been put into test following stress components. It was observed that model's capability to capture the destruction mechanism (negative production) was very limited in the a priori analysis results. Even though general trend of the DNS originated budgets are followed, destruction mechanism (negative production) is mostly reflected as production in the test results. The poor prediction quality on the turbulent diffusion term has persisted on the heated part as well.

The budget for buoyancy contribution investigated in the context of turbulent heat flux as can be simplified to the product of wall normal component by Boussinesq approximation for buoyancy. Two different widely used models to predict heat flux has been tested with the same procedure of the a priori assessment method. The SGDH model was selected for its acceptance in the literature and relevant known issues for the accurate setting of turbulent Prandtl number for supercritical flows. The GGDH model was also selected as a counterpart which deemed to be aware to turbulence related flow events and turbulent anisotropy. These models were tested with the fusion of the a priori test results of selected rans models in comparison to turbulent heat flux data by DNS. SGDH hypothesis was initiated with the constant Prandtl number value of 0.9 for horizontal flow

of SCW used for this test. Results showed that model is not able to perform well under the secondary flow effects such as buoyancy for the provided boundary conditions under supercritical pressure conditions. Rapidly falling temperature gradient and lack of responsiveness of turbulent viscosity modeling led to significantly underpredicted results. However, it was possible to assess that constant turbulent Prandtl number was not a sufficient for successful prediction. Furthermore, turbulent Prandtl number itself under significant changes which were utilized by the secondary flow events that caused immediate local changes in the flow domain affecting the turbulent viscosity and the turbulent thermal diffusivity terms. It was not possible to offer improvement path within the current results presented in this study. The GGDH model performed fairly well especially when it accompanied by Lien model in the a priori testing procedure. Unfortunately, streamwise component of the turbulent heat flux could not be predicted well by the model due to low temperature gradient in this direction. Therefore, the new model development frame suggested in this manner to enhance prediction capability of the model to be aware of changes in the heat flux and turbulent anisotropy.

6 Conclusion and future work

6.1 Conclusion

In this study, the turbulent flow under supercritical pressure conditions has been investigated in terms of turbulence and heat transfer by means of DNS. It was aimed to represent SCWR boundary conditions to provide further insight into the physical events inside the flow field. Therefore, the similarity relation has been constructed within SCWR design suggestion by KIT and the computational cost limitations of performing DNS. The simulated fuel rod geometry was modeled with the cladding material (solid domain) (SS310) and surrounding coolant (fluid domain) (supercritical water). The solid domain was provided to emphasize more realistic heat transfer mechanisms by conjugate heat transfer instead of iso-flux boundary condition that directly imposing heat into the flow domain. The flow orientation was selected as horizontal. There are several remarks obtained upon the investigation of the flow domain,

- Simulated DNS cases considered as "weak buoyancy relevant", secondary flow emerged by the heating effects significantly altered the flow field in terms of turbulence and heat transfer.
- Secondary flow events are observed throughout the heated part. The intensity of the secondary flow led to the classification of the flow field to the three parts as the top, side, and bottom regions. Even though the main flow direction is horizontal, the secondary flow not only consists of wall normal and angular direction movement of the fluid particles. The thermal expansion of the fluid and reduced shear due to heating effects led to laminarization and thermal acceleration of the flow in the main (streamwise) flow direction.
- Buoyancy effect appeared as burst of the movement of fluid particles in positive y direction (against gravity) and led to flow re-development throughout heated part. Immediate emergence of buoyant movement caused the permanent stratified layer of the fluid at the near heated wall region. The stratified layer of the fluid acted as a barrier that forms an additional layer in the bulk flow that can be distinguished by the present and post effects leading to suppressed transport of the turbulence and heat transfer. It has caused the complex picture of the turbulent heated flow in the top region including enhanced thermal mixing, laminarization, and buoyancy effects.
- Increased heat flux amplified the presence of secondary flow events mentioned above. The presence of secondary flow became more visible where it was seen that it stretches out until the bottom region of the annular pipe at the end locations of the heated part. Heat

transfer quality suffered from the immediate drop by the entry effects at the beginning of the heated part. Recovery of the heat transfer quality after the early fall is observed on the base case as a gradual, irregular rise in connection to the flow redevelopment process. However, increased heat flux led to different course of development. The heat transfer quality entered the fall trend for the rest of the annular pipe due to intensified stratified layer of the fluid. It is concluded that heat load plays an important role on the level of stratification of fluid and also deterioration or recovery of the heat transfer.

- The gravity is removed from the system in the second analysis. In this way, buoyancy induced part of the secondary flow were removed from the flow domain. Heat removal from the heated inner wall surface is greatly reduced. Heat transport relied on the conductive and molecular mechanisms which were not efficient as turbulent transport.
- As the gravity is removed, effectiveness of wall dampening on the temperature fluctuations are decreased due to lack of turbulent transport mechanisms.

Results obtained on the DNS showed that the turbulent flow simulated under provided boundary conditions and flow domain shows attributes of highly anisotropic state of the turbulence. Therefore, two RANS models were selected by their capabilities to be aware of turbulent anisotropy. These models are put into test by the a priori analysis by flow data provided by DNS results to assess how they fare under the highly anisotropic turbulent flow conditions within SCWR conditions. Following insights are gained upon a priori test conducted,

- The anisotropic behavior was not captured well under the provided DNS data and the concept of the priori analysis. Both models showed similar results in the representation of the principal stress components. On the other hand, the shear component was predicted to be significantly better by the Lien model. Meaning that anisotropy information is not totally lost. The destruction mechanism (negative production) in the transport of turbulent kinetic energy cannot be captured by the model equations. The turbulent transport and production budgets are predicted fairly better as well as Reynolds stresses by Lien model in comparison to Chien model.
- Buoyancy production budget was investigated under the scope of Boussinesq approximation on turbulent heat flux models. Two models by SGDH and GGDH hypothesis were selected for further investigation by testing their prediction capability to reproduce turbulent heat flux obtained by DNS with very complex flow field. Both of the models present poor prediction results by both the a priori analysis and sole calculation by DNS data. the GGDH model presented better predicted results than the SGDH. Both of models were poorly responsive turbulent anisotropy and heat load changes.
- SGDH model was driven by the model approaches for the turbulent Prandtl number and turbulent viscosity. It was observed that common practice of the idea of constant Prantl number was not valid under SCWR conditions. Further contribution cannot be succeeded as provided results require more high-fidelity numerical simulations for reasonable assessment.
- The model development framework has offered in the base of GGDH model within the limited scope of to increase model responsiveness on heat load and turbulent anisotropy in the streamwise direction of the turbulent heat flux.

In summary, the study conducted in this thesis used to characterize the changes in the heated turbulent flow under SCWR conditions provided under the similarity relation constructed. Therefore, it stands as a reference data of turbulence and heat transfer of high-fidelity simulation that uses geometry of SCWR fuel rod and surrounding coolant by conjugate heat transfer. The comparative study provided between conducted DNS cases is used to identify the heating effects causing the secondary flow and relevant core physical mechanisms behind it. The insight gained by the priori test results spotted the potential weaknesses of cost-effective CFD approaches used to aid the development of advanced SCWR designs.

6.2 Future work

There are several aspects that can be implied such as future work,

- There is need of high-resolution simulations without the entry effects observed at the entry stages of the heated part. In this way, the statistics of the fully redeveloped heated flow can be obtained to provide conclusive picture regarding turbulence and heat transfer.
- Computational limitations can be relaxed withing the use of additional tools or modeling to be closer to the SCWR conditions while preserving the quality of obtained statistics. LES, DDES, RANS methods can be coupled with the machine learning methods and physics informed neural networks to gain access to high quality detailed information on the turbulent flow statistics utilizing foreseen SCWR conditions.
- A priori test conducted in this study can be re-evaluated by RANS simulations to observe full extent of the changes due to turbulence modeling approach. These models can be improved by the insight gained.
- There are known weaknesses on the prediction of the turbulent heat flux. Even though there are various models, consensus has not been reached yet on the use of these models. Therefore, there is a need of further development of the turbulent heat flux models for more robust prediction models.

These suggested potential research works will enhance the knowledge obtained regarding the turbulent flow of the supercritical water. The knowledge gaps addressed in the scope of this thesis can be understood further with targeted numerical studies within the support of experimental studies to be held in parallel. Findings will support the advances in the SCWR designs and other engineering works dealing with supercritical flows.

7 References

[1] J. G. Marques, “Evolution of nuclear fission reactors: Third generation and beyond,” in *Energy Conversion and Management*, Sep. 2010, pp. 1774–1780. doi: 10.1016/j.enconman.2009.12.043.

[2] B. Wealer, S. Bauer, C. V. Hirschhausen, C. Kemfert, and L. Göke, “Investing into third generation nuclear power plants - Review of recent trends and analysis of future investments using Monte Carlo Simulation,” *Renewable and Sustainable Energy Reviews*, vol. 143, Jun. 2021, doi: 10.1016/j.rser.2021.110836.

[3] OECD Nuclear Energy Agency for the Generation IV International Forum, “Technology Roadmap Update for Generation IV Nuclear Energy Systems,” Jan. 2014.

[4] U.S. DOE Nuclear Energy Research Advisory Committee and Generation IV International Forum, “A Technology Roadmap for Generation IV Nuclear Energy Systems,” Dec. 2002.

[5] M. M. Rahman, J. Dongxu, N. Jahan, M. Salvatores, and J. Zhao, “Design concepts of supercritical water-cooled reactor (SCWR) and nuclear marine vessel: A review,” *Progress in Nuclear Energy*, vol. 124, no. 3787, p. 103320, 2020, doi: 10.1016/j.pnucene.2020.103320.

[6] X. Cheng and T. Schulenberg, “Heat Transfer at Supercritical Pressures-Literature Review and Application to an HPLWR,” Karlsruhe, Germany: Forschungszentrum Karlsruhe GmbH, May 2001, doi: 10.5445/IR/270049813.

[7] I. Tiselj, R. Bergant, B. Mavko, I. Bajsić, and G. Hetsroni, “DNS of turbulent heat transfer in channel flow with heat conduction in the solid wall,” *J. Heat Transfer*, vol. 123, no. 5, pp. 849–857, 2001, doi: 10.1115/1.1389060.

[8] T. Schulenberg and I. Otic, “Suggestion for Design of a Small Modular SCWR,” in Proc. 10th Int. Symp. on SCWRs (ISSCWR-10), Prague, Czech Republic, Mar. 15–19, 2021, Paper ISSCWR10-019..

[9] E. W. Lemmon, M. O. McLinden, and D. G. Friend, “Thermophysical Properties of Fluid Systems,” NIST Chemistry WebBook, NIST Standard Reference Database (SRD) 69, National Institute of Standards and Technology. [Online]. Available: https://webbook.nist.gov /chemistry/fluid/

[10] I. Pioro and S. Mokry, “Thermophysical Properties at Critical and Supercritical Conditions.” Heat Transfer - Theoretical Analysis, Experimental Investigations and Industrial Systems, Prof. Aziz Belmiloudi (Ed.) [Online]. Available: www.intechopen.com

[11] S. B. Pope, *Turbulent Flows*, no. 9. Cambridge University Press, 2000.

[12] B. R. Munson, T. H. Okiishi, W. W. Huebsch, and A. P. Rothmayer, *Fundamentals of Fluid Mechanics*, 7th ed. John Wiley & Sons, Inc. [Online]. Available: www.wileyplus.com

[13] P. S. Bernard’ A N D and R. A. Handler, “Reynolds stress and the physics of turbulent momentum transport,” *J. Fluid Mech*, vol. 220, pp. 99–124, 1990, doi: 10.1017/ S0022112090003202.

[14] S. Banerjee, Ö. Ertunç, and F. Durst, “Measurement and modeling of homogenous axisymmetric turbulence,” *Journal of Turbulence*, vol. 10, pp. 1–33, 2009, doi: 10.1080/14685240902744692.

[15] L. Neuhaus *et al.*, “Influence of Surface Roughness on the Turbulent Properties in the Wake of a Turbine Blade,” in *Proc. 18th Int. Symp. on Applications of Laser and Imaging Techniques to Fluid Mechanics*, Lisbon, Portugal, Jul. 4–7, 2016.

[16] N. L. Lumley and G. R. Newmans, “The return to isotropy of homogeneous turbulence,” *J. Fluid Mech.*, vol. 82, no. 1, pp. 161–178, 1977, doi: 10.1017/S0022112077000585.

[17] S. Banerjee, R. Krahl, F. Durst, and C. Zenger, “Presentation of anisotropy properties of turbulence, invariants versus eigenvalue approaches,” *Journal of Turbulence*, vol. 8, pp. 1–27, 2007, doi: 10.1080/14685240701506896.

[18] L. Jofre, S. P. Domino, and G. Iaccarino, “A Framework for Characterizing Structural Uncertainty in Large-Eddy Simulation Closures,” *Flow Turbul. Combust.*, vol. 100, no. 2, pp. 341–363, Mar. 2018, doi: 10.1007/s10494-017-9844-8.

[19] H. Schlichting and K. Gersten, *Boundary-Layer Theory*, 9th ed. Berlin, Germany: Springer, 2017, doi: 10.1007/978-3-662-52919-5.

[20] J. G. M. Eggels, F. Unger, M. H. Weiss, J. Westerweel, R. J. Adrian, and F. T. M. Nieuwstadt, “Fully developed turbulent pipe flow: A comparison between direct numerical simulation and experiment,” 1994. doi: 10.1017/S002211209400131X.

[21] J. Kim, P. Moin, and R. Moser, “Turbulence statistics in fully developed channel flow at low reynolds number,” *J. Fluid Mech.*, vol. 177, no. May, pp. 133–166, 1987, doi: 10.1017/S0022112087000892.

[22] T. L. Bergman, A. S. Lavine, F. P. Incropera, and D. P. DeWitt, *Fundamentals of Heat and Mass Transfer*, 7th ed. John Wiley & Sons, Inc., 2011.

[23] X. Cheng, Y. H. Yang, and S. F. Huang, “A simplified method for heat transfer prediction of supercritical fluids in circular tubes,” *Ann. Nucl. Energy*, vol. 36, no. 8, pp. 1120–1128, 2009, doi: 10.1016/j.anucene.2009.04.016.

[24] I. L. Pioro and R. B. Duffey, "Experimental Heat Transfer to Other Fluids at Supercritical Pressures," *Heat Transfer & Hydraulic Resistance at Supercritical Pressures in Power Engineering Applications*, no. January 2011, pp. 109–115, 2010, doi: 10.1115/1.802523.ch8.

[25] T. H. Kim, J. G. Kwon, M. H. Kim, and H. S. Park, "Experimental investigation on validity of buoyancy parameters to heat transfer of CO2 at supercritical pressures in a horizontal tube," *Exp. Therm. Fluid Sci.*, vol. 92, pp. 222–230, Apr. 2018, doi: 10.1016/j.expthermflusci.2017.11.024.

[26] K. Theologou, R. Mertz, E. Laurien, and J. Starflinger, "Experimental investigations on heat transfer of CO2 under supercritical pressure in heated horizontal pipes," *Energy*, vol. 254, Sep. 2022, doi: 10.1016/j.energy.2022.124171.

[27] I. L. Pioro and R. B. Duffey, "Experimental heat transfer in supercritical water flowing inside channels (survey)," *Nuclear Engineering and Design*, vol. 235, no. 22, pp. 2407–2430, Nov. 2005, doi: 10.1016/j.nucengdes.2005.05.034.

[28] G. A. Adebiyi and W. B. Hall, "Experimental investigation of heat transfer to supercritical pressure carbon dioxide in a horizontal pipe," *Int. J. Heat Mass Transf.*, vol. 19, no. 7, pp. 715–720, Jul. 1976, doi: 10.1016/0017-9310(76)90123-X.

[29] R. Tian, Y. Zhang, Y. Ma, H. Li, and L. Shi, "Experimental study of buoyancy effect and its criteria for heat transfer of supercritical R134a in horizontal tubes," *Int. J. Heat Mass Transf.*, vol. 127, pp. 555–567, Dec. 2018, doi: 10.1016/j.ijheatmasstransfer.2018.08.072.

[30] "Natural circulation in water cooled nuclear power plants : phenomena models and methodology for system reliability assessments," International Atomic Energy Agency, Vienna, Austria, Nov. 2005.

[31] D. Huang and W. Li, "A brief review on the buoyancy criteria for supercritical fluids," Feb. 25, 2018, *Elsevier Ltd*. doi: 10.1016/j.applthermaleng.2017.12.042.

[32] B. Zhang, J. Shan, and J. Jiang, "Numerical analysis of supercritical water heat transfer in horizontal circular tube," *Progress in Nuclear Energy*, vol. 52, no. 7, pp. 678–684, Sep. 2010, doi: 10.1016/j.pnucene.2010.03.006.

[33] K. Yamagata, K. Nishikawa, S. Hasegawa, T. Fujii, and S. Yoshida, "Forced convective heat transfer to supercritical water flowing in tubes," *Int. J. Heat Mass Transf.*, vol. 15, no. 12, pp. 2575–2593, Dec. 1972, doi: 10.1016/0017-9310(72)90148-2.

[34] R. B. Duffey and I. L. Pioro, "Experimental heat transfer of supercritical carbon dioxide flowing inside channels (survey)," *Nuclear Engineering and Design*, vol. 235, no. 8, pp. 913–924, 2005, doi: 10.1016/j.nucengdes.2004.11.011.

[35] C. R. Zhao and P. X. Jiang, "Experimental study of in-tube cooling heat transfer and pressure drop characteristics of R134a at supercritical pressures," *Exp. Therm. Fluid Sci.*, vol. 35, no. 7, pp. 1293–1303, Oct. 2011, doi: 10.1016/j.expthermflusci.2011.04.017.

[36] J. D. Jackson, “Fluid flow and convective heat transfer to fluids at supercritical pressure,” *Nuclear Engineering and Design*, vol. 264, pp. 24–40, 2013, doi: 10.1016/j.nucengdes .2012.09.040.

[37] S. Yu *et al.*, “Influence of buoyancy on heat transfer to water flowing in horizontal tubes under supercritical pressure,” *Appl. Therm. Eng.*, vol. 59, no. 1–2, pp. 380–388, 2013, doi: 10.1016/j.applthermaleng.2013.05.034.

[38] S. Yu *et al.*, “Experimental investigation on heat transfer characteristics of supercritical pressure water in a horizontal tube,” *Exp. Therm. Fluid Sci.*, vol. 50, pp. 213–221, 2013, doi: 10.1016/j.expthermflusci.2013.06.011.

[39] Z. Bin Liu, Y. L. He, Y. F. Yang, and J. Y. Fei, “Experimental study on heat transfer and pressure drop of supercritical CO2 cooled in a large tube,” *Appl. Therm. Eng.*, vol. 70, no. 1, pp. 307–315, Sep. 2014, doi: 10.1016/j.applthermaleng.2014.05.024.

[40] X. Lei, H. Li, N. Dinh, and W. Zhang, “A study of heat transfer scaling of supercritical pressure water in horizontal tubes,” *Int. J. Heat Mass Transf.*, vol. 114, pp. 923–933, 2017, doi: 10.1016/j.ijheatmasstransfer.2017.06.052.

[41] X. Lei, H. Li, W. Zhang, N. T. Dinh, Y. Guo, and S. Yu, “Experimental study on the difference of heat transfer characteristics between vertical and horizontal flows of supercritical pressure water,” *Appl. Therm. Eng.*, vol. 113, pp. 609–620, Feb. 2017, doi: 10.1016/j.applthermaleng.2016.11.051.

[42] N. Kasagi, Y. Tomita, and A. Kuroda, “Direct Numerical Simulation of Passive Scalar Field in a Turbulent Channel Flow,” *Fluid Mechanics and its Applications*, vol. 46, no. August 1992, pp. 551–554, 1992, doi: 10.1007/978-94-011-5118-4_136.

[43] N. Kasagi, A. Kuroda, and M. Hirata, “Numerical investigation of near- wall turbulent heat transfer taking into account the unsteady heat conduction in the solid wall,” *J. Heat Transfer*, vol. 111, no. 2, pp. 385–392, 1989, doi: 10.1115/1.3250689.

[44] C. Flageul, S. Benhamadouche, É. Lamballais, and D. Laurence, “DNS of turbulent channel flow with conjugate heat transfer: Effect of thermal boundary conditions on the second moments and budgets,” *Int. J. Heat Fluid Flow*, vol. 55, no. August, pp. 34–44, 2015, doi: 10.1016/j.ijheatfluidflow.2015.07.009.

[45] I. Tiselj and L. Cizelj, “DNS of turbulent channel flow with conjugate heat transfer at Prandtl number 0.01,” *Nuclear Engineering and Design*, vol. 253, pp. 153–160, 2012, doi: 10.1016/j.nucengdes.2012.08.008.

[46] I. Tiselj, J. Oder, and L. Cizelj, “Double-sided cooling of heated slab: Conjugate heat transfer DNS,” *Int. J. Heat Mass Transf.*, vol. 66, pp. 781–790, 2013, doi: 10.1016/j.ijheatmasstransfer.2013.07.076.

[47] F. Cédric, S. Benhamadouche, É. Lamballais, and D. Laurence, “On the discontinuity of the dissipation rate associated with the temperature variance at the fluid-solid interface for cases

with conjugate heat transfer," *Int. J. Heat Mass Transf.*, vol. 111, pp. 321–328, 2017, doi: 10.1016/j.ijheatmasstransfer.2017.04.005.

[48] A. M. Shehata, D. M. McEligot, "Mean structure in the viscous layer of strongly heated internal gas flow measurements," *Int. J. Heat Mass Transf.*, vol. 41, no. 24, pp. 4297–4313, Oct. 1998, doi: 10.1016/S0017-9310(98)00088-X.

[49] J. H. Bae, J. Y. Yoo, and H. Choi, "Direct numerical simulation of turbulent supercritical flows with heat transfer," *Physics of Fluids*, vol. 17, no. 10, 2005, doi: 10.1063/1.2047588.

[50] D. P. Mikielewicz, A. M. Shehata, J. D. Jackson, and D. M. McEligot, "Temperature, velocity and mean turbulence structure in strongly heated internal gas flows. Comparison of numerical predictions with data," *Int. J. Heat Mass Transf.*, vol. 45, no. 21, pp. 4333–4352, 2002, doi: 10.1016/S0017-9310(02)00119-9.

[51] S. Satake, T. Kunugi, A. M. Shehata, and D. M. McEligot, "Direct numerical simulation for laminarization of turbulent forced gas flows in curcular tubes with strong heating," *Int. J. Heat Fluid Flow*, 2000.

[52] X. Xu, "Large eddy simulation of compressible turbulent pipe flow with heat transfer," Ph.D. dissertation, Iowa State Univ., Ames, IA, USA, 2003.

[53] P. Zhao, J. Liu, Z. Ge, Y. Li, N. Zhao, and Y. Wan, "Direct numerical simulation of strongly heated air flows in a vertical pipe using a thermophysical property table," *Int. J. Heat Mass Transf.*, vol. 124, pp. 1181–1197, Sep. 2018, doi: 10.1016/j.ijheatmasstransfer.2018.04.004.

[54] H. Nemati, A. Patel, B. J. Boersma, and R. Pecnik, "The effect of thermal boundary conditions on forced convection heat transfer to fluids at supercritical pressure," *J. Fluid Mech.*, vol. 800, pp. 531–556, Aug. 2016, doi: 10.1017/jfm.2016.411.

[55] Y. L. Cao, R. N. Xu, J. J. Yan, S. He, and P. X. Jiang, "Direct numerical simulation of convective heat transfer of supercritical pressure CO2 in a vertical tube with buoyancy and thermal acceleration effects," *J. Fluid Mech.*, vol. 927, pp. 1–36, 2021, doi: 10.1017/jfm.2021.705.

[56] J. He, R. Tian, P. X. Jiang, and S. He, "Turbulence in a heated pipe at supercritical pressure," *J. Fluid Mech.*, vol. 920, pp. 1–38, 2021, doi: 10.1017/jfm.2021.458.

[57] S. Pandey, X. Chu, and E. Laurien, "Numerical analysis of heat transfer during cooling of supercritical fluid by means of direct numerical simulation," in *High Performance Computing in Science and Engineering' 17: Transactions of the High Performance Computing Center, Stuttgart (HLRS) 2017*, Springer International Publishing, 2018, pp. 241–254. doi: 10.1007/978-3-319-68394-2_14.

[58] X. Chu and E. Laurien, "Direct numerical simulation of heated turbulent pipe flow at supercritical pressure," *Journal of Nuclear Engineering and Radiation Science*, vol. 2, no. 3, Jul. 2016, doi: 10.1115/1.4032479.

[59] J. H. Bae, J. Y. Yoo, and D. M. McEligot, “Direct numerical simulation of heated CO2 flows at supercritical pressure in a vertical annulus at Re=8900,” *Physics of Fluids*, vol. 20, no. 5, 2008, doi: 10.1063/1.2927488.

[60] J. W. R. Peeters, R. Pecnik, M. Rohde, T. H. J. J. van der Hagen, and B. J. Boersma, “Turbulence attenuation in simultaneously heated and cooled annular flows at supercritical pressure,” *J. Fluid Mech.*, vol. 799, pp. 505–540, Jul. 2016, doi: 10.1017/jfm.2016.383.

[61] J. W. R. Peeters, R. Pecnik, M. Rohde, T. H. J. J. Van Der Hagen, and B. J. Boersma, “Characteristics of turbulent heat transfer in an annulus at supercritical pressure,” *Phys. Rev. Fluids*, vol. 2, no. 2, Feb. 2017, doi: 10.1103/PhysRevFluids.2.024602.

[62] J. Liu, Y. Jin, P. Zhao, Z. Ge, Y. Li, and Y. Wan, “Analysis of heat transfer of supercritical water by direct numerical simulation of heated upward pipe flows,” *International Journal of Thermal Sciences*, vol. 138, pp. 206–218, Apr. 2019, doi: 10.1016/j.ijthermalsci .2018.12.028.

[63] Y. Bai, H. Wang, M. Liu, J. Wu, H. Lyu, and Y. Huang, “Direct numerical simulation of flow and heat transfer of supercritical water with different heat fluxes,” *Int. J. Heat Mass Transf.*, vol. 221, Apr. 2024, doi: 10.1016/j.ijheatmasstransfer.2023.125132.

[64] X. Chu and E. Laurien, “Flow stratification of supercritical CO2 in a heated horizontal pipe,” *Journal of Supercritical Fluids*, vol. 116, pp. 172–189, Oct. 2016, doi: 10.1016/j.supflu.2016.05.003.

[65] W. Wang, S. He, C. Moulinec, and D. R. Emerson, “Direct numerical simulation of thermal stratification of supercritical water in a horizontal channel,” *Comput. Fluids*, vol. 261, Jul. 2023, doi: 10.1016/j.compfluid.2023.105911.

[66] A. Pucciarelli and W. Ambrosini, “On the effect of conjugate heat transfer on turbulence in supercritical fluids: Results from a LES application,” *Ann. Nucl. Energy*, vol. 111, pp. 340–346, Jan. 2018, doi: 10.1016/j.anucene.2017.09.020.

[67] J. He, B. Xu, and S. He, “Effect of conjugate heat transfer on the simulation of flow at supercritical pressure,” in Proc. 17th UK Heat Transfer Conf. (UKHTC2021), Manchester, U.K., Apr. 4–6, 2022, Paper O-9-5.

[68] J. Buongiorno and P. MacDonald, “Progress Report for the FY-03 Generation-IV R&D Activities for the Development of the SCWR in the U.S.,” Sep. 2003. [Online]. Available: http://nuclear.inl.gov/gen4/docs/scwr_annual_progress_report_gen-iv_fy-03.pdf

[69] Y. Zeng and D. Guzonas, “Corrosion assessment of candidate materials for fuel cladding in Canadian SCWR,” *JOM*, vol. 68, no. 2, pp. 475–479, Feb. 2016, doi: 10.1007/s11837-015-1745-5.

[70] AZO Materials, “Properties_ Stainless Steel - Grade 310 (UNS S31000).” Accessed: Jan. 03, 2025. [Online]. Available: https://www.azom.com/properties.aspx?ArticleID=966

[71] E. Marín, “Characteristic dimensions for heat transfer,” *Lat. Am. J. Phys. Educ.*, vol. 4, no. 1, Jan. 2010, [Online]. Available: http://www.journal.lapen.org.mx

[72] T. Reiss, G. Csom, S. Fehér, S. Czifrus, and M. Szieberth, "Full-core SSCWR calculations applying a fast computational method," *Progress in Nuclear Energy*, vol. 52, no. 8, pp. 767–776, Nov. 2010, doi: 10.1016/j.pnucene.2010.06.003.

[73] H. Tsige-Tamirat and L. Ammirabile, "Study on the use of hydride fuel in high-performance light water reactor concept," *Science and Technology of Nuclear Installations*, vol. 2015, 2015, doi: 10.1155/2015/965274.

[74] L. Vlahovic, D. Staicu, A. Küst, and R. J. M. Konings, "Thermal diffusivity of UO2 up to the melting point," *Journal of Nuclear Materials*, vol. 499, pp. 504–511, Feb. 2018, doi: 10.1016/j.jnucmat.2017.11.050.

[75] J. K. Fink, M. G. Chasanov, and L. Leibowitz, "Thermophysical Properties of Uranium Dioxide," *Journal of Nuclear Materials*, vol. 102, pp. 17–25, Aug. 1981, doi: 10.1016/0022-3115(81)90541-9.

[76] B. E. Launder and D. B. Spalding, "The numerical computation of turbulent flows," *Comput. Methods Appl. Mech. Eng.*, vol. 3, pp. 269–289, 1974, doi: 10.1016/0045-7825(74)90029-2.

[77] S. Kadia, N. Rüther, I. Albayrak, and E. Pummer, "Reynolds stress modeling of supercritical narrow channel flows using OpenFOAM: Secondary currents and turbulent flow characteristics," *Physics of Fluids*, vol. 34, no. 12, 2022, doi: 10.1063/5.0124076.

[78] A. Barletta, "The Boussinesq approximation for buoyant flows," *Mech. Res. Commun.*, vol. 124, Sep. 2022, doi: 10.1016/j.mechrescom.2022.103939.

[79] I. Otić and G. Grötzbach, "Turbulent heat flux and temperature variance dissipation rate in natural convection in lead-bismuth," 2007. doi: 10.13182/NSE07-A2679.

[80] B. E. Rapp, "Numerical Methods for Solving Differential Equations," in *Microfluidics: Modelling, Mechanics and Mathematics*, Elsevier, 2017, pp. 549–593. doi: 10.1016/b978-1-4557-3141-1.50027-7.

[81] R. I. Issa, "Solution of the Implicitly Discretised Fluid Flow Equations by Operator-Splitting," *J. Comput. Phys.*, no. 1, pp. 40–65, Jan. 1986, doi: 10.1016/0021-9991(86)90099-9.

[82] S. Pandey, "Thermo-hydraulic analysis of wall bounded flows with supercritical carbon dioxide using direct numerical simulation," Ph.D. dissertation, Univ. of Stuttgart, Stuttgart, Germany, 2018.

[83] X. Chu, "Direct Numerical Simulation of Heat Transfer to Supercritical Carbon Dioxide in Pipe Flows.," Ph.D. dissertation, Univ. of Stuttgart, Stuttgart, Germany, 2016.

[84] S. Pope, "A Perspective on Turbulence Modeling," in *Modeling Complex Turbulent Flows*, Ithaca, New York: Kluwer Academic Publishers, 1999, pp. 53–67.

[85] D. Li, J. Komperda, A. Peyvan, Z. Ghiasi, and F. Mashayek, "Assessment of turbulence models using DNS data of compressible plane free shear layer flow," *J. Fluid Mech.*, vol. 931, Jan. 2022, doi: 10.1017/jfm.2021.919.

[86] W. S. Kim, S. He, and J. D. Jackson, "Assessment by comparison with DNS data of turbulence models used in simulations of mixed convection," *Int. J. Heat Mass Transf.*, vol. 51, no. 5–6, pp. 1293–1312, Mar. 2008, doi: 10.1016/j.ijheatmasstransfer.2007.12.002.

[87] S. He, W. S. Kim, and J. H. Bae, "Assessment of performance of turbulence models in predicting supercritical pressure heat transfer in a vertical tube," *Int. J. Heat Mass Transf.*, vol. 51, no. 19–20, pp. 4659–4675, 2008, doi: 10.1016/j.ijheatmasstransfer.2007.12.028.

[88] F. G. Schmitt, "About Boussinesq's turbulent viscosity hypothesis: historical remarks and a direct evaluation of its validity," *Comptes Rendus. Mécanique*, vol. 335, no. 9, pp. 617–627, 2007, doi: 10.1016/j.crme.2007.08.004ï.

[89] W. P. Jones and B. E. Launder, "The Prediction of Laminarization with a Two-Equation Model of Turbulence," *International Journal of Heat Mass Transfer*, vol. 15, pp. 301–314, May 1971.

[90] Y. Y. Bae, E. S. Kim, and M. Kim, "Assessment of low-Reynolds number k-ε turbulence models against highly buoyant flows," *Int. J. Heat Mass Transf.*, vol. 108, pp. 529–536, 2017, doi: 10.1016/j.ijheatmasstransfer.2016.12.039.

[91] M. Mohseni and M. Bazargan, "The effect of the low Reynolds number k-e turbulence models on simulation of the enhanced and deteriorated convective heat transfer to the supercritical fluid flows," *Heat and Mass Transfer*, vol. 47, no. 5, pp. 609–619, May 2011, doi: 10.1007/s00231-010-0753-9.

[92] J. Wang, J. Gong, X. Kang, C. Zhao, and K. Hooman, "Assessment of RANS turbulence models on predicting supercritical heat transfer in highly buoyant horizontal flows," *Case Studies in Thermal Engineering*, vol. 34, Jun. 2022, doi: 10.1016/j.csite.2022.102057.

[93] F. S. Lien, W. L. Chen, and M. A. Leschziner, "Low-Reynolds-Number Eddy-Viscosity Modelling Based on Non-Linear Stress-Strain/Vorticity Relations," in *Engineering Turbulence Modelling and Experiments*, Elsevier, 1996, pp. 91–100. doi: 10.1016/b978-0-444-82463-9.50015-0.

[94] A. Alasif, O. Siddiqui, A. Pucciarelli, and A. Shams, "Numerical Prediction of Heat Transfer for Supercritical Carbon Dioxide in Horizontal Circular Tubes," in *Proceedings of the Saudi International Conference on Nuclear Power Engineering 2023 (SCOPE 2023), 2024* https://doi.org/10.1007/978-3-031-64362-0_44

[95] A. Einstein, "Die Grundlage der allgemeinen Relativitätstheorie," *Ann. Phys.*, vol. 354, no. 7, pp. 769–822, 1916, doi: 10.1002/andp.19163540702.

[96] P. X. Jiang, Z. C. Wang, and R. N. Xu, "A modified buoyancy effect correction method on turbulent convection heat transfer of supercritical pressure fluid based on RANS model,"

Int. J. Heat Mass Transf., vol. 127, pp. 257–267, Dec. 2018, doi: 10.1016/j.ijheatmasstransfer.2018.07.042.

[97] J. Xiong and X. Cheng, "Turbulence modelling for supercritical pressure heat transfer in upward tube flow," *Nuclear Engineering and Design*, vol. 270, pp. 249–258, 2014, doi: 10.1016/j.nucengdes.2014.01.014.

[98] X. Wang, J. Hussong, and S. Jakirlić, "Curvature influence on flow and heat transfer in a concentric annulus: Conventional and sensitized Reynolds stress modeling study," *Int. J. Heat Mass Transf.*, vol. 249, p. 127192, Oct. 2025, doi: 10.1016/j.ijheatmasstransfer.2025.127192.

[99] M. Mohseni and M. Bazargan, "A New Correlation for the Turbulent Prandtl Number in Upward Rounded Tubes in Supercritical Fluid Flows," *J. Heat Transfer*, vol. 138, no. 8, Aug. 2016, doi: 10.1115/1.4033137.

[100] Y. Y. Bae, "A new formulation of variable turbulent Prandtl number for heat transfer to supercritical fluids," *Int. J. Heat Mass Transf.*, vol. 92, pp. 792–806, Jan. 2016, doi: 10.1016/j.ijheatmasstransfer.2015.09.039.

[101] Z. Hou, X. Guo, Z. Liang, K. Yang, C. Yang, and H. Wang, "Improvement on numerical simulation of supercritical water flow in horizontal tubes: A buoyancy-tuned turbulent Prandtl number model," *Int. J. Heat Mass Transf.*, vol. 232, Nov. 2024, doi: 10.1016/j.ijheatmasstransfer.2024.125928.

[102] M. Mir Emad, K. Mazaheri, and M. Darbandi, "Assessment of algebraic anisotropic turbulent heat flux models using Reynolds stress modeling for simulating film cooling flows," *Physics of Fluids*, vol. 37, no. 1, Jan. 2025, doi: 10.1063/5.0245045.

[103] S. V. Poroseva, J. D. Colmenares F., and S. M. Murman, "On the accuracy of RANS simulations with DNS data," *Physics of Fluids*, vol. 28, no. 11, Nov. 2016, doi: 10.1063/1.4966639.

[104] L. Sufrà and H. Steiner, "A Priori Assessment of Subgrid-Scale Models and Numerical Error in Forced Convective Flow at High Prandtl Numbers," *Flow Turbul. Combust.*, vol. 105, no. 2, pp. 377–392, Aug. 2020, doi: 10.1007/s10494-019-00107-y.

[105] C. Liu, Y. Yan, and Y. Yang, "DNS Study on Eddy Viscosity Turbulence Model," Arlington, Sep. 2014. [Online]. Available: http://www.uta.edu/math/preprint/

[106] Y. K. Rudenko, N. A. Vinnichenko, A. V. Pushtaev, Y. Y. Plaksina, and A. V. Uvarov, "Reconstruction of turbulent flow from temperature field measured using Background Oriented Schlieren," *International Journal of Thermofluids*, vol. 23, Aug. 2024, doi: 10.1016/j.ijft.2024.100744.

[107] M. J. Niedźwiecki, M. Ciołek, A. Gańcza, and P. Kaczmarek, "Application of regularized Savitzky–Golay filters to identification of time-varying systems," *Automatica*, vol. 133, Nov. 2021, doi: 10.1016/j.automatica.2021.109865.

Publications

Özesme, G., Otic, I., Ertunc, Ö., Wiltschko, F. (2024). Impact of the boundary conditions and buoyancy on turbulent heat transfer at supercritical pressure: LES study, Kerntechnik 2024. Leipzig, Germany, June 11-13.